

Aus der Klinik für Radiologie  
der Medizinischen Fakultät Charité – Universitätsmedizin Berlin

DISSERTATION

Magnetic Particle Imaging: New Approaches for Vascular Imaging

Magnetic Particle Imaging: Neue Ansätze für die Gefäßbildgebung

zur Erlangung des akademischen Grades Doctor of Philosophy (PhD)  
vorgelegt der Medizinischen Fakultät Charité – Universitätsmedizin Berlin

von  
Azadeh Mohtashamdolatshahi  
aus Teheran, Iran

Datum der Promotion: 04.03.2022

# Table of Contents

List of abbreviations .....	4
List of figures .....	5
Abstract .....	6
Zusammenfassung.....	8
1. Introduction.....	10
2.Theory .....	12
2.1 Magnetic nanoparticles .....	12
2.2 Basic principles of MPI .....	14
2.2.1 Signal generation .....	14
2.2.2 Signal encoding.....	16
2.2.3 Image reconstruction.....	17
2.3 Comparison of MPI with other medical imaging modalities.....	18
3. Materials and methods .....	20
3.1 Magnetic particle imaging (MPI) tracers.....	20
3.2 Magnetic particle spectroscopy (MPS).....	21
3.3 MPI acquisition and reconstruction parameters.....	21
3.4 MPI phantom studies .....	22
3.5 Animal experiments.....	23
3.6 Image analysis of in vivo and ex vivo MPI .....	24
3.7 Histological analysis and immunohistology .....	25
3.8 Determination of MRI blood half-life of MCP-PEG.....	25
3.9 Cell culture and uptake of MNP .....	26
4.Results.....	27
4.1 Evaluation of the tracer performance by their MPS and MPI spectra .....	27
4.2 Evaluation of reconstruction parameters in single-tube phantoms .....	27
4.3 Evaluation of vessel phantoms.....	29
4.4 Angiography of inferior vena cava and abdominal aorta in healthy rat model .....	30
4.5Ex vivo MPI of vascular inflammation in abdominal aortic aneurysm in mouse model	32
4.6 Prolongation of blood half-life of MCP.....	33
5. Discussion.....	35
6. Conclusion and outlook .....	39

7. References.....	40
Statutory declaration .....	44
Declaration of my own contribution to the publications .....	45
Publication A: MPI Phantom Study with A High-Performing Multicore Tracer Made by Coprecipitation.....	45
Publication B: In vivo magnetic particle imaging: angiography of inferior vena cava and aorta in rats using newly developed multicore particles .....	65
Publication C: Ex vivo magnetic particle imaging of vascular inflammation in abdominal aortic aneurysm in a murine model.....	75
Curriculum Vitae .....	87
Complete list of publications .....	88
Acknowledgments.....	89

## List of abbreviations

<b>A3</b>	Amplitude of third harmonic
<b>A5</b>	Amplitude of fifth harmonic
<b>AA</b>	Abdominal aorta
<b>AAA</b>	Abdominal aortic aneurysm
<b>Aortic C<sub>max</sub></b>	Aortic bolus peak
<b>ApoE</b>	Apolipoprotein-E
<b>BG</b>	Background
<b>CA</b>	Contrast agent
<b>CMD</b>	Carboxymethyl dextran
<b>D<sub>H</sub></b>	Hydrodynamic diameter
<b>D<sub>L</sub></b>	Vessel lumen diameter
<b>DLS</b>	Dynamic light scattering
<b>ECM</b>	Extracellular matrix
<b>Fe</b>	Iron
<b>γ-Fe<sub>2</sub>O<sub>3</sub></b>	Maghemite
<b>Fe<sub>3</sub>O<sub>4</sub></b>	Magnetite
<b>FFP</b>	Field free point
<b>FOV</b>	Field of view
<b>H<sub>D</sub></b>	Drive field
<b>ION</b>	Iron oxide nanoparticles
<b>i.v.</b>	Intravenous
<b>IVC</b>	Inferior vena cava
<b>MCP</b>	MPI-tailored multicore nanoparticles
<b>MNP</b>	Magnetic nanoparticles
<b>MPI</b>	Magnetic Particle Imaging
<b>MRI</b>	Magnetic Resonance Imaging
<b>N<sub>f</sub></b>	Number of frequencies
<b>PEG</b>	Polyethylene glycol
<b>PET</b>	Positron emission tomography
<b>RES</b>	Reticuloendothelial system
<b>SF</b>	System function
<b>SNR</b>	Signal-to-noise ratio
<b>SPECT</b>	Single-photon emission computed tomography
<b>t<sub>1/2</sub></b>	Blood half-life
<b>TEM</b>	Transmission electron microscopy
<b>THP-MΦ</b>	THP-1 differentiated macrophages
<b>Venous C<sub>max</sub></b>	Venous bolus peak
<b>VOI</b>	Volume of interest
<b>λ</b>	Tikhonov regularization term

## List of figures

Figure 1. Multicore magnetic nanoparticle .....	13
Figure 2. Basic principle of Magnetic Particle Imaging .....	15
Figure 3 An illustration of the field free point .....	16
Figure 4. Schematic drawing of vessel phantoms .....	23
Figure 5. MPS and MPI spectrum of MCP and Resovist .....	27
Figure 6. Qualitative assessment of regularization on single tube phantoms .....	28
Figure 7. Signal-to-noise ratio (SNR) over regularization factors ( $\lambda$ ) of single tube phantoms .....	28
Figure 8. Quantified iron mass and volume calculated from single-tube phantoms in dilution series .....	29
Figure 9. Spatial resolution in vessel phantoms for MCP and Resovist .....	30
Figure 10. Dynamic iron concentration curve of first pass IVC and in AA for MCP and Resovist .....	31
Figure 11. Representative in vivo MPI angiographic images of the IVC and AA in rats in all dosages .....	31
Figure 12. The AA isolated by subtraction of venous phase with applied tracer MCP at dosage of 0.1 mmol Fe/kg .....	32
Figure 13. Isosurface-rendered MPI image of ex vivo AAA and validation of quantification MPI with MPS results .....	33
Figure 14. T1-weighted coronal MR images of pre- and post-injection of MCP-PEG and the kinetics tracer blood clearance .....	33
Figure 15. Prussian blue staining of internalized MNP in THP-M $\Phi$ .....	34

## Abstract

Magnetic Particle Imaging (MPI) is a relatively new medical imaging modality that is currently (as of 2020) in experimental phase. MPI utilizes the unique magnetic properties of magnetic nanoparticles (MNP) and visualizes the MNP distribution as three-dimensional maps. MNP characteristics, alongside the intrinsic parameters of the instrumental scanner, determine the spatial resolution, sensitivity and image quality of MPI. Therefore, the development of optimized MPI tracers is crucial for advancement of the imaging technique and to identify potential applications in diagnostic imaging.

Multicore nanoparticles (MCP) tailored for MPI were synthesized in our lab, and their MPI performance was evaluated in comparison to Resovist in phantoms, single or double tubes, and in vivo. For the in vivo angiography study, 8 healthy rats were examined in 16 examinations. The inferior vena cava (IVC) and abdominal aorta (AA) were imaged in a 2 cm suprarenal segment after i.v. injection of MCP and Resovist in 3 dosages of 0.1, 0.05 and 0.025 mmol Fe/kg. In a further study, the vascular inflammation in abdominal aortic aneurysms (AAA) induced in Apolipoprotein E-deficient-mice (n=32) was imaged with MPI ex vivo, 24 h post i.v. Resovist injection (dosage 46.66  $\mu\text{g}$  Fe/kg). The results were validated by histology and magnetic particle spectroscopy (MPS). Moreover, the blood half-life ( $t_{1/2}$ ) of modified MCP, surface coated with Polyethylene glycol (PEG), using MRI was investigated.

MCP, compared to Resovist, provided higher signal-to-noise ratio in MPI, a finer spatial resolution of 1 mm or even lower, higher sensitivity, with successful visualization of 0.1 mmol Fe/l concentration in phantoms, and a distinctive qualitative outcome in in vivo MPI angiographic studies. After administration of MCP at dosages of 0.1, 0.05 mmol Fe/kg, the vessel lumen diameters ( $D_L$ ) of IVC and AA could be assessed with  $IVC=2.7 \pm 0.6$  and of  $AA=2.4 \pm 0.7$  mm. The accumulation of Resovist in inflammatory cells of AAA was imaged ex vivo quantitatively in MPI and verified by Prussian blue and anti-CD86 immunohistochemistry. The iron amount quantification results correlated with MPS results ( $R=0.99$ ). The successful PEGylation of MCP led to prolongation of  $t_{1/2}$  from several minutes to over an hour.

Overall, MCP showed superior MPI image quality. The results implied that angiographic and cellular imaging of vascular abnormalities such as aneurysm is feasible with MPI, with the

simultaneous quantitative measurement of MNP concentration. MPI is an evolving technology, with a good prospect as a clinical diagnostic tool. The findings in the presented work underline the current possibilities, challenges and limitations of MPI for experimental in vivo imaging with the perspective towards potential future clinical applications.

## Zusammenfassung

*Magnetic Particle Imaging* (MPI) ist eine relativ neue medizinische Bildgebungsmodalität, die sich derzeit (Stand 2020) in der experimentellen Phase befindet. MPI nutzt die einzigartigen Eigenschaften magnetischer Nanopartikel (MNP) und visualisiert die MNP-Verteilung dreidimensional. Neben den intrinsischen Parametern des Scanners bestimmen die MNP-Eigenschaften die räumliche Auflösung, die Empfindlichkeit und die Bildqualität von MPI. Daher ist die Entwicklung optimierter MPI-Tracer entscheidend für die Weiterentwicklung dieser Bildgebungstechnik und die Identifizierung potenzieller Anwendungen in der diagnostischen Bildgebung.

In unserem Labor wurden auf MPI optimierte Multicore-Nanopartikel (MCP) synthetisiert und ihre MPI-Leistung in Phantomen und *in vivo* im Vergleich zu Resovist bewertet. Die *In-vivo*-Angiographiestudie wurden an 8 gesunden Ratten in 16 Untersuchungen durchgeführt. Nach i.v.-Injektion von MCP und Resovist in den Dosierungen 0.1, 0.05 und 0.025 mmol Fe/kg wurden die *Vena cava inferior* (IVC) und die abdominale Aorta (AA) suprarenal in einem 2 cm langen Segment abgebildet. In einer weiteren Studie wurde die vaskuläre Entzündung in der Wand von induzierten abdominalen Aortenaneurysmen (AAA) in ApoE<sup>-/-</sup> Mäusen (n=32) 24 h nach i.v.-Resovist-Injektion abgebildet (Dosierung 46.66 µg Fe/kg). Die Ergebnisse wurden durch Histologie und Magnetic Particle Spectroscopy (MPS) validiert. Darüber hinaus wurde die Bluthalbwertszeit ( $t_{1/2}$ ) von PEG-modifizierten MCP mittels MRT untersucht.

MCP lieferten im MPI im Vergleich zu Resovist ein höheres Signal-Rausch-Verhältnis, eine höhere räumliche Auflösung von unter 1 mm, eine höhere Sensitivität bei erfolgreicher Visualisierung der 0.1 mmol Fe/l in Phantomen und ein qualitativ besseres Ergebnis in *in-vivo*-MPI-Angiographiestudien. Nach Verabreichung von MCP in den Dosierungen 0.1 und 0.05 mmol Fe/kg konnten die Gefäßlumendurchmesser von IVC = 2,7±0,6 mm und AA = 2,4±0,7 mm berechnet werden. In entzündlichen Zellen des abdominalen AAA konnte *ex vivo* die Akkumulation von Resovist quantitativ im MPI abgebildet und durch Berliner Blaufärbung und Anti-CD86-Immunhistochemie verifiziert werden. Die Ergebnisse der Eisenmengenquantifizierung korrelierten mit den MPS-Ergebnissen (R=0,99). Die erfolgreiche PEGylierung von MCP führte zu einer Verlängerung von  $t_{1/2}$  wenigen Minuten auf über eine Stunde.

Insgesamt zeigte MCP eine überlegene MPI-Bildqualität. Die Ergebnisse implizieren, dass eine angiographische und zelluläre Bildgebung von Gefäßanomalien wie Aneurysmen bei gleichzeitiger quantitativer Messung der MNP-Konzentration mit MPI möglich ist. MPI ist eine sich weiterentwickelnde Technologie mit Potenzial für die klinische Diagnostik. Die Ergebnisse der vorgestellten Arbeit unterstreichen die aktuellen Möglichkeiten, Herausforderungen und Grenzen des MPI für die experimentelle *in-vivo*-Bildgebung in Hinblick auf mögliche zukünftige klinische Anwendungen.

# 1. Introduction

In 2005, Magnetic Particle Imaging (MPI) was introduced as a novel imaging modality [1]. MPI is a noninvasive, tracer-based, tomographic imaging modality that allows quantitative tracer imaging. The tracers in MPI comprise of magnetic nanoparticles (MNP). Since then, extensive research has been conducted to progress the field toward improving system hardware and instrumentation, optimizing the system theory underlying MPI, and developing MPI-tailored MNP for higher resolution and better imaging performance of MPI.

Since the establishment of the earliest MPI scanner prototype, various commercial and custom built MPI scanners have been developed. Currently, a growing number of research groups worldwide is active in the field of MPI.

Currently not one universal MPI systems theory has been established. Two types of commercial small animal MPI scanners are available, MPI in frequency domain [1] from the company Bruker Biospin GmbH, Germany and x-based MPI [2] from Magnetic Insight, Inc, USA. A number of research groups have developed concepts differing in scanner design, acquisition and reconstruction strategies. Scaling of MPI for human imaging may be an engineering challenge but is theoretically possible, and recently the first report on a human-sized MPI scanner for brain applications has been published [3]. Though the success of this tracer-driven imaging modality certainly relies on the availability of tracers optimized for MPI. Synthesis and development of MPI-tailored tracers are an important field in MPI research and new tracers specifically for MPI applications are being actively developed. Commercially available MNP used in MPI include Resovist (containing ferucarbotran), Synomag [4] and Perimag [5], and a number of lab-developed, non-commercial MNP, like LS-008 (University of Washington, Seattle) [6], have shown promising results in experimental studies. In this regard, MPI specific multicore nanoparticles (MCP), were synthesized at Charité, Group of Experimental Radiology [7]. The term MCP used in this work does not generally refer to multicore nanoparticles, also called “nanoflowers”, though, the MPI specific MNP synthesized in our group. The preliminary investigations suggested that MCP are effective MPI tracers [7]. One of the objectives of this research project was to evaluate, to which extent MCP contribute to the MPI image quality, in vitro and in vivo. Since particularly the interactions of the MNP with the biological matrix, such as uptake into cells, changes the dynamic magnetization of MNP [8] (see 2.2.1), it was of interest to investigate the measures needed to be taken into consideration for the potential clinical MPI scenarios and investigate how factors such as reconstruction parameters (see 2.2.3) and image post-processing can optimize further in vivo imaging. The

following study experimentally investigated the potential clinical applications of MPI for vascular imaging, angiography and vascular inflammation imaging, and peculiarly in regard to employment of newly developed optimized MCP particles towards high-resolution, structure-sensitive MPI.

## 2.Theory

This chapter briefly outlines the underlying theoretical foundation of MNP and MPI to facilitate understanding of the relevant concepts introduced in the present work.

### 2.1 Magnetic nanoparticles

Magnetic nanoparticles (MNP) are nanosized magnetic materials whose functional properties are determined not only by their structure and chemical composition but particularly also by their size. The nanosized materials exhibit different behavior than bulk material of the same chemical composition. The MNP can be influenced by an external magnetic field, and their response to the magnetic field can be measured following their detection. This makes them particularly attractive for a wide range of biomedical diagnostic applications such as contrast media in imaging, in therapeutics e.g., drug delivery systems and hyperthermia, or by combining their properties for use in theranostics.

MNP are composed of a ferromagnetic core and a nonmagnetic coating, which ensures stability of MNP and thus prevents their agglomeration and increases their biocompatibility. MNP have a diameter range of a few nm up to about 100 nm and their controllable size distribution in the nanometer range is a key factor which determines their magnetic and physiochemical characteristics. The core size dominates the magnetic behavior, while the hydrodynamic size ( $D_H$ ), the core-shell combination, determines the physiochemical properties. The core can be synthesized from a variety of materials e.g., iron and cobalt or alloys of these metals. Due to their biocompatibility, iron oxide nanoparticles (ION), consisting of magnetite ( $Fe_3O_4$ ) and maghemite ( $\gamma-Fe_2O_3$ ), are more suitable for biomedical applications [9]. Stabilization of the core is achieved by different types of nonmagnetic coating, which can be electrostatic, e.g., by using citric acid as coating, or steric, e.g., by using polyethylene glycol (PEG) as coating, or a combination of both, e.g., by carboxymethyl dextran (CMD) as coating. Besides providing stability, the nonmagnetic shell affects the MNP fate in the biological environment, and it can further be functionalized by coupling targeting ligands, depending on the anticipated application. The most common methods to synthesize ION are chemical coprecipitation and thermal decomposition. Chemical coprecipitation synthesis is done in aqueous solution, which makes the subsequent step of phase transfer redundant, which is common when synthesis is accomplished by thermal decomposition. The MNP used in the current work were synthesized by a modified chemical co-precipitation method. Excellent reviews have been published towards technical advances and the development of suitable MPI-MNP, amongst others by

Kratz et. al [10], which are relevant for this work. The size, shape and crystalline structure of the core depend on the fabrication process, which affects the magnetic properties of the MNP system. The MNP are either single-core (containing one single domain nanocrystallite) or multicore (containing many single domain nanocrystallites). The MNP used in this work are multicore particles where single crystallites in sizes in range of 4 to 6 nm are densely packed in aggregates (Figure 1). The existence of multiple cores might be beneficial, in the sense that this leads to an increase of effective magnetic moment of the MNP at a given size [11]. The reduced dipolar interactions of multicore clusters in the absence of magnetic fields help to ensure high dispersibility in aqueous media and high stability for utilizing them in biological media.

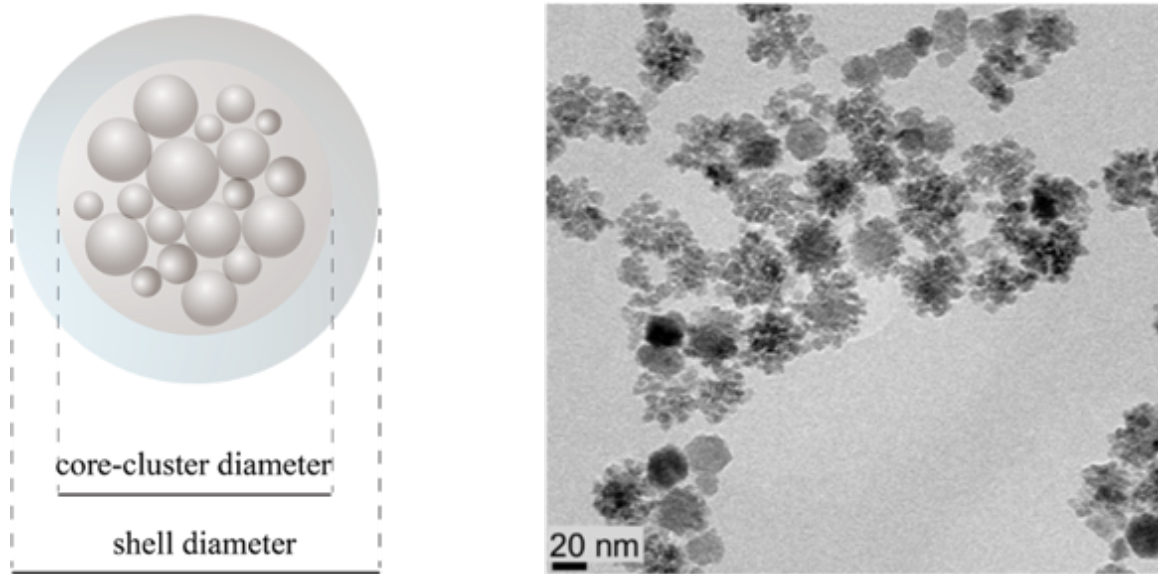


Figure 1. Diagram of a multicore magnetic nanoparticle (left). Transmission electron microscopy (TEM) image of multicore nanoparticles (MCP) used in this work (right) [12]. The magnetic core-cluster is coated with nonmagnetic shell, e.g., CMD, for stabilization. The effective magnetic moment of a multicore nanoparticle is the vectorial sum of all magnetic moments.

MNP with typical sizes of less than 100 nm have a single magnetic domain, as it is energetically unfavorable for MNP in this size range to form domain walls [9, 11]. The magnetization of the mono-domain MNP in a simplified manner is described by the Langevin function (Figure 2b.) under assumption of thermal equilibrium. In thermal equilibrium, hysteresis effects are absent. The Langevin theory is implemented to explain the physics of MNP magnetization in MPI, but does not include influential factors such as relaxation effects, explained below, and interparticle interactions [9]. According to the Langevin function the MNP magnetization is given by [13]:

$$M = M_0 L\left(\frac{HV M_s \mu_0}{k_B T}\right)$$

with  $L(\xi) = \coth(\xi) - \frac{1}{\xi}$

where  $M_0$  is the saturation magnetization of MNP,  $H$  is the external magnetic field,  $V$  is the volume of the MNP core,  $M_s$  is the saturation magnetization of MNP material,  $\mu_0$  is the permeability of vacuum,  $k_B$  is the Boltzmann constant,  $T$  is the MNP temperature. By assuming that the MNP have a spherical shape, the term  $V$ ,  $V = \frac{1}{6}\pi d^3$ , indicates the dependency of the MNP magnetization on the core diameter [13].

By application of time-varying magnetic field, the MNP magnetization follows the applied field with a certain delay, that can be described by the relaxation time  $\tau$ . This dynamic magnetic behavior of MNP is dominated by a combination of Néel and Brown relaxation mechanisms. The alteration in orientation of the magnetization moment can be accomplished by movement or rotation of the whole particle (Brown relaxation) or by internal reorientation in the domain (Néel relaxation). The Néel relaxation time is given by:

$$\tau_N = \tau_0 \exp\left(\frac{K^A V}{k_B T}\right)$$

with  $\tau_0$  as material dependent time constant and  $K^A$  is the magnetic anisotropy of the MNP. The Brownian relaxation time is given by:

$$\tau_B = \frac{3\eta V^H}{K_B T}$$

with  $\eta$  as viscosity of the MNP environment and  $V^H$  as the hydrodynamic volume of MNP. The total relaxation time can be approximated by:

$$\tau = \frac{\tau_B \tau_N}{\tau_B + \tau_N}$$

The equations show the influence of the MNP environment on the dynamics of MNP in MPI applications, for instance, temperature or the binding state of MNP. Effective relaxation also depends on the frequency of the applied magnetic field. Brownian relaxation is dominant at lower frequencies if the MNP are in a viscose solution and not immobilized, while Néel relaxation is dominant in the higher frequency range [14].

## 2.2 Basic principles of MPI

### 2.2.1 Signal generation

Signal generation in MPI is based on the nonlinear magnetization response of the MNP in the presence of a sinusoidal magnetic field, the so-called excitation or the drive field ( $H_D$ ). MNP are the only source of the informative signal in MPI. Following the application of the alternating drive field with excitation frequency  $f_0$ , if a receive coil is placed in the vicinity the

of MNP, the time-varying magnetization of the MNP is detectable through the voltage signal induced according to Faraday's law,  $S(t)$  in time domain. For differentiation of signals induced by MNP and signal induced by drive fields, the signal is Fourier-transformed,  $S_n$ .

In the presence of a homogeneous magnetic field, the ensemble of MNP align with the external field. The magnetization of MNP is nonlinear in relation to the external magnetic field before reaching saturation (Figure 2b.). In the frequency domain, the excitation signal is represented as a single peak,  $f_0$ , also called the fundamental frequency. The nonlinear magnetization response of MNP is characterized as multiples of the  $f_0$  in higher harmonics.  $f_0$  is filtered out of the recorded signal with a bandstop filter. The remaining higher harmonics form the basis of the raw MPI signal. The amplitude of the higher harmonics is proportional to the concentration of MNP [1] and thus allows quantitative statements about the tracer material present in the measured volume. The spectrum of each MNP and furthermore with respect to its surrounding is unique and specific, and therefore distinctive identification and quantification of MNP with a calibration step is attainable.

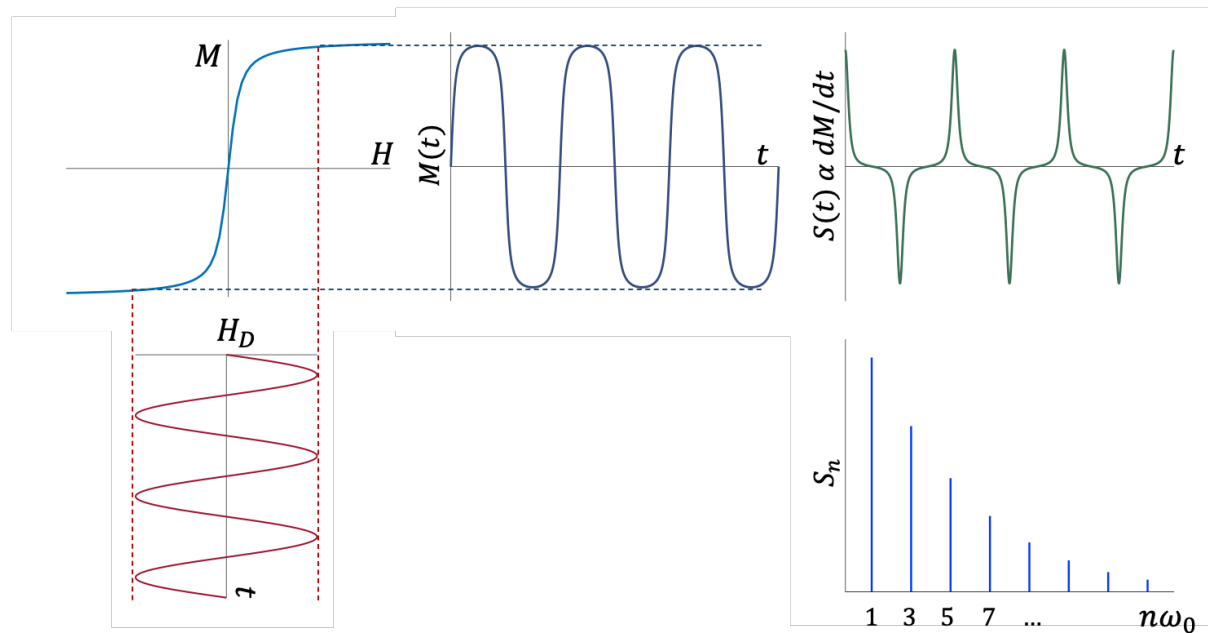


Figure 2. Basic principle of Magnetic Particle Imaging (a) the alternating magnetic field,  $H_D$ , magnetizes the MNP (c). The magnetization curve of the MNP is defined by the Langevin function (b). The magnetization response of MNP induces a voltage in the receive coil (d). The higher harmonics in the Fourier-transformed signal arise from the MNP magnetization response (e) and can be distinguished from the fundamental frequency of the excitation signal (here  $n=1$ ). Recreated from [1].

Since the induced MNP signal is proportional to the derivative of the magnetization curve, a steeper magnetization, resulting from larger MNP, is advantageous for spatial resolution. Modeling studies predict a core size of 25–30 nm or even larger to be most favorable for magnetite [15]. However, in clinical practice, the usable size range is limited to the aforementioned size by the intended medical purpose, e.g., need for avoiding formation of

aggregates and relaxation effects (Brown and Néel relaxation) [14], since the relaxation effects will begin to dominate in larger MNP.

### 2.2.2 Signal encoding

While the signal spectrum allows conclusions to be drawn about the concentration of MNP in the field of view (FOV), no further information about the position of the MNP signal in the FOV is obtainable. In order to localize the MNP in space, a static inhomogeneous gradient field, the so-called selection field is applied to magnetically saturate MNP outside a specific region, the field free region (FFR). The FFR can be encoded using a field free point (FFP), or a field free line (FFL). In the present work FFP-based scanner has been implemented, and for this reason we focus on the notion of FFP encoding. The selection field can be generated by a pair of permanent magnets or coils in Maxwell configuration. The opposing magnetic fields compensate each other generating an area with zero field strength in their center, the FFP. With the strong gradient strength, the MNP are saturated in all locations outside the FFP. With increasing distance from the FFP, the field strength rapidly increases linearly, and no or neglectable signals from MNP in vicinity of the FFP are detectable. Hence no detectable signal is generated outside the FFP. The superimposition of the gradient field with the drive field will result in confining the measured signal to the FFP, and since the volume of the FFP is determined by the gradient strength, the spatial resolution of MPI is directly correlated with the selection field strength. The gradient strength is two times higher in z-direction, due to the encoding scheme of the selection-field coils, providing a higher resolution along this direction.

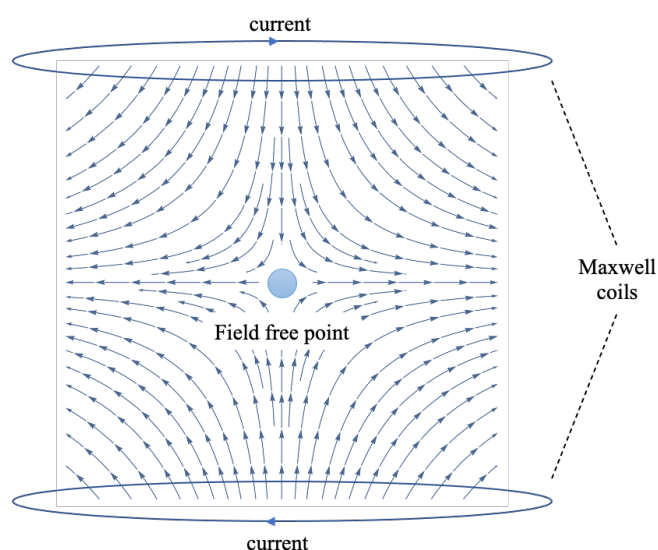


Figure 3 Illustration of the field free point generated by an opposite Maxwell coil pair. The spatial inhomogeneity of the magnetic field will saturate all MNP except those in the field free region. Recreated from [13].

A complete volume of interest (VOI) can be imaged by moving the object or the FFP in the FOV. Most commonly the FFP is moved in the FOV by electromagnetic fields rather than mechanically moving the sample. The drive field applied to excite the MNP moves the FFP back and forth in one dimension [16], e.g., in x- direction. When additional drive fields with slightly different excitation frequencies are applied in y- and z-direction, the FFP can be moved in a 3D trajectory (Lissajous-trajectory). The drive fields shift the position of the FFP and move it across the entire imaging volume in sub second range. The drive fields frequencies in this work are chosen around 25 kHz resulting in scanning of the FOV used in the following studies in a period of 21.5 ms. With the known trajectory of the FFP movement, the recorded signal is assigned to the corresponding voxel in the FOV at each time step and a discrete image can be reconstructed from the time series data. Due to excitation in 3 dimensions with three slightly different frequencies,  $f_{0x}$ ,  $f_{0y}$ ,  $f_{0z}$ , the signals are not only arising at multiples of the  $f_0$  in higher harmonics as in 1 dimension, but as mixed frequencies as well. Every frequency component is a linear combination of excitation frequencies for each drive field, given by [17]:

$$f = |n_x f_x + n_y f_y + n_z f_z|$$

and the mixing order is given by:

$$n = |n_x| + |n_y| + |n_z|$$

### 2.2.3 Image reconstruction

Various concepts have been proposed for MPI image reconstruction. Currently two approaches are used in commercially available MPI systems dependent on the MPI system: Harmonic space system matrix or system function (SF) MPI developed by Philips researchers, and x-space MPI for FFL scanners [18], developed by Magnetic Insight. In the present work, the SF-based approach was used, and for this reason, we here focus on SF-based reconstruction.

The SF approach is a calibration-based technique in which the magnetization response of MNP is measured. For this a point-like reference sample containing a known amount of MNP is measured by means of a robotic arm in all possible spatial positions of voxels in FOV. The SF obtained includes information on imaging trajectory, MNP signal and their position in space, receive coil sensitivity and the transfer function of the MPI electronic instrumentation. The acquired SFs are specific for each tracer and their respective environment, and any hardware modification will affect the frequency response of the tracer, and new SFs are to be recorded. The SF measurements are time demanding, requiring up to several days for completion. An object with unknown distribution of MNP should be scanned using the same imaging

parameters, e.g., drive field, as applied for the SF measurement in the MPI scanner. The relation between MNP density and the measured MPI signal is linear, given by

$$u = Gc$$

where  $u$  is the complex vector matrix of measured signal,  $G$  the SF matrix, and  $c$  is the matrix containing the MNP-concentration in each voxel of FOV. The reconstruction problem is an inverse problem of linear equations. Due to the noisiness of measured data, e.g., hardware shortcomings, simple computation of the inverse of the SF and multiplying it with the measured vector results in an ill-posed problem. Therefore, a regularization term ( $\lambda$ ), Tikhonov regularization term, is introduced into the equation.

$$\| Gc - u \|^2 - \lambda \| c \|^2 \rightarrow \min$$

The frequently used method for image reconstruction in MPI by standard Tikhonov regularization is Kaczmarz algorithm which is an iterative algorithm and has been used in this work. The signal becomes approximately exact over multiple iterations. The Kaczmarz algorithm is favorable in terms of computation cost and memory requirement and is therefore preferred for large scales of data in MPI.

### **2.3 Comparison of MPI with other medical imaging modalities**

The current state of MPI can be compared with that of Magnetic Resonance Imaging (MRI) in the early 1980s, a functional imaging concept was available, first commercial (animal) scanners were manufactured and contrast agents (CA) were just developed [19]. The general hardware and imaging concepts of MPI are slightly similar to MRI, in concepts essentially in utilization of magnetic fields for excitation and detection, and gradient fields for spatial encoding [19]. However, the principal scheme of imaging mechanism of MPI as explained in section 2.2 differs from MRI. The tracers used in MPI are rather familiar, since the application of MNP as CA in MRI well known for lesion detection, angiography, cell tracking and other applications. The ION which were used for clinical MRI, are well tolerated and provide a reliable safety for patients. MPI using MNP could be an option in patients with chronic kidney disease, since IONs are mainly eliminated through the reticuloendothelial system (RES), predominantly in liver and spleen [9]. Unlike MRI, where the MNP cause signal void and hence a negative contrast, MNP generate a positive signal in MPI, however without anatomical information of the surrounding tissue, similar to the imaging modalities Single-photon emission computed tomography (SPECT) or Positron emission tomography (PET), but without ionizing radiation. Another advantage of MPI is the proportionality of the measured signal amplitude to the local

amount of MNP, as this potentially enables the quantitative determination of MNP concentration. MPI is faster than MRI, with a high temporal resolution of up to 46 3D volumes/s. With the short image acquisition time of MPI, high sensitivity to the MNP and 3D imaging capability, MPI has great potential for a range of imaging applications including fast 3D high-contrast angiography and inflammatory imaging. Currently available MPI has a spatial resolution on the order of millimeters, which is comparable to that of small animal PET or SPECT. However, the spatial resolution of MPI can still be improved with better scanner design and MPI-tailored MNP. Table 1 summarizes major aspects of the common medical imaging modalities compared to MPI.

	<b>CT</b>	<b>MRI</b>	<b>PET</b>	<b>SPECT</b>	<b>MPI</b>
<b>Spatial resolution</b>	~0.5 mm	~1 mm	~4 mm	~10 mm	~ 1 mm or submm
<b>Acquisition time</b>	1 s	1 s – 10 min	1 min	1 min	<0.1 s
<b>Sensitivity</b>	Low	Low	High	High	Theoretically high
<b>Quantifiability</b>	Yes	Yes, but it requires complex methodology	Yes	Yes	Yes
<b>Harmfulness</b>	X-ray	Heating	$\beta/\gamma$ Radiation	$\gamma$ Radiation	Heating

Table 1. Comparison of different imaging modalities. Modified from [14]

### 3. Materials and methods

#### 3.1 Magnetic particle imaging (MPI) tracers

The MNP employed in this study are: Resovist and MCP. While both of these MNP have iron oxide cores ( $\text{Fe}_3\text{O}_4/\gamma\text{-Fe}_2\text{O}_3$ ), they differ in core size, core size distribution, coating and  $D_H$ . Resovist (initially developed by Schering AG, Berlin, Germany), containing the active substance Ferucarbotran, is one of the few ION approved for use in clinical medical imaging and was developed as a CA for contrast-enhanced liver MRI [20]. Manufacture of Resovist was discontinued in Europe in 2008, but the product is commercially available from the Japanese distributor (Fujifilm RI Pharma and I'rom Pharmaceutical Co Ltd, Tokyo, Japan). Resovist is widely used in experimental MPI measurements due to its acceptable MPI image quality, stability over time, availability, reliability between batches and applicability in vivo without adverse reactions, and was used in this work for comparison. MCP tailored as MPI tracer was developed in-house (Charité). The MCP were produced via synthesis of green rust, oxidation and following addition of a stabilizing agent [7]. Two types of MCP MNP were employed in the studies outlined here. One type coated with carboxymethyl dextran (CMD), and the second with the surface coating modified with Polyethylene glycol (PEG), MCP-PEG. The characteristics of the employed MNP are listed in Table 2.

MNP	Resovist	MCP	MCP-PEG
<b>Mean core cluster diameter (TEM)</b>	4-16 nm	32 nm	32 nm
<b>Mean <math>D_H</math> (DLS)</b>	60 nm	53 nm	-
<b>Poly dispersity index (DLS)</b>	0.17	0.08	-
<b>Saturation Magnetization</b>	98 Am <sup>2</sup> /kg (Fe)	104 Am <sup>2</sup> /kg (Fe)	-
<b>Mean magnetic moment</b>	2.7 aAm <sup>2</sup>	3.9 aAm <sup>2</sup>	-
<b>Surface coating</b>	Carboxydextran	Carboxymethyl dextran (CMD)	Polyethylene glycol (PEG)
<b>Zeta-Potential</b>	-24 mV	-39 mV	-3 mV
<b>Stock solution Conc. (mmol Fe/l)</b>	500	145.5	155

Table 2. MNP used in the studies and their characteristics. Parameters from [7, 12, 21].

The magnetic core/core cluster size was measured using Transmission electron microscopy (TEM). The  $D_H$ , Poly dispersity index and the surface charge (Zeta-potential) of the MNP were determined using a Zetasizer Nano ZS particle analyzer (Malvern Instruments, Worcestershire, UK). The blood half-life ( $t_{1/2}$ ) of MNP are as follows: 3.9–5.8 min in MRI [22] and less than 15 min in MPI [6, 23] for Resovist, and 8.8 and 17.4 min at 0.05 and 0.1 mmol Fe/kg in rats calculated from MR imaging for MCP in previous studies [7]. The blood  $t_{1/2}$  of MCP-PEG is reported in the results.

### **3.2 Magnetic particle spectroscopy (MPS)**

MPS can be considered a zero-dimensional MPI scanner without spatial resolution, i.e., one drive field and no gradient fields, with higher sensitivity than MPI. MNP are characterized by MPS primarily to determine their potential applicability for MPI. MPS measurements were performed with a commercial MPS-device (Bruker Biospin, Germany) with a sinusoidal excitation signal with an amplitude of up to 25 mT, a frequency of 25 kHz and a sample temperature adjustable up to 42 °C. The nonlinear magnetization response of samples containing MNP was measured for 10 s by a pickup coil at 37 °C. The MNP samples were filled in PCR tubes for MNP characterization and tissue samples were investigated for validation of MPI quantification results. For characterization of MNP, the MPS spectra of samples were normalized to the known iron content of each sample, resulting in the spectrum of the magnetization given in  $\text{Am}^2/\text{mol}$  (Fe).

For quantitation of unknown MNP concentration in a tissue samples, a reference sample with a known MNP concentration is measured beforehand. The reference sample was chosen considering the magnetization behavior of the measured sample in the immobilized state, according to the A5/A3-ratio (amplitude of the fifth harmonic to the third ratio) of the measured sample. The two reference samples used for quantification were in water dispersion or immobilized by freeze-drying in 10% mannitol with 1 mmol Fe/L concentration. For quantification, the amplitude of the A3 of the MPS spectra of measured samples was normalized to the amplitude of the known reference sample.

### **3.3 MPI acquisition and reconstruction parameters**

All MPI measurements were performed in a small animal MPI scanner (Bruker 25/20 FF, Bruker Biospin GmbH, Ettlingen, Germany), which operates according to the FFP principle

and requires a SF for reconstruction of images. The scanner is equipped with a receive-only gradiometer coil [24] (developed by Bruker and Physikalisch-Technische Bundesanstalt (PTB)) contributing to a better signal-to-noise ratio (SNR) and sensitivity. MNP are excited by drive fields of 12 mT in three orthogonal axes at three slightly different frequencies (2.5 MHz divided by 102/96/99 in x-/y-/z-direction). A selection gradient with a strength of up to 1.25 T/m/ $\mu_0$  in x- and y-axis and 2.5 T/m/ $\mu_0$  in z-axis was used for spatial encoding and generating the FFP. The FFP is moved along a 3D-Lissajous trajectory by the three drive fields scanning the FOV in a period of 21.5 ms results in an acquisition rate of 46 volumes/s. The data were acquired and reconstructed using Paravision software (Bruker Biospin, Germany). The SFs were measured in water dispersion and had a size of  $33 \times 33 \times 33$  voxels, except the one used in the ex vivo abdominal aortic aneurysms (AAA) imaging study, which had the immobilized state, freeze-dried in mannitol sugar matrix and therefore was less resolved (size:  $25 \times 25 \times 13$  voxels). Using an iterative Kaczmarz algorithm, the images in the phantom study and in vivo angiography study were reconstructed to  $33 \times 33 \times 33$  voxels and in the ex vivo AAA imaging study to  $25 \times 25 \times 13$  voxels. The physical FOV had a size of  $19.2 \times 19.2 \times 9.6$  mm<sup>3</sup> leading to an overscan [25] to minimize artifacts by signals generated outside of the FOV. The bandwidth was limited to 0.09–1.25 MHz. The maximum order of mixing frequencies was 25 for all images. Prior to reconstruction, the background (BG) signal from a measurement without MNP was subtracted from the measured subject signal. In the reconstruction of phantoms and the ex vivo AAA imaging study, a block average through the entire sample acquisition time was applied in the reconstruction step to reduce image BG artifacts. Further reconstruction parameters are discussed in section 3.2. The data and images were analyzed using Matlab (Mathworks, Natick, MA, USA).

### **3.4 MPI phantom studies**

In order to evaluate image SNR, BG artifacts and spatial resolution, as well as to optimize and standardize image reconstruction parameters within the studies, phantoms of aqueous dispersions of MNP in a range relevant for in vivo studies, 10-0.1 mmol Fe/L, were investigated [12]. For this purpose, PVC tube phantoms with inner diameters of 1, 2 and 3 mm with wall thickness of 0.5 mm and length of 20 mm were used and the ends were sealed with Parafilm. Single-tube phantoms with inner diameter of 3 mm, filled with 90  $\mu$ L tracer dispersion, were employed for determination of optimal reconstruction parameters with respect to the highest SNR and quantitative information obtained from MPI. In order to achieve this, the phantom

images were reconstructed with different regularization factors ( $\lambda$ ), ranging from  $10^{-6}$  to  $10^0$  and with 5 iterations. Image analysis was performed in Matlab. The 3D dataset was thresholded with a 30% cutoff of the maximum value for BG artifacts minimization prior to the determination of the iron content and volume.

Double-tube phantoms represented the adjacent blood vessels, e.g., inferior vena cava (IVC) and abdominal aorta (AA), and the spatial resolution of MCP was explored for vascular MPI in vitro. Vessel phantoms consisting of six combinations of tubes with 3 different diameters (1-3 mm) but containing the same tracer dilution (10 and 1 mmol Fe/L) were investigated. Given the higher spatial resolution in z-direction – resulting from the higher gradient strength and hence anisotropic spatial resolution - the phantoms were measured in two directions, either aligned longitudinally to x- or to z-axis.

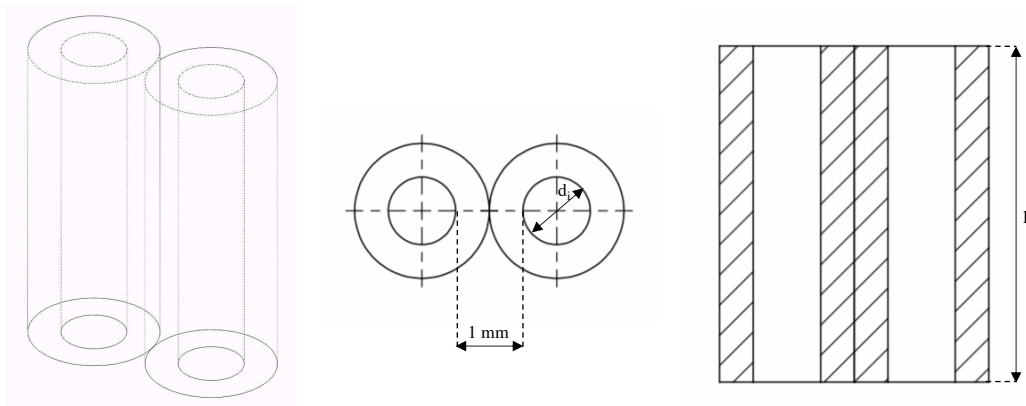


Figure 4. Drawing of double-tube phantoms. The inner diameters of the tubes ( $d_i$ ) were 1, 2 and 3 mm with wall thickness of 0.5 mm and length of 20 mm. The vessel phantoms were assembled by combinations of tubes of different diameter size and tracer concentrations.

### 3.5 Animal experiments

All procedures were approved by the Berlin State Office for Health and Social Affairs Berlin (LAGESO) and were carried out in accordance with the guidelines and provisions for the implementation of the animal welfare act.

For MPI angiography of the inferior vena cava (IVC) and abdominal aorta (AA) in rats [26], 16 in vivo examinations were conducted on 8 healthy 7 weeks old male Sprague Dawley rats (Charles River Laboratories, Sulzfeld, Germany). The FOV covered a small segment of 2 cm in the suprarenal abdominal area. Before the MPI measurement, anesthesia was induced with 5% isoflurane in an anesthetic induction chamber and maintained with 1–2% isoflurane throughout MPI acquisitions. A catheter was fixed in the tail vein for the injection of the MNP.

The subjects were placed in the MPI scanner and scanned prior, during and immediately after tracer administration for approximately 5 min. MCP and Resovist were administered manually as i.v bolus injection in rats at dosages of 0.1, 0.05 and 0.025 mmol Fe/kg. Each group included three subjects for dosages of 0.1 and 0.05 mmol Fe/kg and two for a dosage of 0.025 mmol Fe/kg. MPI acquisition started one minute prior to full dose tracer injection. Based on the animal welfare act principle the number of animals used in the study was kept to the minimum. Each subject was intravenously (i.v.) injected both tracers, MCP and Resovist, in arbitrary order, with sufficient time between the two successive injections for MNP clearance from the bloodstream (at least one hour apart). This time interval was chosen based on the predetermined blood  $t_{1/2}$  of the tracers (see section 2.1) and the absence of the MNP signal in MPI raw signal. For ex vivo imaging of AAA in MPI [27], AAAs were induced in male, Apolipoprotein-E (ApoE<sup>-/-</sup>) deficient mice (8 weeks old) by continuous infusion of Angiotensin II by pump implantation. The AAA development 3-4 weeks post pump implantation was verified by MR imaging. The mice then were injected with Resovist (I'rom Pharmaceutical Co Ltd) i.v. in the tail vein at a dosage of 50  $\mu$ l (46.66  $\mu$ g Fe/Kg). 24 h post-injection, animals were sacrificed, and the AAA was harvested for ex vivo MPI and MPS measurements and histology. In MR imaging studies for determination of the blood  $t_{1/2}$  of modified MCP-PEG, the MNP were administered i.v. in 12 weeks old healthy male Sprague Dawley rats (n=3) at a dose of 0.05 mmol Fe/kg bodyweight.

	<b>Purpose of study</b>	<b>Animal model</b>	<b>MNP used</b>
<b>1</b>	Angiography of IVC and AA	Healthy rats (n=8)	MCP and Resovist
<b>2</b>	Ex vivo imaging of AAA	ApoE <sup>-/-</sup> mouse (n=32)	Resovist
<b>3</b>	Determination of blood $t_{1/2}$	Healthy rats (n=3)	MCP-PEG

Table 3. Overview of experiments involving rodents.

### 3.6 Image analysis of in vivo and ex vivo MPI

In the angiography study, after preliminary reconstruction of the images, the iron concentration-time curves were generated for further analysis. The VOI was specified on the cross-section of the IVC and AA, and the dynamic intravascular mean signal, respectively iron amount, was determined in the VOIs (shown in Figure 12). With identification of the time of arrival of the bolus from the curves, single images were reconstructed at the time interval  $t_1$ , where venous peak (venous  $C_{max}$ ) is detectable and time  $t_2$ , where the rise in AA is observed in

the iron concentration curve. The reconstructed images from two time points of IVC passage of the MNP, blue, and AA passage of the MNP, red, were overlaid. The attribution of colors to the IVC passage of the MNP and AA passage of the MNP was carried out in Matlab for the purpose of better presentation. To delineate the AA from IVC, the reconstructed image from IVC passage of the MNP was subtracted from the temporally separated AA passage of the MNP. An early post-contrast image ( $t_1$ ) is subtracted from a late post-contrast image ( $t_2$ ). Hence, the IVC and AA were assessable individually. The lumen diameter ( $D_L$ ) of IVC and AA was calculated from the cross-sectional area of the vessels in x-z plane by segmentation, assuming a circular cross-section in the transverse plane.

In the ex vivo MPI of AAA, the iron amount in ex vivo AAA samples in MPI images was determined by integration of overall iron in the VOI over the AAA, after applying a 50% threshold, to minimize BG artifacts.

### **3.7 Histological analysis and immunohistology**

MPI results were correlated to histology and immunohistology. The histochemistry and immunohistology was carried out by Dilyana Mangarova. MNP deposition in AAA was visualized by Perls' Prussian blue staining in paraffin sections, 9  $\mu\text{m}$  thick, with additional Hematoxylin and Eosin staining to study the AAA morphology. Immunofluorescence staining with macrophage specific antibody, CD68, was used for localizing macrophages and correlating them with tissue iron. For more information, please see [27].

### **3.8 Determination of MRI blood half-life of MCP-PEG**

For optimization of MCP MNP for angiographic imaging, the MCP surface was modified by PEGylation. Blood  $t_{1/2}$  time was determined by MR imaging, since the MCP-PEG produce bright intravascular signal in a T1-weighted sequence. The rats were scanned pre and post MCP-PEG injection in intervals of 10 mins. Images were acquired in a clinical 3-Tesla scanner (Magnetom Lumina, Siemens, Germany) using an extremity coil. T1-weighted MR images were acquired with a 3D fast low-angle shot (FLASH) sequence in coronal slice orientation using the following sequence parameters: repetition time (TR) = 6.57 ms, echo time (TE) = 1.95 ms, flip angle (FA) = 25°, FOV= 300 × 300 mm, matrix size = 784 × 896 (reconstructed pixel size = 0.3 x 0.3 mm), and slice thickness = 0.6 mm, 80 slices, bandwidth of 130 Hz/Px. Blood  $t_{1/2}$  was determined from the T1-weighted images. For this the SNR was determined as

the average signal intensity (SI) of 3 defined ROIs in the abdominal aorta over the average value of BG SI (several ROIs). The  $SNR_{pre}$  was subtracted from the  $SNR_{post}$  values to eliminate the underlying tissue signal. The values were plotted versus time and fitted by single-order kinetics in Matlab.

### **3.9 Cell culture and uptake of MNP**

THP-1 cells (human acute monocytic leukemia cell line) were obtained from ATCC (Wesel, Germany), cultured in suspension in RPMI medium 1640 (Gibco, Germany) supplemented with 10% fetal calf serum (FCS, Gibco, Germany) and 100 U/ml penicillin, 100  $\mu$ g/ml streptomycin (Gibco, Germany). THP-1 monocyte cells were differentiated into THP-1 macrophages (THP-M $\Phi$ ) by incubation with 20 ng/ml phorbol-12-myristate-13-acetate (PMA). After 72 h, the PMA supplemented media was removed, cells were washed with medium and rested in fresh PMA-free medium for further 24 h in order to obtain phenotypic characteristics of macrophages. The THP-M $\Phi$  were incubated with MNP at an iron concentration of 0.75 mM [8] in medium supplemented with 1% FCS. Thereafter the cells were stained for iron uptake visualization using Prussian blue and nuclear fast red stain.

## 4. Results

This chapter contains key results published in *Nanomaterials* (2019) (Publication A) [12], *Scientific Reports* (Oct. 2020) (Publication B) [26] and *Scientific Reports* (July 2020) (Publication C) [27]. In the last section of this chapter results from a manuscript currently in preparation are presented (Publication D).

### 4.1 Evaluation of the tracer performance by their MPS and MPI spectra

The results in this section are presented due to their fundamental relevance to the present work, which forms the basis of the subsequent studies. Screening of MNP spectra using MPS allows rapid evaluation of the potential applicability of an MNP-product for MPI. MPS measurements of aqueous MNP solutions revealed remarkably stronger signal amplitudes for MCP, 5 times higher, compared to Resovist. The immobilized MCP sample in Polyacrylamide (PAA) gel (4.2%) show a decreased amplitude and a faster decay of the spectrum compared to the mobile MCP in the aqueous solution. However, the signal amplitude is still higher than that of Resovist, 3 times higher (Figure 5a). The MPI spectrum is a combination of mixed frequency components and hence differs from MPS spectrum. Yet the magnitude of the amplitude of the MPI signal of MCP is higher, especially in higher harmonics (Figure 5b).

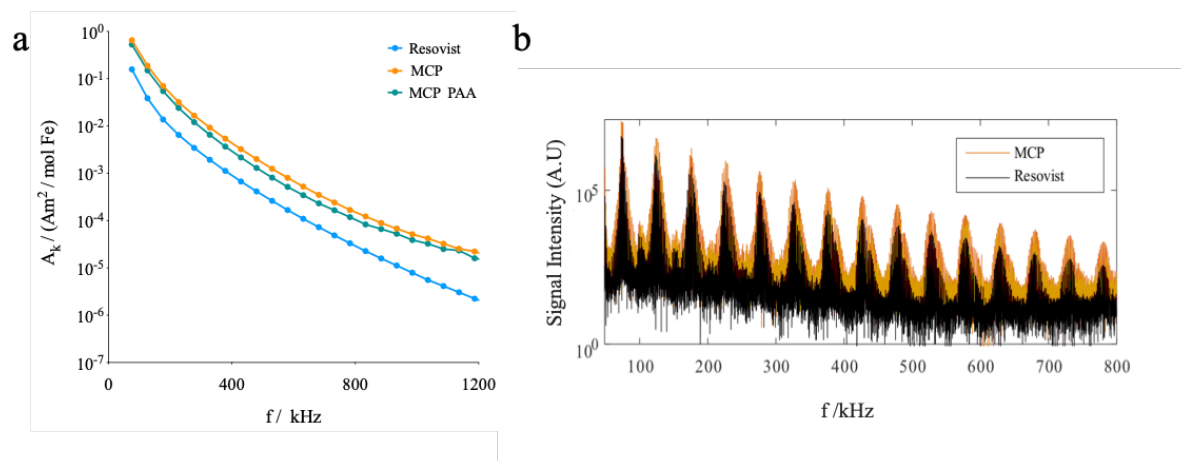


Figure 5. (a) MPS spectrum of MCP in aqueous dispersion (orange), immobilized MCP in PAA (green), and Resovist (blue) in aqueous dispersion measured at 10 mT and 25 kHz [12]. (b) MPI spectra of MCP and Resovist in water dispersion normalized to the iron [26].

### 4.2 Evaluation of reconstruction parameters in single-tube phantoms

As mentioned in section 2.2.3, images were reconstructed using Kaczmarz's algorithm with Tikhonov regularization. The choice of the optimal value for the regularization parameter  $\lambda$  is

crucial for image denoising.  $\lambda$  has a smoothing effect. If the value of  $\lambda$  is chosen too large, the image is oversmoothed, leading to loss of object geometry. If the value of  $\lambda$  is too small, the regularization term will only slightly affect the solution such that the denoising is not effective (Figure 6).

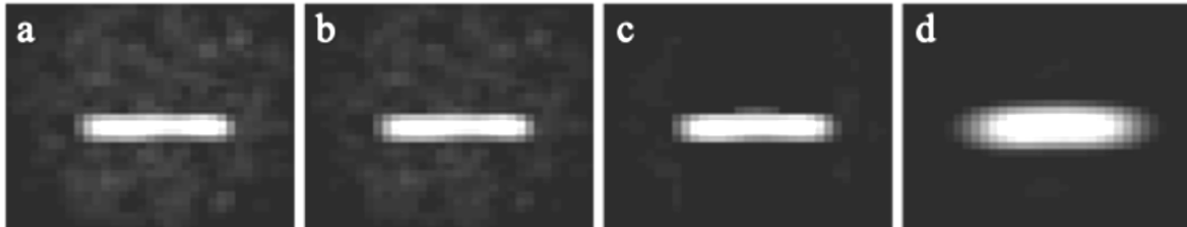


Figure 6. Maximum intensity projection of a single tube phantom with a concentration of 2 mmol Fe/L MCP in the x-y plane. The  $\lambda$  values for a-d are  $10^{-6}$ ,  $10^{-2}$ ,  $10^{-1}$ ,  $10^1$ . Over-regularization leads to over-smoothing of the edges and to blurring (d), and an under-regularization leads to only limited noise suppression (b). Inconsistent selection of reconstruction parameters leads to unreliable qualitative and quantitative results.

By varying  $\lambda$  in a range of  $10^{-6}$ - $10$  multiple image sets were reconstructed, and the image quality of each set was measured by SNR and plotted over  $\lambda$  for MCP and Resovist (Figure 7). Both tracers showed the highest SNR in the range of  $\lambda = 10^{-2}$ - $10^{-1}$ , particularly at lower concentrations ( $<2$  mmol Fe/l), which is substantial for in vivo research. The SNR contributed by MCP is more robust to variations of  $\lambda$  comparing to Resovist, showing a nearly constant SNR at  $\lambda$ -values below  $10^{-3}$ , at the same time showing duplicate the SNR of Resovist at the same  $\lambda$ s. This suggests that SNR values of Resovist are highly dependent on the  $\lambda$  applied. Overall, MCP shows a higher SNR than Resovist.

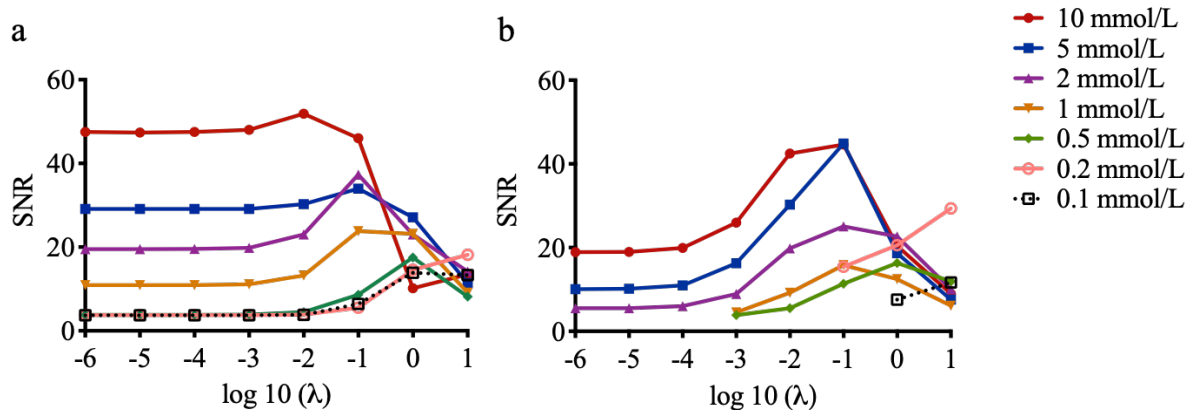


Figure 7. Signal-to-noise ratio (SNR) of single tube phantom reconstructed with different regularization factors ( $\lambda$ ) plotted over for MCP 3 (a) and Resovist (b). [12]

At concentrations below 2 mmol Fe/l for Resovist the objects were fairly indiscernible from BG artifacts in the  $\lambda$ -range of  $10^{-3}$ - $10^1$  and SNR determination was not possible. Iron amounts down to 500 ng were quantifiable with MCP while the limit for Resovist was 1  $\mu$ g. To reduce

variability, two other reconstruction parameters of the algorithm, the number of iterations, i.e., 5, and number of frequency components ( $N_f$ ) employed, were maintained the same for both tracers, i.e., 2438 frequencies.

The MPI-quantified amount of iron in the single-tube phantoms, reconstructed with the aforementioned parameters, was in good agreement with actual iron content, especially for MCP. The volumetric results in the same phantoms also correlated well with the nominal volume values for MCP, with average deviation from actual volume values for concentrations above 1 mmol Fe/L 2,5% and below 1 mmol Fe/L 6,5% in the x-y plane. The deviation from the true volume was considerable for Resovist, with an average of 36,5% for all concentrations that could be visualized reasonably, above 0,5 mmol Fe/L (Figure 8). More details can be found in publication A. The defined set of reconstruction parameters which led to better noise reduction, qualitative spatial resolution, conspicuity and overall image quality were then employed for in vitro and in vivo image reconstruction in subsequent experiments.

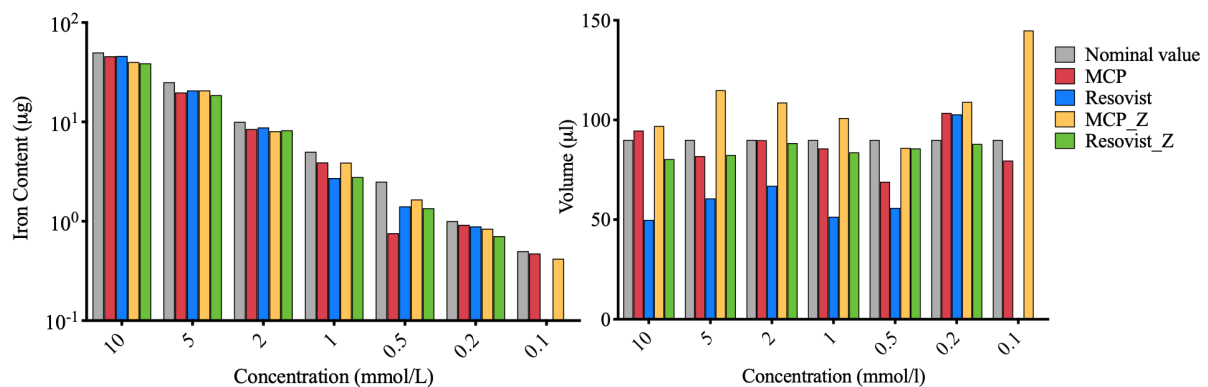


Figure 8. Quantified iron mass (left panel) and volume (right panel) calculated from single-tube phantoms in dilution series. [12]

### 4.3 Evaluation of vessel phantoms

Given the higher spatial resolution in z-direction – resulting from the higher gradient strength and hence anisotropic spatial resolution - the phantoms were measured in two directions, either aligned longitudinally to x- or to z-axis. Some representative phantom images are provided in Figure 9. Tubes of the same diameter (3, 2, 1 mm) containing identical concentrations of iron (1 and 10 mmol Fe/L), distanced apart 1 mm, were resolvable from one another for MCP in all cases in the x-z plane and x-y plane, except for 1 mm tubes in the x-y plane. For Resovist, the tube vessels with 1 mm inner diameter were not resolvable at all in the x-y plane at 10 and 1 mmol Fe/L and poorly resolvable in the x-z plane at 10 mmol Fe/L. At a concentration of 1 mmol Fe/L in the x-y plane, the Resovist phantoms with 2 mm internal diameter appear as a

single entity. The results indicate that the achievable spatial resolution with MCP in combination with the MPI scanner system used for imaging, is 1mm or even better. It is observed that while maintaining the same tracer concentration (10 mmol/L), a smaller structure in the vicinity of a larger object will not be distinguishable in image reconstructions. The effect was observed here in phantoms with inner diameter combinations of 3 and 1, and 2 and 1 mm with respective iron amount ratio of 9:1 and 4:1. We refer to this phenomenon as the "shadowing effect" which turns more apparent as the ratio between the objects containing two different quantities of iron increases.

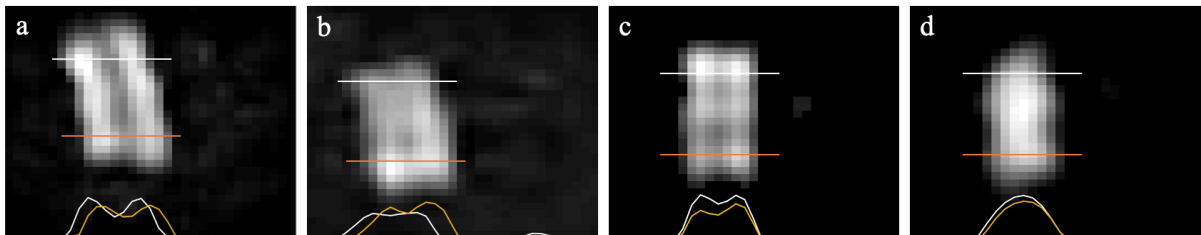


Figure 9. Representative examples of the assessed spatial resolution in vessel phantoms for MCP (a,c) and Resovist (b,d). The two adjacent tubes have an inner diameter of 1 mm in (a,b) and 2 mm in (c,d), and the tracer concentrations are 10-(a,b) and 1 mmol Fe/L (c,d). The distance between the MNP solutions is 1 mm. The images (a,b) are acquired in the x-z plane, parallel to the higher gradient and (c,d) in the x-y plane. At the lower iron concentration, the tubes are resolvable only with MCP but not Resovist. Images are represented as maximum intensity projection. Images were thresholded to eliminate BG artifacts for better visualization (c,d), modified from [12].

#### 4.4 Angiography of inferior vena cava and abdominal aorta in healthy rat model

With the real-time imaging capability of MPI, the temporal profiles of the iron concentration curves allow exact recording of the bolus arrival time in IVC and AA. The venous  $C_{max}$  at time point  $t_1$  is well detected but not the aortic peak (aortic  $C_{max}$ ), since the bolus is passing through the AA after the first cardiopulmonary passage and is diluted. By AA passage of the MNP, the gradual and reduced signal rise at time  $t_2$  (approx. 2–3 s after initial tracer administration) did not allow the identification of an exact aortic  $C_{max}$ . Subsequently, single time images were reconstructed at the times pre, main and post venous  $C_{max}$ . Qualitatively, the reconstructed images of the IVC at main and post venous  $C_{max}$  did not reveal a major difference except for Resovist at 0.025 mmol Fe/Kg (see supplementary data publication B). This indicates, that venous  $C_{max}$  reconstruction might be beneficial when a smaller amount of tracer is applied. The images of the AA passage of the MNP indicated in Figure 11 (red) were reconstructed at time  $t_2$  shown in Figure 10.

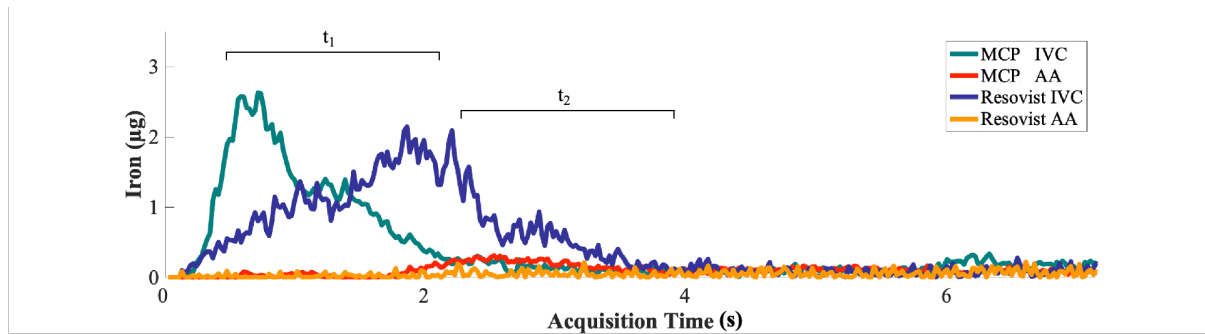


Figure 10. Dynamic iron concentration curve of first pass IVC ( $t_1$ ) and in AA ( $t_2$ ) for MCP and Resovist, in the VOI defined in imaging data acquired. Shown here is the curve for the administered dosage of 0.05 mmol Fe/kg one animal per MNP. The venous  $C_{max}$  is marked by  $t_1$  and the passage of the MNP in AA signal rises by  $t_2$ . The profiles of curves vary from one another due to different injection speeds as the injections were manual. [26]

The reconstructed images from two time points, i.e., of first IVC passage of the MNP ( $t_1$ ) and AA passage of the MNP ( $t_2$ ), overlaid are shown in Figure 11. While the IVC is discernible with both tracers at all dosages, the AA is visible with adequate morphological detail only at administered dosages of 0.1 and 0.05 mmol Fe/kg for MCP. Additionally, qualitatively the results exhibit that, even for MCP, the lowest of the 3 doses investigated, 0.025 mmol Fe/kg, is insufficient to generate an adequate signal for MPI angiography in rats. Our results indicate that a MCP dose of more than 0.05 mmol Fe/kg is required for angiographic imaging in rats.

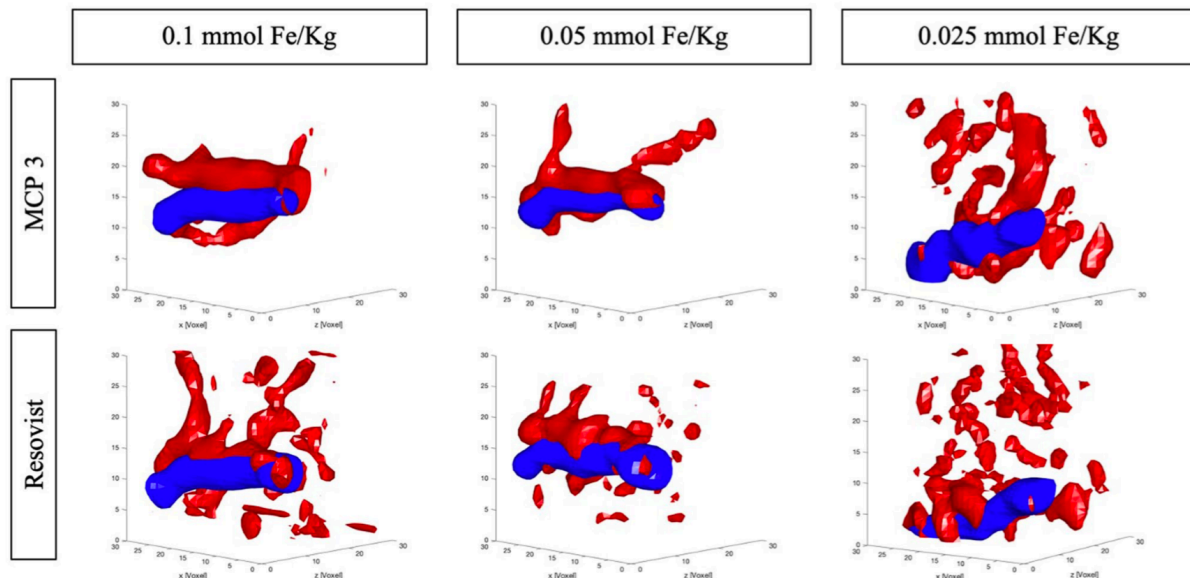


Figure 11. Representative in vivo MPI angiographic images of the IVC (blue) and AA (red) in rats at three dosages tested. The first pass in AA is perceptible by application of higher dosages of MCP, while the AA is barely detectable by application of Resovist. The Resovist-MPI images have overall poorer image quality. [26]

As predicted from the phantom studies, in vivo delineation of AA from IVC is hardly feasible. To delineate the AA from the IVC, a MPI digital subtraction step, as explained in section 3.6,

was performed which allowed clear separation and individual examination of the two adjacent vessels. Determination of the  $D_L$  along the vessel was feasible only with MCP and at concentrations of 0.1 and 0.05 mmol Fe/kg (Figure 12). The mean  $D_L$  calculated along the AA and IVC for 0.1 mmol Fe/kg was: IVC =  $2.7 \pm 0.7$ , AA =  $2.5 \pm 0.7$ ; and for 0.05 mmol Fe/kg: IVC =  $2.8 \pm 0.6$ , AA =  $2.3 \pm 0.8$  mm.

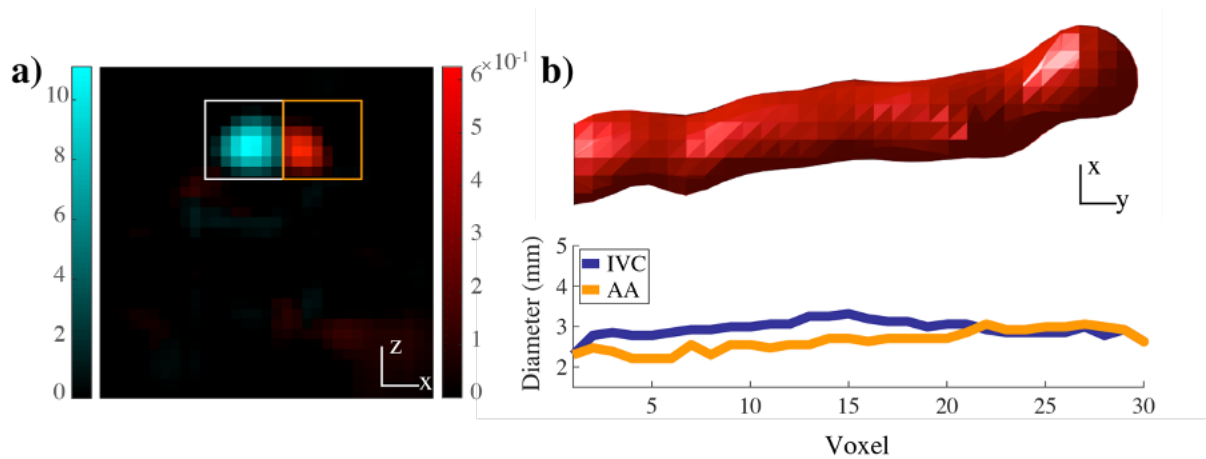


Figure 12. The AA isolated by subtraction of IVC passage of the MNP from time of AA passage of the MNP after i.v. injection of MCP at a dosage of 0.1 mmol Fe/kg. Shown are cross-sections of the isolated AA (marked with orange square) overlaid with the IVC (marked with white square) (a) and the isolated AA in coronal orientation (b) and respectively their  $D_L$ . Color bar values in (a) and are in  $\mu\text{g}$ . [26]

#### 4.5 Ex vivo MPI of vascular inflammation in abdominal aortic aneurysm in mouse model

24 h post i.v. Resovist administration the AAA were harvested and imaged ex vivo by MPI, measured with MPS for validation of quantification results of MPI and histologically processed. Reconstruction of images and quantification of MNP amount in the arterial wall of AAA in both MPI and MPS was performed using an immobilized sample acquiring the SF. The quantitative iron amount as determined from MPI was confirmed by quantitative results using MPS ( $y = 1.05x + 0.03$ ,  $R=0.99$ ,  $p < 0.05$ ). The smallest Fe amounts visualized in MPI in two AAA samples were 311 and 373 ng Fe, as determined by MPS. Due to remaining BG noise, the AAA containing above 500 ng Fe and below 1  $\mu\text{g}$ , MPI deviated slightly from nominal values, measured with MPS. The average deviation of total iron amount determined by MPI from MPS for AAA containing above 500 ng iron and below 1  $\mu\text{g}$  was 20.6%, and for samples above 1  $\mu\text{g}$  8.3%. The correlated Perls' Prussian blue stained sections revealed abundant iron within AAA specimens and anti-CD68 monoclonal antibody immunohistology revealed abundant macrophage accumulation in the adventitial area of the aneurysm (For more information please see Publication C).

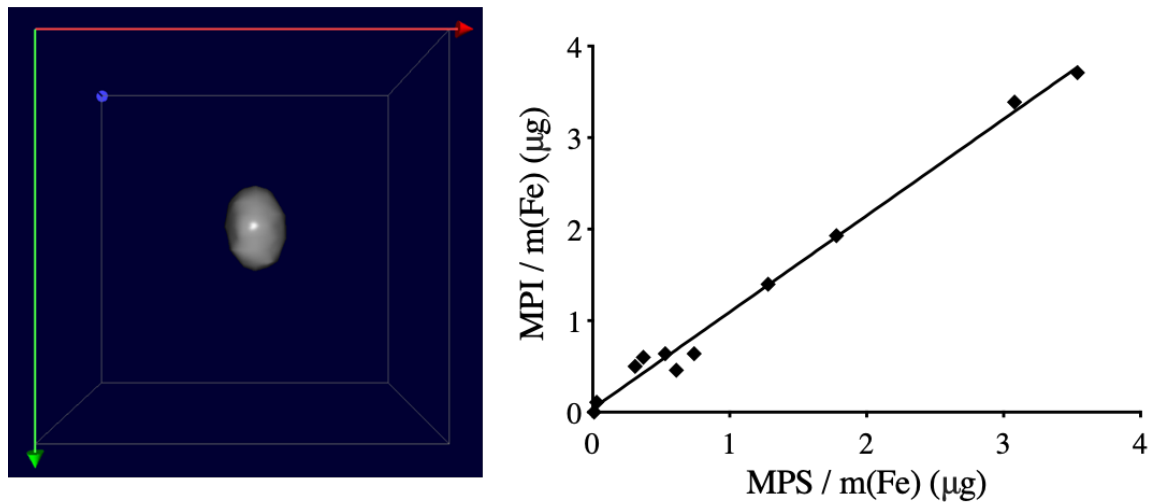


Figure 13.(a) Isosurface-rendered MPI image of an ex vivo AAA sample visualized in Paravision (b) Validation of quantification results of iron amount in ex vivo MPI with MPS measurements ( $R=0.99$ ). No or little iron was detected in the control group.  $P<0.05$ . [27]

#### 4.6 Prolongation of blood half-life of MCP

The blood  $t_{1/2}$  time of the successfully PEGylated MCP as determined using T1-weighted MRI is presented here as partial results to the study. The blood  $t_{1/2}$  of MCP-PEG within the three measurements was 44.9, 54.5 and 85.4 min, resulting in a mean MRI blood  $t_{1/2}$  of 61.6 min at the dosage of 0.05 mmol Fe/kg.

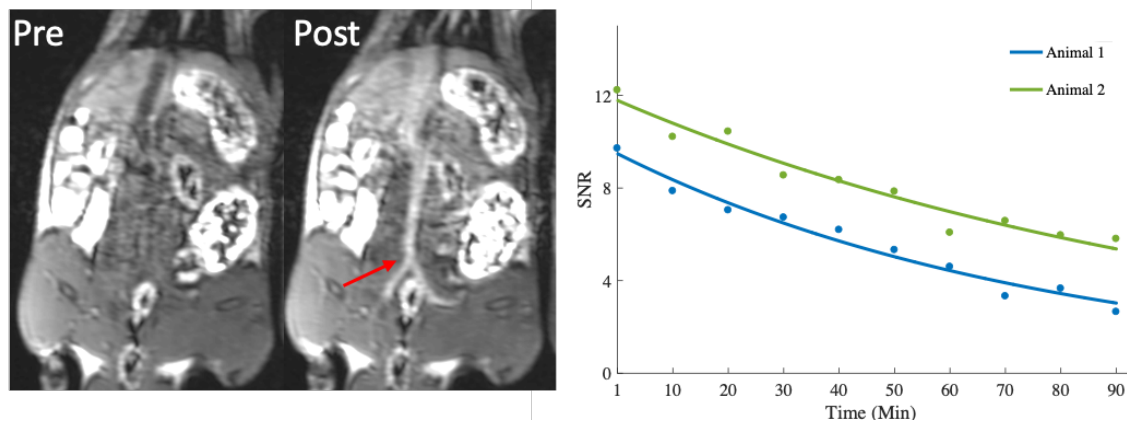


Figure 14. T1-weighted coronal MR images were acquired serially and following i.v. injection of MCP-PEG in rats and are shown here at representative time points (pre, 10 min post administration, left panel). Signal intensities pre- and post-injection of the abdominal aorta (red arrow) were fitted to first-order kinetics to obtain blood clearance (representative graph  $n=2$ ).

THP-M $\Phi$  were investigated as a simplified model of activated macrophages to visually examine the uptake of MNP after 24 h incubation and stained with Prussian blue. Resovist and MCP-CMD were efficiently internalized into the cells under the incubation conditions, whereas for MCP-PEG an evasion of phagocytic uptake in THP-M $\Phi$  was observed.

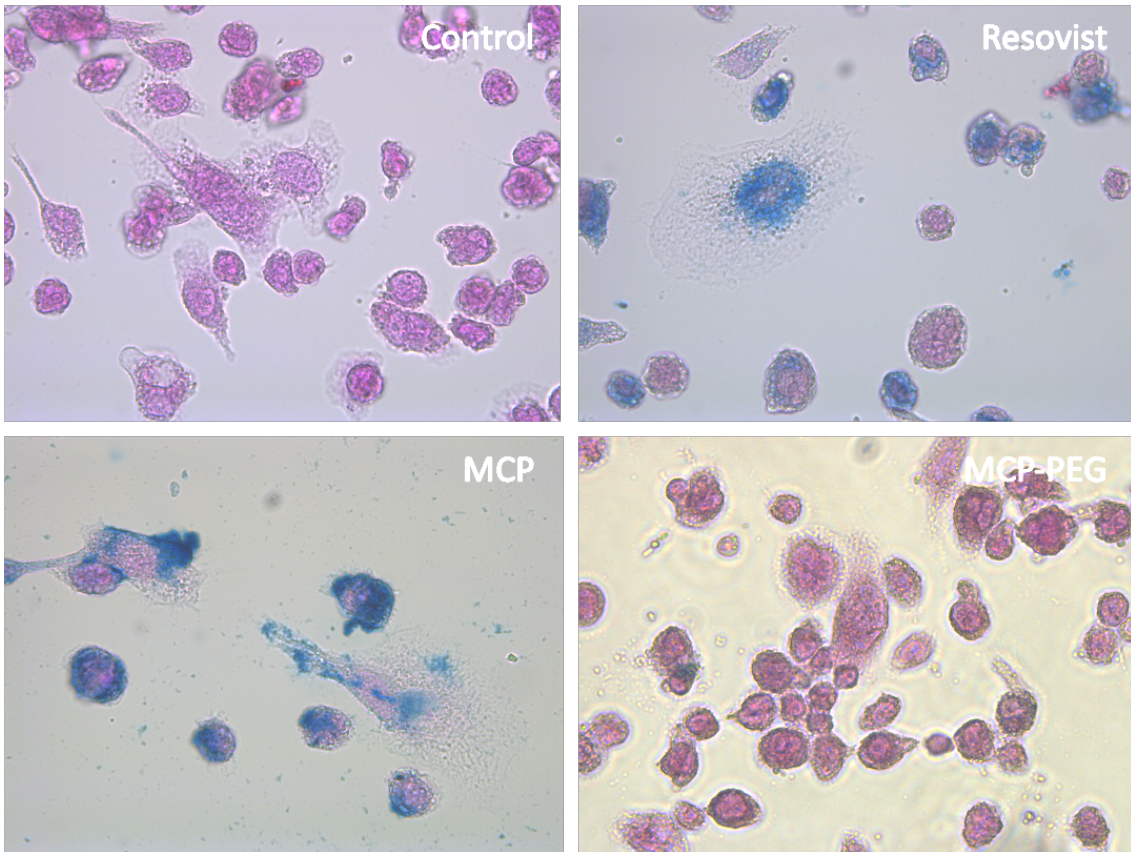


Figure 15. Prussian blue stain of phagocytized MNP in THP-MΦ cells, period of incubation 24 h with 0.75 mmol Fe/l. Cells incubated without MNP served as control.

## 5. Discussion

Within this work, the development of MPI including MNP for vascular imaging is presented. For this, the employment of a MPI suitable MNP was required. The MCP, developed in our group, contributed to the MPI image quality in phantom studies and further on allowed time-resolved quantitative imaging of the passage of MNP in IVC and AA. The gain in image quality was obvious from the first measurements of cylindrical phantoms, where for MCP compared to Resovist an improved SNR, with a SNR twice as high for MCP, resulting in a higher spatial resolution in the order of 1 mm or even submillimeter and higher sensitivity was observed.

In addition to the MNP employed for MPI and acquisition parameters, reconstruction techniques and reconstruction parameters affect both qualitative and quantitative results of MPI. Therefore, a method of standardization of image reconstruction parameters based on phantom studies, with respect to their quantitative information, iron content and volume, was introduced in this work and applied to further in vivo studies. In MPI reconstruction using a Kaczmarz's algorithm with Tikhonov regularization, three parameters can be varied: The  $\lambda$ , the number of iterations, and  $N_f$ , which is adjusted by tuning of the SNR ratio of the SF used. In section 4.2, determination of  $\lambda$  based on the highest SNR was predominantly addressed, while maintaining iteration number and  $N_f$  the same for all reconstructions. A higher number of iteration steps leads to convergence of the correct solution, allowing a more accurate reconstruction of object geometry, however at the cost of a higher computation time. Five iteration steps provided a satisfactory trade-off between image quality and computation time. A lower number of frequencies leads to blurring of the image and loss of sensitivity in geometrical integrity. The iron content and volume, obtained from the single-tube images reconstructed with aforementioned parameters, were in good agreement with nominal values using MCP. This indicates that MCP is reliable for volume estimation and area calculation, which can be employed in applications such as for determination of the volumes of pathologic changes, where MNP accumulate.

In angiography study, MCP at a dosage of 0.1 and 0.05 mmol Fe/kg allowed good appreciation of the AA. Since the spatial resolution of MPI is limited, by image post-processing, a subtraction step, inspired from digital subtraction angiography (DSA), with subtraction of an early MNP passage, at bolus arrival time, from a later temporally distanced MNP passage based on the dynamic MNP concentration curve, allowed examination of  $D_L$  along the AA and IVC. Therewith, with the focus on the subsequent MPI image analysis task, a workflow for  $D_L$  assessment, e.g., for stenosis or aneurysm imaging in abdominal aorta and their quantification

in an experimental setting was introduced. Furthermore, the MCP dose required for angiographic imaging in rats was determined not far above the maximum permissible dose of clinically approved iron oxide nanoparticles such as Resovist for clinical MRI, which is 0.04 mmol Fe/kg [28]. The results of MPI-determined  $D_L$  in rats were not far away from real values observed in other imaging studies [29], with a slight overestimation. This overestimation could be attributable to partial volume effects, mismatch of the calibration sample (SF) environment and the MNP local environment in vivo or the reconstruction parameters, e.g., over-regularization. Deviation from nominal values of stenosis phantoms diameter has been observed previously [30]. It can be proposed that by application of the appropriate MPI-MNP, here MCP, delineation of vascular abnormalities such stenosis, occlusion, or even aneurysmal dilatation and  $D_L$  alteration, with high temporal resolution combined with quantitative measurement of tracer concentration, is achievable by MPI.

In Publication C, the ability of MPI for imaging vascular inflammation in AAA by passive targeting was shown in an ApoE<sup>-/-</sup>AAA mouse model, ex vivo. The colocalization of iron positive areas, Prussian blue staining and Laser ablation inductively coupled plasma mass spectrometry, with macrophages in histological sections, confirmed the uptake of MNP in macrophages. To this date, some MRI studies have demonstrated uptake of ultra-small IONs in the aortic wall of AAA and correlated the results with macrophage activity and cellular inflammation [31, 32]. One hypothesis regarding the accumulation of MNP in macrophages in AAA wall is that the wandering phagocytes, in the blood and tissue, phagocytize the nanoscale objects introduced through the vasculature [9] and eventually infiltrate the pathologic tissue [32]. The mechanism is presumably facilitated by recognition of protein absorbed on the surface of MNP, which is dependent on the size and charge of MNP [33], by receptors on the surface of the phagocytes [9]. The micro-defect architecture of the AAA wall and the remodeled extracellular matrix (ECM) could also enhance the penetration of MNP into tunica media and adventitia [32] and consequent phagocytosis by tissue resident macrophages. Alternatively, it has been proposed that the negatively charged MNP coating can be exchanged in vivo by the ECM via transchelation [8, 34]. Therefore, the MNP cores have a binding affinity to the altered glycosaminoglycans in the pathologic ECM. Whether both mechanisms simultaneously lead to accumulation of MNP in the AAA wall, remains an open question. In MPI, the environment of the MNP influences its magnetization behavior and therefore theoretically the possibility arises to distinguish between the intracellular MNP and the MNP interactions in ECM, e.g., by use of multicolor MPI [4]. However, the magnetic behavior of MNP in biological tissue, whether intracellular or in ECM, is more complex, due to

interparticle interactions, ranging from dipole-dipole interactions to aggregation [9], hence their distinguishment using multicolor MPI, with the current technical state of technique even if plausible, is very challenging. The approach taken in publication C, was adjustment of the calibration step (SF) in a general term to mimic the immobilized state of MNP in the tissue based on MPS A5/A3 ratio measurements [8]. Thus, identification of inflammatory cellular activity within vascular tissue in a quantitative manner was possible, with the substantial benefit of inducing positive contrast in comparison to MRI, where the signal void due to ION can be missed or mistaken for an artifact.

For applications such as angiography and blood pool imaging a prolonged blood  $t_{1/2}$  and prevention of serum-protein adsorption on the MNP is favorable. Stealth coating of the MNP with PEG is an efficient approach [35]. At the time of submission of this doctoral thesis, the MCP used in this section of the work have been successfully PEGylated, characterized and investigated in vivo (manuscript in preparation). The PEGylation increases the MNP dispersion stability, reduces the interaction with serum proteins which promote phagocytosis [33] and thereby prolongs the blood  $t_{1/2}$  time. The reduced adsorption of blood proteins and biomacromolecules on MCP-PEG could minimize the possible deviation of dynamic magnetization behavior of MNP in the SF sample used for calibration and the MNP in the bloodstream. The nearly neutral surface charge of MCP-PEG also contributes to the stealth effect and evasion from uptake by immune cells [9]. Resovist and MCP have highly negative surface charges and therefore are prone to rapid uptake by immune cells [8, 9], like THP-M $\Phi$  as shown in the current study and previously for RAW 264.7 [7]. By implementation of the MPI-tailored MNP, imaging of inflamed pathobiology might be possible with improved spatial resolution and sensitivity.

Our studies encountered limitations. The theoretical sensitivity limit of MPI, predicted in picogram range [16], is much lower than the sensitivity achieved in this study. Published studies have reported sensitivities below 100 ng [24, 36], however for concentrated iron amounts in a point-like volume, also using coils with smaller inner dimeters [37] leads to higher sensitivity. Sensitivity differs for diluted samples in larger volumes as reported in this study. Yet detection of small iron amounts in concentrated small volumes is only beneficial for certain medical applications, such as localized inflammation or metastasis imaging, whereas 3D delineation of imaged structures is essential in other applications such as angiography. With diluted MCP at a concentration of 0.1 mmol Fe/l, the shape of cylindrical phantoms containing 500 ng iron was nearly recovered despite the high BG artifacts. In ex vivo AAA examinations,

the limit of detection of Resovist in tissue was in the same range, with the smallest tracer amounts visualized in MPI having nominal MPS measured iron amounts of 300-500 ng Fe. The “shadowing effect” observed in the vessel phantoms, i.e., limitation in resolving large MNP amount differences in the FOV, has been reported before [38], and could be attributed as a reconstruction algorithm problem and is a substantial challenge that should be taken into consideration for in vivo imaging, for instance, in angiographic imaging [39], where neighboring smaller vessels, or adjacent blood vessels containing different iron contents, due to distribution in blood stream, are in close vicinity of each other. Another example is imaging of structures in proximity of the liver or spleen, where MNP are sequestered by the RES. The high accumulation of MNP in these organs makes imaging of nearby structures challenging. Implementation of other reconstruction algorithms [38, 40] and a thorough analysis of correlation of reconstruction parameters or implementation of other reconstruction algorithms will provide useful knowledge to overcome the “shadowing effect” and to improve the image quality. Additionally, the theoretical MNP physics is rather complex and current theories and simulations do not predict exact outcome of the MPI measurements. The experimental exploration and analytical theoretical description will pave the way for more accurate quantitative MPI.

## 6. Conclusion and outlook

Within this work, we demonstrated the use of MPI in the field of vascular imaging and the MPI performance of newly developed tracers tailored for MPI, in vitro and in vivo towards high resolution MPI. The applicability of MPI for structure-sensitive angiographic imaging and cellular imaging of activated macrophages in vascular inflammation in AAA was shown. Furthermore, with respect to the subsequent MPI image analysis task, a workflow for in vivo MPI bolus tracking in the confined FOV with measurement of vessel lumen diameters was introduced. To our knowledge, this is the first study that demonstrates the potential of MPI for assessment of inflammatory processes in the aneurysmal wall. Even though the two studies were conducted in different animal models and with two different MNP, results suggest that the MPI technique is useful in the diagnostic work-up of vascular disease and for cellular imaging of activated macrophages within the vessel wall with tracer quantification possibility through a single MNP application. In further work, the altered pharmacokinetics of MPI optimized MNP, PEGylated MCP, for new MPI applications such as cardiovascular applications, was shown. Within the scope of this work the MCP and Resovist as MPI tracers were used, but comparison with other MPI suitable MNP, such as Synomag [4] and Perimag [5] would give further valuable insights. Furthermore, investigations on feasibility of implementation of multicolor MPI [4] for distinguishing the intracellular MNP and extracellular MNP in biological tissue can provide useful insights to pathological tissue changes. The FOV in the current scanner setup covers a relatively small core volume in the center of the pickup coil. An additional hardware upgrade in the future, by installation of focus fields [41], will allow the volume covered by the Lissajous trajectory to be shifted and thus a larger sized FOV is achieved. Future studies building on the results presented here can be conducted to investigate applications of MCP and MCP-PEG MNP for structure-sensitive, high-resolution MPI in the same or other medical scenarios, in particular in the field of vascular imaging. The simultaneous quantitative imaging of progressive alteration of the vessel lumen and vascular inflammation with MPI could be of particular interest. MPI is an emerging technology in which many parameters remain to be optimized. The efforts in the presented work address current improvements, challenges and limitations of in vivo MPI with our MPI scanner and tracers applied, and simultaneously open doors to improved resolution, sensitivity, image quality, and new potential medical applications for MPI.

## 7. References

1. Gleich B, Weizenecker J. Tomographic imaging using the nonlinear response of magnetic particles. *Nature*. 2005;435(7046):1214-7.
2. Goodwill PW, Conolly SM. The X-space formulation of the magnetic particle imaging process: 1-D signal, resolution, bandwidth, SNR, SAR, and magnetostimulation. *IEEE Trans Med Imaging*. 2010;29(11):1851-9.
3. Graeser M, Thieben F, Szwargulski P, Werner F, Gdaniec N, Boberg M, Griese F, Moddel M, Ludewig P, van de Ven D, Weber OM, Woywode O, Gleich B, Knopp T. Humanized magnetic particle imaging for brain applications. *Nat Commun*. 2019;10(1):1936.
4. Paysen H, Loewa N, Stach A, Wells J, Kosch O, Twamley S, Makowski MR, Schaeffter T, Ludwig A, Wiekhorst F. Cellular uptake of magnetic nanoparticles imaged and quantified by magnetic particle imaging. *Sci Rep*. 2020;10(1):1922.
5. Kosch O, Paysen H, Wells J, Ptach F, Franke J, Wöckel L, Dutz S, Wiekhorst F. Evaluation of a separate-receive coil by magnetic particle imaging of a solid phantom. *Journal of Magnetism and Magnetic Materials*. 2019;471:444-9.
6. Kaul MG, Mummert T, Jung C, Salamon J, Khandhar AP, Ferguson RM, Kemp SJ, Ittrich H, Krishnan KM, Adam G, Knopp T. In vitro and in vivo comparison of a tailored magnetic particle imaging blood pool tracer with Resovist. *Phys Med Biol*. 2017;62(9):3454-69.
7. Kratz H, Taupitz M, Ariza de Schellenberger A, Kosch O, Eberbeck D, Wagner S, Trahms L, Hamm B, Schnorr J. Novel magnetic multicore nanoparticles designed for MPI and other biomedical applications: From synthesis to first in vivo studies. *PLOS ONE*. 2018;13(1):e0190214.
8. Poller WC, Lowa N, Wiekhorst F, Taupitz M, Wagner S, Moller K, Baumann G, Stangl V, Trahms L, Ludwig A. Magnetic Particle Spectroscopy Reveals Dynamic Changes in the Magnetic Behavior of Very Small Superparamagnetic Iron Oxide Nanoparticles During Cellular Uptake and Enables Determination of Cell-Labeling Efficacy. *J Biomed Nanotechnol*. 2016;12(2):337-46.
9. Krishnan KM. Biomedical Nanomagnetism: A Spin Through Possibilities in Imaging, Diagnostics, and Therapy. *IEEE Trans Magn*. 2010;46(7):2523-58.
10. Kratz H, Eberbeck D, Wagner S, Taupitz M, Schnorr J. Synthetic routes to magnetic nanoparticles for MPI. *Biomed Tech (Berl)*. 2013;58(6):509-15.

11. Wells J, Kazakova O, Posth O, Steinhoff U, Petronis S, Bogart LK, Southern P, Pankhurst Q, Johansson C. Standardisation of magnetic nanoparticles in liquid suspension. *J Phys D: Appl Phys*. 2017;50(38).
12. Kratz H, Mohtashamdolatshahi A, Eberbeck D, Kosch O, Hauptmann R, Wiekhorst F, Taupitz M, Hamm B, Schnorr J. MPI Phantom Study with A High-Performing Multicore Tracer Made by Coprecipitation. *Nanomaterials (Basel)*. 2019;9(10):1466.
13. Borgert J, Gleich B, Buzug TM. Magnetic Particle Imaging In: Kramme R, Hoffmann K, Pozos RS, editors. *Springer Handbook of Medical Technology*: Springer, Berlin, Heidelberg; 2011. p. 461-76.
14. Knopp T, Buzug TM. *Magnetic Particle Imaging An Introduction to Imaging Principles and Scanner Instrumentation*: Springer-Verlag Berlin Heidelberg; 2012.
15. Ferguson RM, Minard KR, Khandhar AP, Krishnan KM. Optimizing magnetite nanoparticles for mass sensitivity in magnetic particle imaging. *Med Phys*. 2011;38(3):1619-26.
16. Gleich B. *Principles and Applications of Magnetic Particle Imaging*: Springer Vieweg; 2013.
17. Szwargulski P, Rahmer J, Ahlborg M, Kaethner C, Buzug TM. Experimental evaluation of different weighting schemes in magnetic particle imaging reconstruction. *Current Directions in Biomedical Engineering*. 2015;1(1):206-9.
18. Goodwill PW, Konkle JJ, Zheng B, Saritas EU, Conolly SM. Projection x-space magnetic particle imaging. *IEEE Trans Med Imaging*. 2012;31(5):1076-85.
19. Saritas EU, Goodwill PW, Croft LR, Konkle JJ, Lu K, Zheng B, Conolly SM. Magnetic particle imaging (MPI) for NMR and MRI researchers. *J Magn Reson*. 2013;229:116-26.
20. Reimer P, Balzer T. Ferucarbotran (Resovist): a new clinically approved RES-specific contrast agent for contrast-enhanced MRI of the liver: properties, clinical development, and applications. *Eur Radiol*. 2003;13(6):1266-76.
21. Eberbeck DW, F. Wagner, S. Trahms, L. How the size distribution of magnetic nanoparticles determines their magnetic particle imaging performance. *Appl Phys Lett*. 2011;98(18):182502.
22. Hamm B, Staks T, Taupitz M, Maibauer R, Speidel A, Huppertz A, Frenzel T, Lawaczek R, Wolf KJ, Lange L. Contrast-enhanced MR imaging of liver and spleen: first experience in humans with a new superparamagnetic iron oxide. *J Magn Reson Imaging*. 1994;4(5):659-68.

23. Haegele J, Duschka RL, Graeser M, Schaecke C, Panagiotopoulos N, Ludtke-Buzug K, Buzug TM, Barkhausen J, Vogt FM. Magnetic particle imaging: kinetics of the intravascular signal in vivo. *Int J Nanomedicine*. 2014;9:4203-9.
24. Paysen H, Wells J, Kosch O, Steinhoff U, Franke J, Trahms L, Schaeffter T, Wiekhorst F. Improved sensitivity and limit-of-detection using a receive-only coil in magnetic particle imaging. *Phys Med Biol*. 2018;63(13):13NT02.
25. Weber A, Werner F, Weizenecker J, Buzug TM, Knopp T. Artifact free reconstruction with the system matrix approach by overscanning the field-free-point trajectory in magnetic particle imaging. *Phys Med Biol*. 2016;61(2):475-87.
26. Mohtashamdolatshahi A, Kratz H, Kosch O, Hauptmann R, Stolzenburg N, Wiekhorst F, Sack I, Hamm B, Taupitz M, Schnorr J. In vivo magnetic particle imaging: angiography of inferior vena cava and aorta in rats using newly developed multicore particles. *Sci Rep*. 2020;10(1):17247.
27. Mangarova DB, Brangsch J, Mohtashamdolatshahi A, Kosch O, Paysen H, Wiekhorst F, Klopffleisch R, Buchholz R, Karst U, Taupitz M, Schnorr J, Hamm B, Makowski MR. Ex vivo magnetic particle imaging of vascular inflammation in abdominal aortic aneurysm in a murine model. *Sci Rep*. 2020;10(1):12410.
28. Tombach B, Reimer P, Bremer C, Allkemper T, Engelhardt M, Mahler M, Ebert W, Heindel W. First-pass and equilibrium-MRA of the aortoiliac region with a superparamagnetic iron oxide blood pool MR contrast agent (SH U 555 C): results of a human pilot study. *NMR IN BIOMEDICINE*. 2004;17(7):500-6.
29. Lanz B, Poitry-Yamate C, Gruetter R. Image-derived input function from the vena cava for 18F-FDG PET studies in rats and mice. *J Nucl Med*. 2014;55(8):1380-8.
30. Vaalma S, Rahmer J, Panagiotopoulos N, Duschka RL, Borgert J, Barkhausen J, Vogt FM, Haegele J. Magnetic Particle Imaging (MPI): Experimental Quantification of Vascular Stenosis Using Stationary Stenosis Phantoms. *PLOS ONE*. 2017;12(1):e0168902.
31. Brangsch J, Reimann C, Kaufmann JO, Adams LC, Onthank DC, Thone-Reineke C, Robinson SP, Buchholz R, Karst U, Botnar RM, Hamm B, Makowski MR. Concurrent Molecular Magnetic Resonance Imaging of Inflammatory Activity and Extracellular Matrix Degradation for the Prediction of Aneurysm Rupture. *Circ Cardiovasc Imaging*. 2019;12(3):e008707.
32. Raffort J, Lareyre F, Clement M, Hassen-Khodja R, Chinetti G, Mallat Z. Monocytes and macrophages in abdominal aortic aneurysm. *Nat Rev Cardiol*. 2017;14(8):457-71.

33. Belanova AA, Gavalas N, Makarenko YM, Belousova MM, Soldatov AV, Zolotukhin PV. Physicochemical Properties of Magnetic Nanoparticles: Implications for Biomedical Applications In Vitro and In Vivo. *Oncol Res Treat.* 2018;41(3):139-43.
34. Wagner S, Schnorr J, Ludwig A, Stangl V, Ebert M, Hamm B, Taupitz M. Contrast-enhanced MR imaging of atherosclerosis using citrate-coated superparamagnetic iron oxide nanoparticles: calcifying microvesicles as imaging target for plaque characterization. *Int J Nanomedicine.* 2013;8:767-79.
35. Klibanov AL, Maruyama K, Torchilin VP, Huang L. Amphipathic polyethyleneglycols effectively prolong the circulation time of liposomes. *FEBS Lett.* 1990;268(1):235-7.
36. Arami H, Teeman E, Troksa A, Bradshaw H, Saatchi K, Tomitaka A, Gambhir SS, Häfeli UO, Liggitt D, Krishnan KM. Tomographic magnetic particle imaging of cancer targeted nanoparticles. *Nanoscale.* 2017;9(47):18723-30.
37. Orendorff R, Peck AJ, Zheng B, Shirazi SN, Matthew Ferguson R, Khandhar AP, Kemp SJ, Goodwill P, Krishnan KM, Brooks GA, Kaufer D, Conolly S. First in vivo traumatic brain injury imaging via magnetic particle imaging. *Phys Med Biol.* 2017;62(9):3501-9.
38. Knopp T, Gdaniec N, Moddel M. Magnetic particle imaging: from proof of principle to preclinical applications. *Phys Med Biol.* 2017;62(14):R124-R78.
39. Molwitz I, Ittrich H, Knopp T, Mummert T, Salamon J, Jung C, Adam G, Kaul MG. First magnetic particle imaging angiography in human-sized organs by employing a multimodal ex vivo pig kidney perfusion system. *Physiol Meas.* 2019;40(10):105002.
40. Storath M, Brandt C, Hofmann M, Knopp T, Salamon J, Weber A, Weinmann A. Edge Preserving and Noise Reducing Reconstruction for Magnetic Particle Imaging. *IEEE Transactions on Medical Imaging.* 2017;36(1):74-85.
41. Rahmer J, Gleich B, Schmidt J, Bontus C, Schmale I, Kanzenbach J, Borgert J, Woywode O, Halkola A, Weizenecker J. Continuous Focus Field Variation for Extending the Imaging Range in 3D MPI. *Magnetic Particle Imaging. Springer Proceedings in Physics: Springer, Berlin, Heidelberg; 2012. p. 255-9.*

## Statutory declaration

“I, Azadeh Mohtashamdolatshahi, by personally signing this document in lieu of an oath, hereby affirm that I prepared the submitted dissertation on the topic Magnetic Particle Imaging: New Approaches for Vascular Imaging (Magnetic Particle Imaging: Neue Ansätze für die Gefäßbildgebung), independently and without the support of third parties, and that I used no other sources and aids than those stated.

All parts which are based on the publications or presentations of other authors, either in letter or in spirit, are specified as such in accordance with the citing guidelines. The sections on methodology (in particular regarding practical work, laboratory regulations, statistical processing) and results (in particular regarding figures, charts and tables) are exclusively my responsibility.

Furthermore, I declare that I have correctly marked all of the data, the analyses, and the conclusions generated from data obtained in collaboration with other persons, and that I have correctly marked my own contribution and the contributions of other persons (cf. declaration of contribution). I have correctly marked all texts or parts of texts that were generated in collaboration with other persons.

My contributions to any publications to this dissertation correspond to those stated in the below joint declaration made together with the supervisor. All publications created within the scope of the dissertation comply with the guidelines of the ICMJE (International Committee of Medical Journal Editors; [www.icmje.org](http://www.icmje.org)) on authorship. In addition, I declare that I shall comply with the regulations of Charité – Universitätsmedizin Berlin on ensuring good scientific practice.

I declare that I have not yet submitted this dissertation in identical or similar form to another Faculty.

The significance of this statutory declaration and the consequences of a false statutory declaration under criminal law (Sections 156, 161 of the German Criminal Code) are known to me.”

Date

Signature

# Declaration of my own contribution to the publications

## **Publication A:**

Kratz H, **Mohtashamdolatshahi A**, Eberbeck D, Kosch O, Hauptmann R, Wiekhorst F, Taupitz M, Hamm B, Schnorr J. MPI Phantom Study with A High-Performing Multicore Tracer Made by Coprecipitation. *Nanomaterials (Basel)*. 2019;9(10):1466

The multicore nanoparticles were synthesized by Dr. Kratz and Dr. Hauptmann. The physiochemical characterization of nanoparticles was carried by Dr. Kratz and the magnetic characterization by Dr. Eberbeck. The idea of evaluation of the MPI performance of the nanoparticles in phantoms was raised by Dr. Kratz and Dr. Kosch and the acquisition of the phantoms were carried out with their assistance. My contributions in detail are listed below:

- Planning, organization and acquisition of MPI images with consultation of supervisors.
- Conceptualization for image reconstruction optimization and image analysis methodology.
- Performing the image post-processing, investigations on image reconstructions and evaluation of quantitative MPI data.
- Interpretation of the results, visualization of MPI figures and relevant MPI graphs.
- Substantial contribution to first draft and reviewing of the final version of the paper.

The results and conclusions I obtained were approved primarily by Dr. Kosch, Dr. Kratz, Dr. Wiekhorst and further on by other members/supervisors. This includes the figures 6 – 12 in the publication.

## **Publication B:**

**Mohtashamdolatshahi A**, Kratz H, Kosch O, Hauptmann R, Stolzenburg N, Wiekhorst F, Sack I, Hamm B, Taupitz M, Schnorr J. In vivo magnetic particle imaging: angiography of inferior vena cava and aorta in rats using newly developed multicore particles. *Sci Rep*. 2020;10(1):17247

The synthesis of multicore nanoparticles was carried out by Dr. Kratz. The in vivo experiments were conducted by Dr. Schnorr, Dr. Stolzenburg and Dr. Kratz. The MPI acquisition was carried out by Dr. Kosch. My contributions in detail are listed below:

- Conceptualization of the image post-processing and analysis strategy of dynamic MPI data from image reconstruction to evaluation of quantitative MPI data.
- Interpretation of the results, creation and visualization of data.
- Co-conceptualization and writing of original draft.

The results and conclusions I obtained were approved primarily by Dr. Kosch, Dr. Kratz, Dr. Wiekhorst, Dr. Schnorr and further on by other members/supervisors. All figures and the table were created by me expect for one: the MPI spectrum of MNP presented in the supplementary data (measured by Dr. Olaf Kosch).

### **Publication C:**

Mangarova DB, Brangsch J, **Mohtashamdolatshahi A**, Kosch O, Paysen H, Wiekhorst F, Klopffleisch R, Buchholz R, Karst U, Taupitz M, Schnorr J, Hamm B, Makowski MR. Ex vivo magnetic particle imaging of vascular inflammation in abdominal aortic aneurysm in a murine model. Sci Rep. 2020;10(1):12410

The conceptualization of the study, the animal model development, in vivo experiments and histology were carried out by the working group of Prof. Makowski, Ms. Mangarova and Ms. Brangsch. The magnetic particle spectroscopy measurements (MPS) were performed by Dr. Paysen. The LA-ICP-MS experiments were conducted by Dr. Karst and Ms. Buchholz. My contributions in detail are listed below:

- Co-conceptualization of acquisition, reconstruction and visualization of ex vivo MPI images.
- Planning, organization, acquisition and visualization of ex vivo MPI images.
- Contributing to first draft and reviewing of the final version of the paper.

The results and conclusions I obtained were approved primarily by Dr. Kosch and Mr. Paysen. and further on by other members/supervisors. These results I obtained are shown in figure 4. (A3) and the MPI determined iron amount (my work) is plotted vs. MPS determined iron amount.

---

Signature of the first supervisor

---

Signature of the student

# Publication A: MPI Phantom Study with A High-Performing Multicore Tracer Made by Coprecipitation

Journal Data Filtered By: **Selected JCR Year: 2018** Selected Editions: SCIE,SSCI  
 Selected Categories: **“MATERIALS SCIENCE, MULTIDISCIPLINARY”**  
 Selected Category Scheme: WoS  
**Gesamtanzahl: 293 Journale**

Rank	Full Journal Title	Total Cites	Journal Impact Factor	Eigenfactor Score
66	CRYSTAL GROWTH & DESIGN	29,940	4.153	0.037860
67	JOURNAL OF THE MECHANICS AND PHYSICS OF SOLIDS	18,866	4.087	0.019250
68	MATERIALS SCIENCE AND ENGINEERING A-STRUCTURAL MATERIALS PROPERTIES MICROSTRUCTURE AND PROCESSING	79,492	4.081	0.065810
69	Extreme Mechanics Letters	1,439	4.075	0.005890
70	CONSTRUCTION AND BUILDING MATERIALS	56,987	4.046	0.063710
71	Nanomaterials	4,955	4.034	0.008390
72	Liquid Crystals Reviews	176	3.917	0.000810
73	APPLIED CLAY SCIENCE	15,784	3.890	0.014850
74	PHYSICAL REVIEW B	371,919	3.736	0.363380
75	Physica Status Solidi-Rapid Research Letters	3,346	3.729	0.008100
76	LANGMUIR	117,927	3.683	0.096010
77	INTERNATIONAL JOURNAL OF FATIGUE	13,715	3.673	0.014320
78	SCIENCE AND TECHNOLOGY OF ADVANCED MATERIALS	5,047	3.585	0.005870
79	Smart Materials and Structures	19,870	3.543	0.025150
80	Materials Science and Engineering B-Advanced Functional Solid-State Materials	10,565	3.507	0.005690
81	ORGANIC ELECTRONICS	12,429	3.495	0.018640
82	JOURNAL OF MATERIALS SCIENCE	50,817	3.442	0.034620
83	NANOTECHNOLOGY	43,992	3.399	0.048160
83	Soft Matter	36,016	3.399	0.066600
85	IEEE Journal of Photovoltaics	4,887	3.398	0.011360

Article

# MPI Phantom Study with A High-Performing Multicore Tracer Made by Coprecipitation

Harald Kratz <sup>1,\*</sup>, Azadeh Mohtashamdolatshahi <sup>1</sup>, Dietmar Eberbeck <sup>2</sup>, Olaf Kosch <sup>2</sup>, Ralf Hauptmann <sup>1</sup>, Frank Wiekhorst <sup>2</sup>, Matthias Taupitz <sup>1</sup>, Bernd Hamm <sup>1</sup> and Jörg Schnorr <sup>1</sup>

<sup>1</sup> Charité-Universitätsmedizin Berlin, corporate member of Freie Universität Berlin, Humboldt-Universität zu Berlin, and Berlin Institute of Health, Department of Radiology, D-10117 Berlin, Germany; Azadeh.Mohtashamdolatshahi@charite.de (A.M.); Ralf.Hauptmann@charite.de (R.H.); Matthias.Taupitz@charite.de (M.T.); Bernd.Hamm@charite.de (B.H.); Joerg.Schnorr@charite.de (J.S.)

<sup>2</sup> Physikalisch-Technische Bundesanstalt, D-10587 Berlin, Germany; Dietmar.Eberbeck@ptb.de (D.E.); Olaf.Kosch@ptb.de (O.K.); Frank.Wiekhorst@ptb.de (F.W.)

\* Correspondence: Harald.Kratz@charite.de; Tel.: +49-30-450-527180

Received: 11 September 2019; Accepted: 14 October 2019; Published: 16 October 2019



**Abstract:** Magnetic particle imaging (MPI) is a new imaging technique that detects the spatial distribution of magnetic nanoparticles (MNP) with the option of high temporal resolution. MPI relies on particular MNP as tracers with tailored characteristics for improvement of sensitivity and image resolution. For this reason, we developed optimized multicore particles (MCP 3) made by coprecipitation via synthesis of green rust and subsequent oxidation to iron oxide cores consisting of a magnetite/maghemite mixed phase. MCP 3 shows high saturation magnetization close to that of bulk maghemite and provides excellent magnetic particle spectroscopy properties which are superior to Resovist<sup>®</sup> and any other up to now published MPI tracers made by coprecipitation. To evaluate the MPI characteristics of MCP 3 two kinds of tube phantoms were prepared and investigated to assess sensitivity, spatial resolution, artifact severity, and selectivity. Resovist<sup>®</sup> was used as standard of comparison. For image reconstruction, the regularization factor was optimized, and the resulting images were investigated in terms of quantifying of volumes and iron content. Our results demonstrate the superiority of MCP 3 over Resovist<sup>®</sup> for all investigated MPI characteristics and suggest that MCP 3 is promising for future experimental in vivo studies.

**Keywords:** magnetic particle imaging (MPI); magnetic particle spectroscopy (MPS); magnetic nanoparticles (MNP); magnetic multicore particles (MCP); coprecipitation

## 1. Introduction

Magnetic particle imaging (MPI) was first presented as a novel radiation-free imaging modality by Weizenecker and Gleich in 2005 [1]. MPI is capable of 4D imaging with high temporal resolution (46 volumes per second) and a spatial resolution of 1–2 mm depending on the scanner type and the tracer used. MPI directly and specifically measures the magnetic moments of magnetic nanoparticles (MNP) using an alternating magnetic field. Its high sensitivity and high temporal resolution with the option of quantifying the administered MNP as tracers make MPI a promising method, especially for imaging the cardiovascular system and local perfusion, if the tracer behaves as a blood pool agent [2,3]. The MNP have nonlinear magnetization behavior, generating higher harmonics of the applied excitation frequency which are measured inductively. Additional magnetic field gradients are used to facilitate spatial encoding in the field of view (FOV) [4]. For more detailed information on principles of MPI one can refer to [1]. As MPI only detects the tracer, combination of MPI with other imaging modalities such as magnetic resonance imaging (MRI) or computed tomography (CT) is

necessary to obtain the corresponding anatomical information [5,6]. Both, MPI scanners and tracers are still under development. Regarding tracers, Resovist<sup>®</sup> is still a kind of standard for MPI, since most published studies of MPI, especially those obtained by in vivo experiments, have been conducted with this tracer [2,7–17]. Since Resovist<sup>®</sup> was initially developed as a contrast agent for MRI of the liver it has some disadvantages when used for MPI. For MPI investigations of the cardiovascular system the in vivo blood circulation time of Resovist<sup>®</sup> is limited, and MPI signal intensity is also generally restricted [16]. Several other MNP with promising properties as MPI tracers have been described in the literature [16,18–20], but most of these MNP are currently not generally available for MPI studies. Furthermore, some potential MPI tracers with superior magnetic particle spectroscopy (MPS) signal intensities compared with Resovist<sup>®</sup> are commercially available (perimag<sup>®</sup> [21,22], synomag-D<sup>®</sup> [23], micromod Partikeltechnologie GmbH, Rostock, Germany). Nevertheless, to further advance MPI as a medical imaging modality, there is still a great need for the development of new MPI tracers. Tracers with excellent MPI characteristics are especially crucial for the potential preclinical development of this imaging modality and the identification of new possible clinical applications. The most important methods for synthesizing new MNP are coprecipitation and thermal decomposition [5,24,25]. Both methods have their strengths and weaknesses. Thermal decomposition provides very good control over the MNP shape, and the achievable size distribution is very narrow. However, this method is complicated and needs high temperatures in some cases over 300 °C plus an inert gas atmosphere and produces a lot of possibly toxic byproducts [26]. Moreover, with this method, the MNP are synthesized in organic solvents and, for use in biological systems, need to be transferred into the aqueous phase.

In contrast, coprecipitation is a very simple method that needs ambient conditions with a temperature of up to approx. 95 °C but often lacks good control over shape, and the realizable size distribution is only relatively narrow [24,27]. Apart from MPI tracers consisting of single-core particles, there are also some which are based on so-called multicore particles (MCP), which theoretically might have some advantages and are also partly contained in Resovist<sup>®</sup> [28]. In theory, the ideal MPI tracer should have a magnetic core diameter of approx. 25 nm for a 25-kHz excitation field frequency and be monodisperse [29]. In addition, for in vivo use MPI tracers have to be biocompatible and biodegradable [5]. We already reported the synthesis of MCP [26], which is a new generation of MPI tracers with very good MPI tracer properties. In the first in vivo studies in rats biocompatibility of MCP was investigated with doses up to 3 mmol Fe/kg of body weight and no adverse side effects could be observed. In addition, MCP showed a fast MRI degradation in liver with a half-life of seven days [26]. Compared to the commercially available potential MPI tracers from micromod Partikeltechnologie GmbH our MCP have a different coating and magnetic core structure. Here we present the synthesis and physicochemical characterization of a further improved version of these MCP made by coprecipitation and investigations on their MPI signal generating properties in phantom experiments performed using a preclinical MPI scanner. We examined the new tracer focusing on the achievable sensitivity, spatial resolution, and occurrence and severity of artifacts using Resovist<sup>®</sup> as standard of reference. In addition, we assessed tracer selectivity concerning the discrimination of small tracer volumes in close vicinity to each other, in particular with a view to future in vivo experiments and further advancement of MCP.

## 2. Materials and Methods

### 2.1. Chemicals

Acrylamide solution (30% in water), N-N'-methylenebisacrylamide solution (2% in water), ammonium persulfate (1% in water), and N,N,N',N'-tetramethylethylenediamine (≥98%, p.a.) were purchased from Carl Roth GmbH (Karlsruhe, Germany). All other chemicals were purchased from Sigma-Aldrich (Steinheim, Germany). Iron(II) chloride tetrahydrate and carboxymethyl dextran sodium salt were used as received without further purification. To prepare a 5% hydrogen peroxide solution (5 wt% in H<sub>2</sub>O<sub>2</sub>), hydrogen peroxide solution (30 wt% in H<sub>2</sub>O<sub>2</sub>) was diluted with five parts

of deionized water. Deionized water was generally produced using a Mill-Q A10 system (Millipore, Billerica, MA, USA) and used for both synthesis and for preparation of solutions and dispersions.

## 2.2. Magnetic Particle Imaging (MPI) Tracers

Resovist<sup>®</sup> was purchased from Fujifilm RI Pharma Co., Tokyo, Japan. Optimized multicore particles (MCP 3) were synthesized in our laboratory at Charité using a technique of alkaline coprecipitation of ferrous chloride in the presence of atmospheric oxygen and subsequent oxidation by hydrogen peroxide [26]. Thereafter, the washed MNP were coated with carboxymethyl dextran sodium salt (CMD, 10–20 kD) and heated for several hours. After washing with Milli-Q water by ultrafiltration using Vivaflow 200 filters with a 100 kDa regenerated cellulose (RC) membrane (Sartorius AG, Göttingen, Germany), the resulting MNP were divided into different fractions by repeated magnetic separation (see supplement text S1 for further details). For later use, MCP were concentrated to 145.5 mmol Fe/l by centrifugation at  $3112 \times g$  using Amicon Ultra-15 Centrifugal Filter Units (PLHK Ultracel-PL Membrane, 100 kDa). Thereafter the dispersion was passed through 0.2  $\mu\text{m}$  cellulose mixed ester (CME) syringe filters for sterile filtration. MNP dispersions were diluted with Milli-Q water to prepare the respective final concentrations required for the experiments and MNP characterization (see below).

## 2.3. Magnetic Nanoparticles (MNP) Characterization

Hydrodynamic diameters of MNP were determined by dynamic light scattering (DLS) on a Zetasizer Nano ZS particle analyzer (Malvern Instruments, Worcestershire, UK). For DLS measurement, MNP dispersions were diluted with Milli-Q water to a final concentration of 1 mmol Fe/l. For  $\zeta$ -potential measurement, MNP dispersions were diluted with 10 mM NaCl to a final concentration of 1 mmol Fe/l and adjusted to a pH of 7.19 with NaOH. MNP size and morphology were analyzed by transmission electron microscopy (TEM) using a TECNAI G2 20 S-Twin (FEI-Company, Hillsboro, OR, USA). Average core/multicore diameters ( $d_v$ ) and size distributions were calculated for each nanoparticle sample by averaging 200 MCP from the TEM images using ImageJ software (developed by the National Institutes of Health, Bethesda, Maryland, USA). The ferric and ferrous iron contents of the MNP dispersions were colorimetrically determined using the phenanthroline method [30]. MNP were also analyzed by magnetic particle spectroscopy (MPS) to assess the response of MNP to alternating magnetic fields. MPS measurements were performed using a magnetic particle spectrometer (MPS-3, Bruker BioSpin, Ettlingen, Germany) at 10 mT, 25 kHz, and 37 °C for 10 s. Deviating from that, samples embedded in polyacrylamide (PAA) gel were measured at  $27.5 \pm 1.5$  °C.

For measurements, 30  $\mu\text{L}$  of each sample was filled in Life Technologies polymerase chain reaction (PCR) tubes. The amplitude of the magnetic moment was normalized to the iron content of each sample, resulting in the spectrum of the magnetization,  $M_k$ , which is given in  $\text{Am}^2/\text{mol}(\text{Fe})$ . For  $M(H)$  measurements, 75  $\mu\text{L}$  sample volumes were filled in polycarbonate capsules. The magnetic moment of each sample was measured using an MPMS (Magnetic Property Measurement System, Quantum Design, USA) successively increasing the applied magnetic field from 0 to 5 T. The background signal caused by empty capsules, diamagnetic susceptibility of the dispersion medium, and deionized water was subtracted from the signal obtained for the samples. The resulting signal represents the magnetization of the MNP and was normalized to the iron content of the sample for quantitative evaluation. For partial immobilization of MCP 3 in PAA gel, 52  $\mu\text{L}$  acrylamide solution (30% in water), 52  $\mu\text{L}$  N-N'-methylenebisacrylamide solution (2% in water), 10  $\mu\text{L}$  ammonium persulfate (1% in water), 273  $\mu\text{L}$  water, 3  $\mu\text{L}$  MCP 3 dispersion (145.5 mmol (Fe)/l), and 9.7  $\mu\text{L}$  N,N,N',N'-tetramethylethylenediamine (1:30 diluted with water (v/v)) were mixed and subsequently vortexed. Then 50  $\mu\text{L}$  of the resulting dispersion was filled in a measuring cuvette and polymerized at 60 °C in a water bath for approx. 30 min.

#### 2.4. MPI Phantom Studies

The phantoms used in this study were manufactured from PVC tubes with 0.5 mm wall thickness and inner diameters of 1, 2, and 3 mm (Conrad Electronic, Hirschau, Germany). All tubes were cut to a final length of 20 mm. The tubes were filled with tracer dispersions and the open ends sealed with paraffin embedding wax (Paraplast, Tissue Embedding Medium, Sigma, St Louis, MO, USA). For the dual-tube phantoms, pairs of tubes with the same or different inner diameters were longitudinally fixed to each other using Parafilm M<sup>®</sup> (Bemis Company, Neenah, WI, USA). Single-tube phantoms of the dilution series were filled with 90  $\mu$ L tracer dispersion with the following concentrations: 10, 5, 2, 1, 0.5, 0.2, and 0.1 mmol Fe/l. For the dual-tube phantom series, six different pairwise combinations of tubes were filled with MCP 3 or Resovist<sup>®</sup> with in each case a concentration of 10 mmol Fe/l. In the third phantom series, tubes with the same inner diameters (1, 2, and 3 mm) were longitudinally fixed to each other and filled with 1 mmol Fe/l MCP 3 or Resovist<sup>®</sup>.

The volumes of tracer dispersions were 90  $\mu$ L for the PVC tubes with 3 mm inner diameter, 40  $\mu$ L for the tubes with 2 mm inner diameter, and 10  $\mu$ L for the tubes with 1 mm inner diameter. MPI phantom experiments were performed on a preclinical MPI scanner (Bruker 25/20 FF, Bruker Biospin GmbH, Ettlingen, Germany). The scanner operates according to the field-free-point (FFP) principle and needs a prerecorded system function (SF) for reconstruction of images. The standard 25/20 MPI system has dual-purpose coils to simultaneously generate the drive-field (DF) for excitation of the MNP dispersion and to receive the voltage signals from the MNP induced by magnetization. In addition, a prototype of a separate receive coil (developed by Bruker and Physikalisch-Technische Bundesanstalt (PTB)) was installed in the x-channel of the MPI system at Charité to improve the signal-to-noise ratio (SNR) and sensitivity [31,32]. In the MPI measurement, we applied a DF amplitude of 12 mT with approx. 25 kHz in all three directions and a selection field gradient of  $(G_x/G_y/G_z) = (1.25/1.25/2.5)$  T/m. The phantoms were measured in two different orientations to take the different gradient resolutions of x, y, and z direction into account.

#### 2.5. Image Reconstruction and Analysis

##### 2.5.1. Reconstruction

Prior to reconstruction, the background signal was subtracted from the measured signal. To this end, the background signal was measured before the phantom measurement for the same length of time as required for the actual measurement [33]. The acquired data were reconstructed to  $33 \times 33 \times 33$  voxels using an iterative Kaczmarz algorithm [34] with five iteration steps (ParaVision 6, Bruker Biospin GmbH, Ettlingen, Germany). The voxel size of the applied SF was  $0.8 \times 0.8 \times 0.4$  mm<sup>3</sup>. For reconstruction, the frequency range above the SNR threshold, determined from the SF, was employed. For elimination of background noise, the bandwidth was limited to 0.09–125 MHz [33]. For both, MCP 3 and Resovist<sup>®</sup>, 2438 frequencies were chosen according to the SNR of the applied system function (SF), while different SNR thresholds of 24 and 6 were selected for MCP 3 and Resovist<sup>®</sup>, respectively. For SF parameters please see supplement text S6. The maximum order of mixing frequencies was 25 for all images. A block average of 5 was applied to each measurement in the reconstruction step to reduce image noise. In reconstruction of the phantom measurements, the determined SNR-optimized regularization factors  $\lambda$  between  $10^{-2}$  and  $10^{-1}$  were used for MCP 3 and Resovist<sup>®</sup>. In the final reconstruction of the phantoms,  $\lambda = 10^{-2}$  was used for higher concentrations, i.e., 10 and 5 mmol Fe/l, and  $\lambda = 10^{-1}$  for lower concentrations because these values were observed to be the optimal compromise for the two tracers.

##### 2.5.2. Evaluation of SNR-Optimized Regularization Factor (Plotting SNR Against $\lambda$ )

SNR of different tracer concentrations in the dilution series was analyzed using MATLAB (Mathworks, Natick, MA, USA) in relation to different regularization factors ( $\lambda$ ), ranging from  $10^0$  to  $10^{-6}$  [16]. To this end, images of the single-tube phantoms were reconstructed with 5 iterations.

To determine the SNR, first, a 30% cut-off threshold from maximum was applied to the reconstructed 3D image to eliminate most background noise and artifacts. Images were then segmented in 3D space via a stack of 2D masks created by active contours with 100 iterations [35]. SNR was defined as the mean signal level of the segmented object over the mean signal level of the background.

### 2.5.3. Methods for Volume and Iron Evaluation in The Single-Tube Phantom Series

The total phantom volume of the single-tube phantoms visualized in the images and their iron content were calculated using MATLAB (Mathworks, Natick, MA, USA). In detail, the total volume was determined as the number of voxels in the segmented area multiplied by the voxel volume and the iron amount by the integration of iron content within the segmented area. The volumes and iron contents calculated from the images were compared with the known values of the single-tube phantoms, and arithmetic means were calculated.

## 3. Results and Discussion

### 3.1. MCP 3 Synthesis

MCP 3 were synthesized according to our synthesis described previously [26]. In brief, we used a modified technique of alkaline coprecipitation of ferrous chloride with subsequent oxidation and annealing. The resulting MCP were coated with CMD for electrosteric stabilization of the MNP. We chose the coprecipitation method for developing these MNP because it is efficient and relatively mild in terms of reaction conditions. Contrast agents based on iron oxide nanoparticles and formerly used for clinical MRI of the liver (Resovist<sup>®</sup> [36,37] and Endorem<sup>®</sup> [37]) were developed using the coprecipitation method.

For the present study, we optimized our initial synthesis method in terms of MPS/MPI performance by different modifications such as enlarging the approach with an upscaling factor of three and an altered magnetic separation procedure. These modifications led to better control over the magnetic core diameters and their size distribution (for details, please see supplement text S1).

### 3.2. MNP Characterization

TEM for assessment of the core structure of MCP 3 revealed that cores of MCP 3 were not uniform (Figure 1a–c), consisting of a predominantly (about 60%) clustered structure and a smaller share (about 40%) of other MNP with an unknown structure (see supplement Figure S2) [26]. The selected area electron diffraction (SAED) pattern indicates that the MNP consist of magnetite and/or maghemite (Figure 1d). The photometrically measured Fe<sup>2+</sup> content was 3.9%, which strongly suggests a high maghemite content of MCP 3. For evidence of the exact iron oxide composition, for example, x-ray diffraction or Mössbauer spectroscopy investigations would be necessary [38,39].

The hydrodynamic size of the MNP was measured by DLS. This method demonstrated the absence of aggregates, which is a very important parameter for dispersion stability and in vivo use [5]. Furthermore, the MNP dispersions can be stored for more than a year and remain stable. Figure 2 shows the hydrodynamic volume-weighted size distribution of the MNP as measured by DLS (Figure 2a) and the number-weighted size distribution determined by TEM (Figure 2b). The distribution parameters are compiled in Table 1. MNP had a mean core diameter of  $32 \pm 8$  nm in TEM. The hydrodynamic diameter range (by volume) of the tracers measured by DLS was 24.4–122.4 nm, with a z-average of 54 nm and a polydispersity index (PDI) of 0.08.

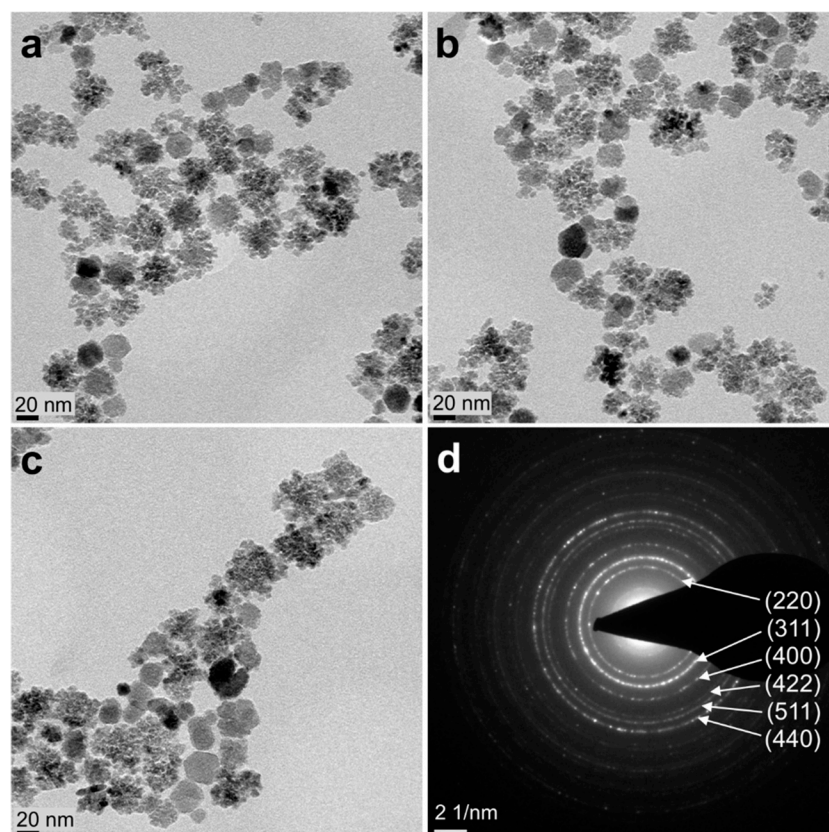


**Figure 1.** (a–c) TEM images of multicore particles (MCP 3) (scale bar: 20 nm) and (d) corresponding selected area electron diffraction (SAED) pattern (scale bar:  $2 \text{ nm}^{-1}$ ) For magnified TEM images of MCP 3, please see supplement Figures S2–S4.

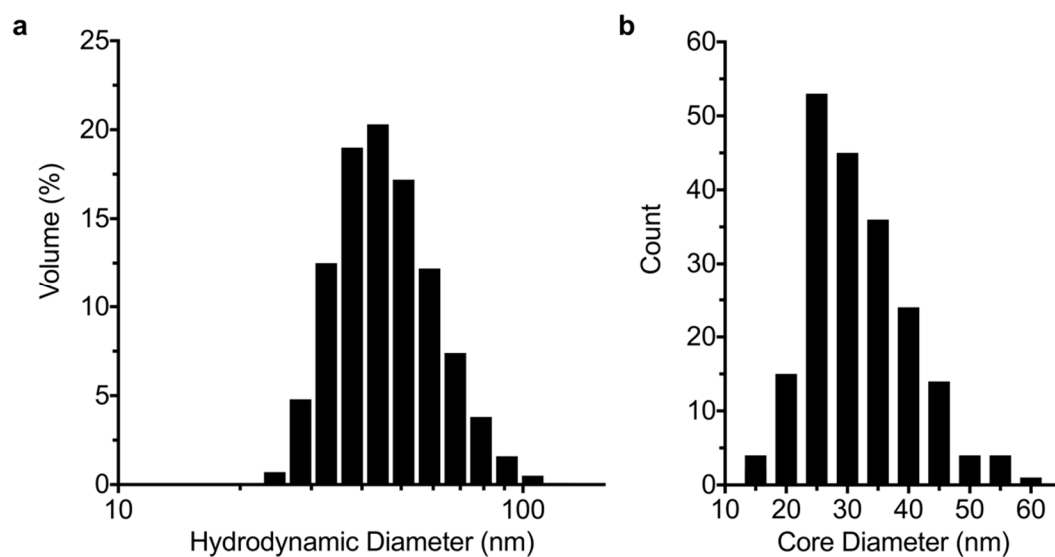


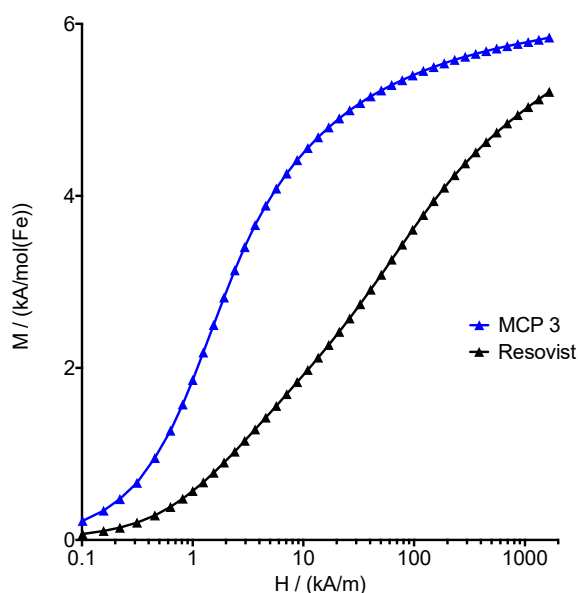
**Figure 2.** (a) Hydrodynamic and (b) TEM core diameter distributions of MCP 3. The hydrodynamic size distribution is given by volume. The TEM size distribution is based on the measurement of 200 multicore particles of MCP 3. The y-axis of the histogram in b gives the number of magnetic nanoparticles (MNP).

**Table 1.** Compilation of characteristics of MCP 3 as determined by TEM and DLS.

Mean Core Diameter (TEM) * [nm]	$d_V$ (DLS) [nm] by Volume	Z-Average (DLS) [nm]	PDI (DLS)	$\zeta$ -Potential [mV]
$31.72 \pm 8.4$	24.4–122.4	53.94	0.08	−33.5

\*: 200 MCP counted.

The  $M(H)$  curve derived from the measurements revealed a saturation magnetization  $M_S$  for MCP 3 of  $5.8 \pm 0.3 \text{ Am}^2/\text{mol}(\text{Fe})$  ( $104 \pm 4 \text{ Am}^2/\text{kg}(\text{Fe})$ ) (Figure 3), which is close to  $M_S$  bulk values of  $6.2 \text{ Am}^2/\text{mol}(\text{Fe})$  ( $111 \text{ Am}^2/\text{kg}(\text{Fe})$ ) for maghemite reported in the literature [26]. This fits well with the low photometrically measured  $\text{Fe}^{2+}$  content of 3.9% and the presumed high maghemite content of the magnetic cores. It should be noted here that the saturation magnetization of magnetite/maghemite nanoparticles is usually below pure bulk values [40–45], which is attributable to surface effects and/or a high amount of crystallographic disorder [26]. For comparison, the  $M_S$  of pure Magnetite is reported to be  $7.1 \text{ Am}^2/\text{mol}(\text{Fe})$  ( $127 \text{ Am}^2/\text{kg}(\text{Fe})$ ), and the  $\text{Fe}^{2+}$  content should theoretically be 33.3% [46].

**Figure 3.** Molar magnetization  $M$  as a function of applied external field  $H$  measured for MCP 3 and Resovist<sup>®</sup> at 295 K.

MPS inductively measures the nonlinear response of the MNP to an alternating magnetic field [47]. In an MPS, the measured intensities of the harmonics of the basic frequency are a measure of the potential properties in an MPI scanner. MPS can be regarded as a zero-dimensional MPI scanner without spatial resolution [47]. Therefore, MPS is a very important tool for the fast screening of different MNP probes with regard to their MPI properties in MPI tracer development. MPS measurements showed markedly stronger signal amplitudes for MCP 3 compared to Resovist<sup>®</sup> as the standard of reference. The signal magnitude of MCP 3 is amplified by a factor of approx. five in the relevant range of up to 800 kHz (Figure 4). In vivo, the largest proportion of MNP is assumed to be first opsonized and then phagocytosed by macrophages especially in the liver and spleen [48]. In this case, the MNP would subsequently be taken up into lysosomes and appear wholly or partially immobilized within the MPS measurement time of 40  $\mu\text{s}$ . For the first assessment of the MPS properties of MCP 3 under these conditions, we embedded the MNP in a PAA gel (4.2%) [49]. In the relevant range, the MPS signal of this gel was slightly lower in amplitude but still three to four times higher than in the Resovist<sup>®</sup> dispersion, i.e., immobilization reduced the signal amplitude by about 20% at the 3rd harmonic.

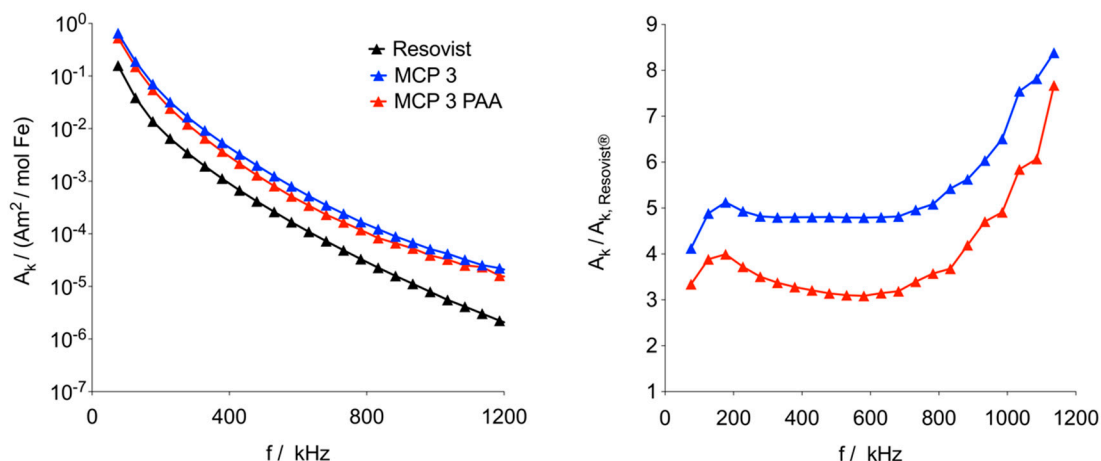


**Figure 4.** Left: magnetic particle spectroscopy (MPS) data of MCP 3 in aqueous dispersion (blue) and polyacrylamide (PAA) gel (red) in comparison with Resovist<sup>®</sup> (black) at 10 mT and 25 kHz. Data are plotted as magnetic moment (normalized to iron content) versus frequency. Right: The ratio of amplitudes of MCP 3 and Resovist<sup>®</sup> in aqueous dispersion (blue) and in the PAA gel matrix (red). In both cases, only odd harmonics are shown, and lines were added to guide the eye.

The signal drop of the harmonics in PAA gel may be attributable to a reduction of Brownian relaxation of MCP 3 [48,50] and/or to dipole-dipole interactions between the magnetic moments of the MNP [49,51]. The  $M(H)$  curve was analyzed using a model that describes magnetization by the superposition of non-interacting MNP of different sizes [28]. We applied a bimodal lognormal distribution of the magnetic moments, which was previously shown to be useful for the analysis of data obtained with Resovist<sup>®</sup> [28]. The distribution of effective magnetic diameters was derived from the distribution of magnetic moments assuming a spherical shape of the MNP and an identical saturation magnetization for all MNP. The resulting bimodal volume-weighted distribution of the effective diameters is shown in Figure 5. The first mode, A, consists of magnetic domains with a mean diameter of about 10 nm, which do not significantly contribute to the MPS or MPI signal. We, therefore, focused on the second mode, B, whose parameters are listed in Table 2.

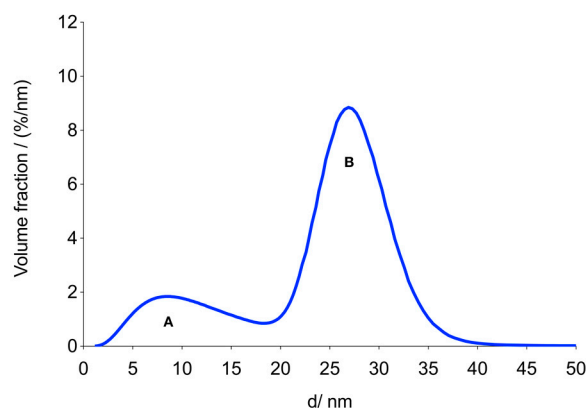


**Figure 5.** Bimodal volume distribution of MCP 3 with modes A and B calculated from the  $M(H)$  data. It is probable that only mode B contributes significantly to the MPS/MPI signal.

**Table 2.** Fit parameters obtained from the analysis of the M(H) data.

Sample	$\beta$	$d_{v2}$ (nm)	$\sigma_2$	$M_s$ Am <sup>2</sup> /kg Fe	$\mu_2$ (aAm <sup>2</sup> )	$\beta \cdot \mu_2$ (aAm <sup>2</sup> )	$M_3$ Am <sup>2</sup> /mol(Fe)
MCP 3	$0.73 \pm 0.02$	$27 \pm 0.5$	$0.13 \pm 0.01$	$5.81 \pm 0.25$	$3.9 \pm 0.2$	$2.81 \pm 0.16$	0.65
$\beta$	Volume fraction of the second mode (B) of the assumed bimodal size distribution obtained from M(H) data						
$d_{v2}$	Mean volume diameter of the second mode (B) of the assumed bimodal size distribution obtained from M(H) data						
$\sigma_2$	Geometric dispersion parameter of the second mode (B) of the assumed bimodal size distribution obtained from M(H) data						
$M_s$	Saturation magnetization of the second mode (B) of the assumed bimodal size distribution obtained from M(H) data						
$\mu_2$	Mean magnetic moment of the second mode (B) of the assumed bimodal size distribution obtained from M(H) data						
$M_3$	Third harmonic of measured MPS data (f = 25 kHz, B = 10 mT)						

It is noteworthy that the mean volume diameter,  $d_{v2}$ , of the second mode, B, is 16% smaller than the mean diameter of MCP 3 measured by TEM. The corresponding mean volumes differ by 47%. This can be explained by a particular multi-domain core structure of MCP [26]. In contrast to the structure of single-core MNP, the structure of MCP is characterized by vacancies between individual grains, making the overall physical volume greater than the magnetic one. Furthermore, the magnetization of different grains or elementary cores within the MCP may not be aligned in parallel. This also reduces the magnetic moment of the MCP. The magnetic mean volume diameter of mode B is close to the predicted optimal diameter of 25 nm for a 25 kHz excitation field frequency [29], and this part B accounts for a high fraction of 73% of the total volume. The saturation magnetization of MCP 3 is very close to that of bulk maghemite [26]. These observations could explain the high MPS/MPI signal intensity of MCP 3.

### 3.3. MPI Phantom Measurements/Image Reconstruction

Sensitivity, selectivity, and spatial resolution, which can be achieved with MCP 3 as tracer were evaluated using PVC tube phantoms with 1, 2, and 3 mm inner diameters, 0.5 mm wall thickness, and 20 mm length. As a reference for comparison, phantoms filled with Resovist<sup>®</sup> were used. First, we imaged single-tube phantoms to determine the SNR and spatial resolution of the two MPI tracers. Sensitivity, spatial resolution, and especially selectivity were assessed in dual-tube phantoms (Figure 6).

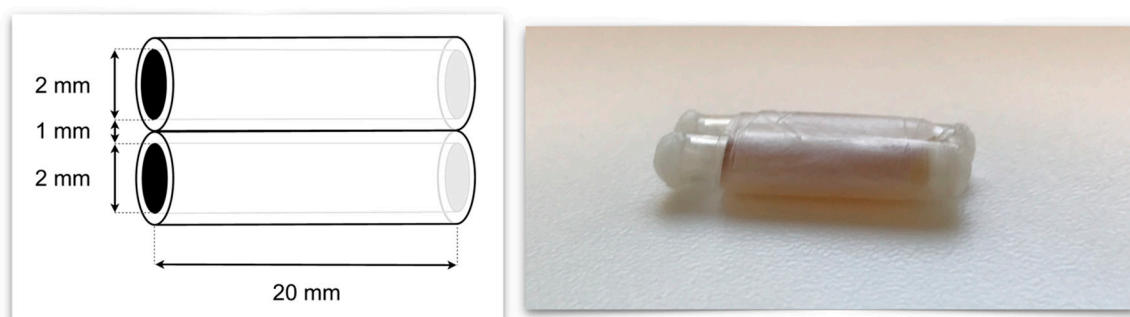


**Figure 6.** Left: Schematic drawing of a dual-tube phantom with 20 mm length and 2 mm inner diameter. Right: Photograph of a phantom with a 3 mm inner diameter filled with 10 mmol Fe/l tracer dispersion.

### 3.3.1. Phantom Dilution Series

The dilution series was investigated in a range of 0.1 to 10 mmol Fe/l, which is relevant for in vivo experiments. In general, reconstruction parameters should be optimized to achieve good spatial resolution while minimizing visual noise. Image reconstruction in MPI is an ill-posed inverse problem and hence regularization is required. Regularization parameter should be optimized to achieve a good balance between image resolution and SNR [52]. A higher regularization factor reduces artifacts while at the same time leading to a loss of object geometry, and it has been shown that variations in regularization can contribute to over- or underestimation of the size of a depicted object [53]. Accordingly, standardization of results is important for comparison. For optimal reconstruction of the tube phantoms, the regularization factor  $\lambda$  had to be identified that provides the best SNR for the respective tracer concentration. For this purpose, the MPI measurement data of the single-tube phantoms measured with their long axis in x-direction (x orientation) were reconstructed with different regularization factors  $\lambda$  for each measured tracer concentration, and then SNR was plotted over  $\lambda$  to identify the best  $\lambda$  for reconstruction with the highest SNR [16] (Figure 7).

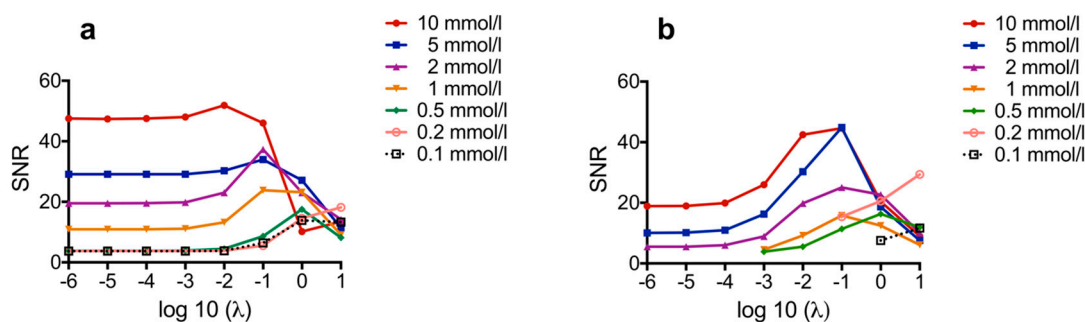


**Figure 7.** Signal-to-noise ratio (SNR) plotted over  $\lambda$  for MCP 3 (a) and Resovist<sup>®</sup> (b). For reconstruction of the tube phantoms, the  $\lambda$ -values with the highest corresponding SNR for each tracer concentration were used, which were in the range of  $10^{-1}$  to  $10^{-2}$ .

The results show that both tracers have the highest SNR in the range of  $\lambda = 10^{-1}$  to  $10^{-2}$ , especially at lower concentrations ( $<2$  mmol Fe/l), which might be relevant for, in vivo studies, the achievable SNR of MCP 3 is much higher than that of Resovist<sup>®</sup>. At higher concentrations ( $> 2$  mmol Fe/l), the SNR of MCP 3 is rather constant at  $\lambda$ -values below  $10^{-1}$ . Overall, the SNR-values of all measured MCP 3 concentrations are nearly constant at  $\lambda$ -values below  $10^{-3}$  and the SNR is more than two times higher. Conversely, the SNR values of Resovist<sup>®</sup> strongly depend on the applied  $\lambda$ . The SNR-values of Resovist<sup>®</sup> concentrations below 2 mmol Fe/l were only determinable in the  $\lambda$ -range of 10 to  $10^{-3}$  for concentrations of 1 and 0.2 mmol Fe/l and of 1 to 10 for 0.1 mmol Fe/l. In the final reconstruction of the phantom images,  $\lambda = 10^{-2}$  was used for higher concentrations, e.g., 10 or 5 mmol Fe/l, and  $\lambda = 10^{-1}$  for lower concentrations. The reconstructed interpolated images of the phantoms of the dilution series show good reproduction of the phantoms from 10 mmol Fe/l down to 2 mmol Fe/l (Figure 8, for images of phantoms filled with 2 and 5 mmol Fe/l, please see supplement Figure S7). The phantoms were measured in two orientations, with their long axis in x- and z-direction, to take the different gradients of the selection field into account. In the range from 1 to 0.1 mmol Fe/l, the changes in phantom shapes become increasingly distorted along with an increase in artifact and noise levels. In x-axis orientation the phantoms filled with MCP 3 are reasonably well displayed down to concentrations of 0.1 mmol Fe/l. Overall, visualization was better for MCP 3-filled phantoms compared with phantoms filled with Resovist<sup>®</sup>, which produced only noise and artifacts especially at the lowest concentration of 0.1 mmol Fe/l. As MPI is being developed as a new medical imaging modality, recovery of the shape of the target structures to be imaged is essential.

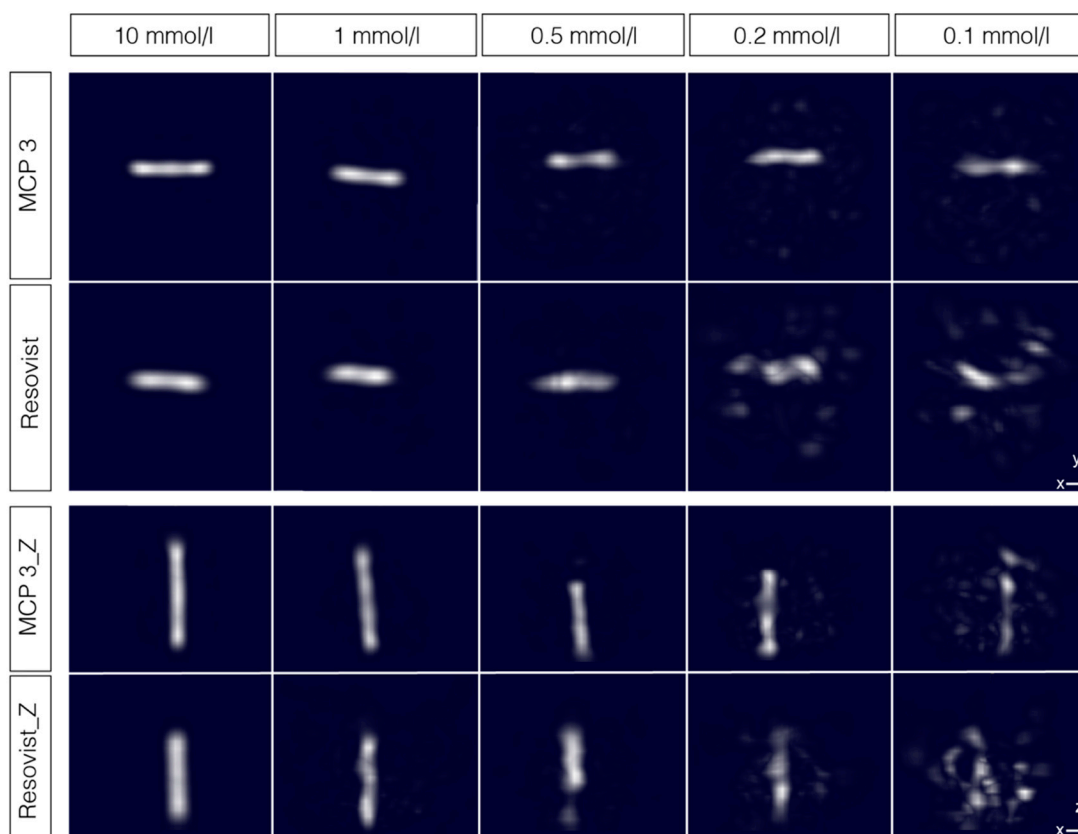


**Figure 8.** Reconstructed images of the phantom dilution series. PVC tubes with an inner diameter of 3 mm and filled with MCP 3 and Resovist<sup>®</sup> at concentrations from 10 to 0.1 mM Fe. The tubes were measured in two orientations to take the different gradients of the selection field into account. Images are interpolated and represented as maximum intensity projections with the threshold set at 50%. For images of phantoms filled with 2 and 5 mmol Fe/l, please see supplement Figure S7.

### 3.3.2. Determination of Volumes and Iron Amounts in the Phantom Dilution Series

For the determination of total volumes and iron contents of the phantoms in the dilution series, the reconstructed images were segmented into two regions: the region of interest (ROI), i.e., the investigated phantom, and background. The total volume was then calculated as the sum of the voxels within the ROI, and the corresponding iron content was determined by the integration of the iron content within this region. The results are shown in Figure 9.

The high noise and artifact levels precluded determination of the total volume and iron content of the phantoms filled with 0.1 mmol Fe/l Resovist<sup>®</sup> in both x- and z-orientation. Our method allowed determination of the volumes of both tracers in the two orientations with arithmetic mean deviation of  $\pm 28\%$  (for numerical percentages, please see supplement Tables S9 and S10). Overall, the results for MCP 3 were closer to the volume reference values of 90  $\mu\text{L}$  than those for Resovist<sup>®</sup>. The only noticeable result for MCP 3 was the high value in z-orientation with the lowest concentration of 0.1 mmol Fe/l. This can be explained by background noise at this very low concentration and the resulting false ROI segmentation. Iron contents found for MCP 3 and Resovist<sup>®</sup> were generally lower than the iron amount setpoints. This can be attributed to the threshold-based segmentation approach and partial volume effects due to the limited resolution of MPI. Another possible contributing factor is the not ideal magnetic behavior of MPI tracers with their slow response to the magnetic fields, which also limits the spatial resolution that can be achieved and is a possible reason for underestimation of volumes and iron amounts [54]. It is striking that the results for the iron content of MCP with 0.5 mmol Fe/l in x-orientation deviate from the general trend. Overall the MCP 3 values of total volume and iron content are closer to the respective setpoints than those of Resovist<sup>®</sup>.

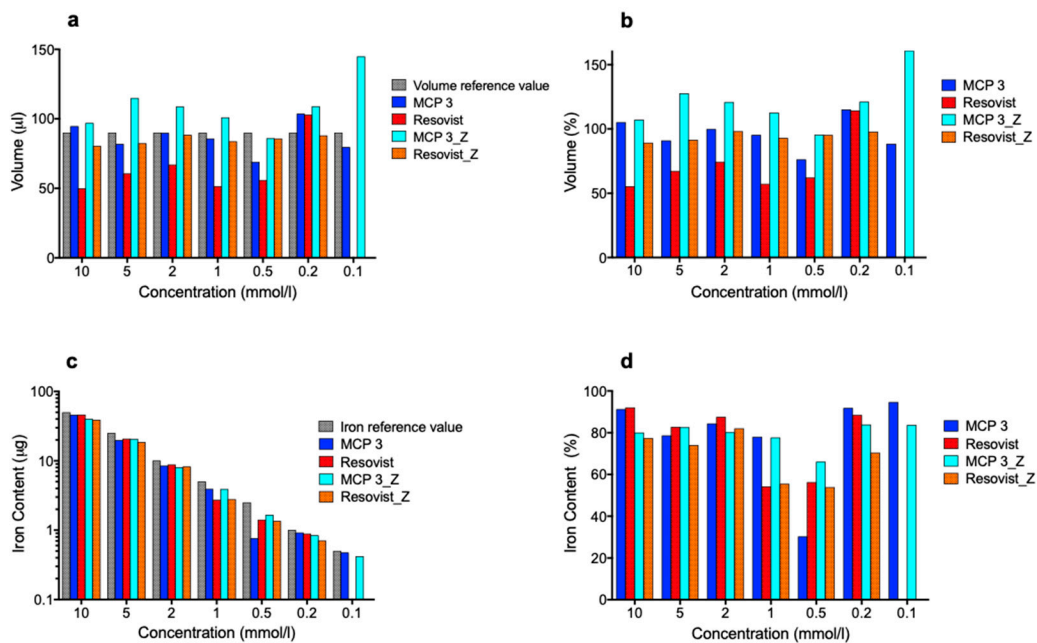


**Figure 9.** Determination of volume and iron content in the phantom dilution series: volume in absolute terms (a) and in relation to the reference volume (b), iron content in absolute terms (c), and in relation to the absolute iron content (d).

### 3.3.3. Dual-Tube Phantoms

For assessing especially, the selectivity of MCP 3 with a view to potential *in vivo* use, all possible combinations of two tubes were assembled and filled then with 10 mmol Fe/l tracer dispersion. The resulting 12 phantoms were measured in two orientations, one parallel to the higher gradient in *z* direction and another parallel to a lower gradient in *x* direction (Figure 10). This was done considering the higher spatial resolution in the orientation of the higher gradient as a consequence of the asymmetry of the selection field.

The similar assembled dual-tube phantoms of 2 and 3 mm inner diameter are well resolved and separated from one another, except for the Resovist<sup>®</sup> phantom with 2 mm inner diameter in *x-y*-orientation, where the two tubes are poorly separated. The phantoms with 1 mm inner diameter are indistinguishable and appear as a single object.

The dual-tube phantoms with combinations of different inner diameters with 2 and 3 mm are well resolved and separated from one another. In the cases of phantoms with combinations of 3 mm and 1 mm as well as 2 mm and 1 mm, only the tubes with the larger diameter are clearly visible. The smaller tubes are only visible after adjustment of brightness and contrast, such as for the MCP 3 phantoms in *z*-orientation in both cases (please see supplement Figure S8).

A large difference in the iron amount of two objects present in the FOV results in the suppression of the object with the lower iron amount. This is known as the “shadowing effect”, which becomes more conspicuous as the ratio between the two different iron amounts increases [55]. This effect is considerably less pronounced for MCP 3 compared with Resovist<sup>®</sup>. The iron amount ratios for the 3 + 1 mm and 2 + 1 mm phantoms are 9:1 and 4:1, respectively.

In addition, the MPI properties of MCP 3 were also assessed with similar combined dual-tube phantoms with 3, 2 and 1 mm inner diameter filled with 1 mmol Fe/l MCP 3 and Resovist<sup>®</sup> (Figure 11). The results for the 3- and 2-mm phantoms are consistent with the results obtained for 10 mmol/l, except for the 2-mm phantoms in *x-y*-orientation, which appears to be the limit for differentiation of the two tubes using MCP 3. The equivalent Resovist<sup>®</sup> phantom is visually one object. All 1-mm phantoms are visually one object in *x-y* orientation and show artifacts in *x-z* orientation. In the *x-z*-orientation of

the MCP 3-filled 1-mm phantom, one can guess the existence of two tubes, but they are not clearly separated from each other.

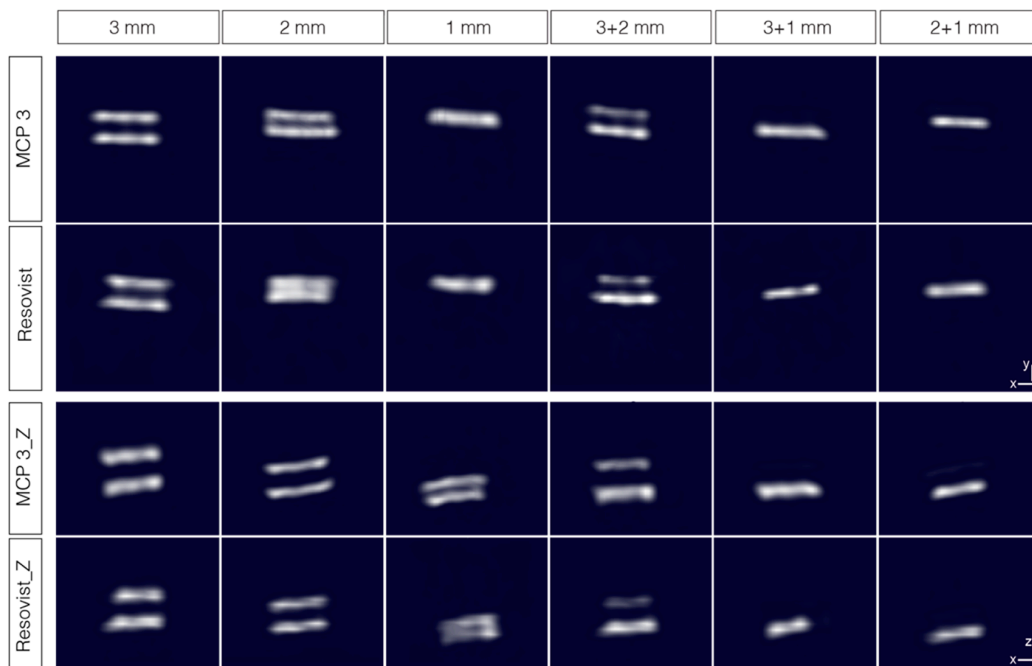


**Figure 10.** Dual-tube phantoms combining tubes of identical and different inner diameters (of 1, 2, and 3 mm) with MCP 3 and Resovist® at 10 mmol Fe/l and measured in two orientations. Images are interpolated and represented as maximum intensity projections with the threshold set at 50%.

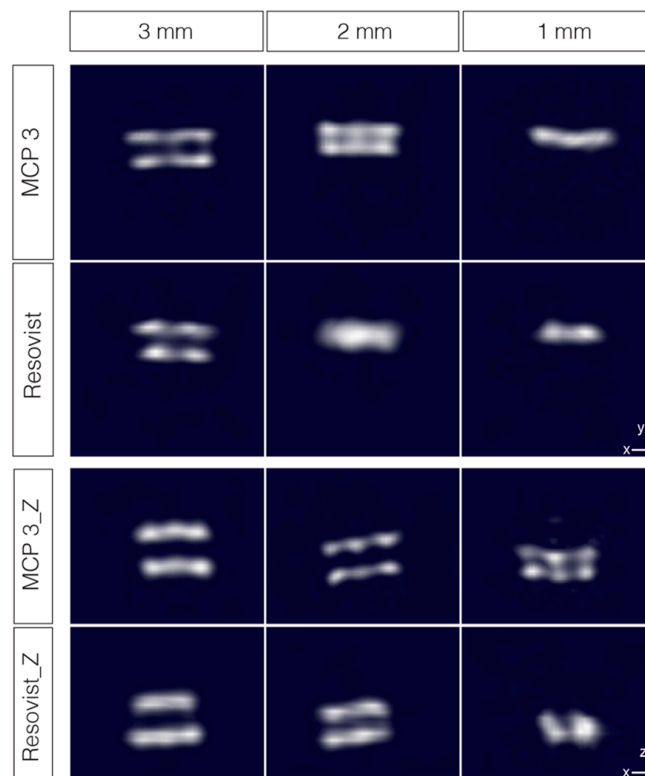


**Figure 11.** Dual-tube phantoms of 3, 2, and 1 mm inner diameter, filled with 1 mmol Fe/l MCP 3 and Resovist® and measured in two orientations. Images are interpolated and represented as maximum intensity projections with the threshold set at 50%.

In summary, the dual-tube phantoms prepared with the lower concentration of 1 mmol Fe/l MCP 3 provide more selectivity, spatial resolution, and a lower artifact level compared with the corresponding phantoms prepared with Resovist<sup>®</sup>, and the two tubes were distinguishable down to an inner diameter of 2 mm.

#### 4. Conclusions

The new MCP 3 generates an MPS signal amplitude which is about five times stronger than the signal achieved with Resovist<sup>®</sup>. Embedding of the MNP in PAA gel is a good simulation of the fully or partially immobilized state of MNP after uptake into the liver or spleen. Even under these conditions, the signal produced by MCP 3 is still three to four times higher compared with Resovist<sup>®</sup>. These excellent MPS results were also confirmed by our phantom experiments in the MPI scanner. The evaluation of the optimal regularization factor  $\lambda$  also indicated the higher SNR for MCP 3. These results are also consistent with the observed better resolution and better visualization of phantom geometry seen for MCP 3 versus Resovist<sup>®</sup>. MCP 3 also shows excellent selectivity in the dual-tube phantom experiments in both orientations parallel to the higher gradient in z direction and the lower gradient in x direction. Our results demonstrate the superiority of MCP 3 over Resovist<sup>®</sup> for all investigated MPI characteristics, suggesting that MCP 3 is a promising candidate for future in vivo studies. The strong shadowing effect, observed especially for Resovist<sup>®</sup>, suppresses the signal of smaller iron amounts in the presence of larger ones and might be a potential challenge in prospective in vivo investigations, for instance in the imaging of adjacent blood vessels of different diameters. Compared to our previously presented initial MCP the new MCP 3 show a much higher MPS/MPI signal, which could be achieved by optimizing the synthesis regarding a better control over the resulting magnetic core diameters. The results obtained with MCP 3 also show that the coprecipitation method is well suitable to develop high-performance MPI tracers.

**Supplementary Materials:** The following are available online at <http://www.mdpi.com/2079-4991/9/10/1466/s1>, Text S1: Synthesis of MCP 3, Figure S2: Magnified TEM image of MCP 3 (1/3), Figure S3: Magnified TEM image of MCP 3 (2/3), Figure S4: Magnified TEM image of MCP 3 (3/3), Figure S5: DLS data of MCP 3 (volume and intensity data, mean of 6 measurements), Text S6: System function parameters, Figure S7: Dilution series concentrations 2 and 5 mmol Fe/l (Images are interpolated and represented as maximum intensity projection with threshold set at 50%), Figure S8: Dual-tube phantoms filled with 10 mmol Fe/l MCP 3 and Resovist<sup>®</sup> processed with extreme brightness and contrast values, Table S9: Percent values of the dilution series data analysis (volume measurement), Table S10: Percent values of the dilution series data analysis (iron content).

**Author Contributions:** Conceptualization, H.K. and A.M.; methodology, H.K., A.M., D.E., and O.K.; software, A.M., O.K., and D.E.; validation, H.K., A.M., D.E., O.K., and F.W.; formal analysis, H.K., A.M., and D.E.; investigation, H.K., A.M., D.E., and O.K.; resources, R.H.; writing—original draft preparation, H.K.; writing—review and editing, A.M., D.E., O.K., F.W., M.T., and J.S.; visualization, H.K. and A.M.; supervision, J.S.; project administration, H.K.; funding acquisition, F.W., M.T., B.H., and J.S.

**Funding:** Funded by the German Research Foundation (DFG, Deutsche Forschungsgemeinschaft)-Projektnummer 372486779-CRC 1340 (SFB 1340)-“Matrix in vision” - projects A02 and C01, and Research Training Group 2260 (BIOQIC). We also acknowledge additional support from the German Research Foundation (DFG) and the Open Access Publication Fund of Charité–Universitätsmedizin Berlin.

**Acknowledgments:** We thank Bettina Herwig for language editing, Monika Ebert for analysis of iron(II) and Sören Selve for conducting the TEM investigations at ZELMI (TU Berlin).

**Conflicts of Interest:** The authors declare no conflict of interest.

#### References

1. Gleich, B.; Weizenecker, J. Tomographic imaging using the nonlinear response of magnetic particles. *Nature* **2005**, *435*, 1214–1217. [[CrossRef](#)] [[PubMed](#)]
2. Haegele, J.; Duschka, R.L.; Graeser, M.; Schaecke, C.; Panagiotopoulos, N.; Ludtke-Buzug, K.; Buzug, T.M.; Barkhausen, J.; Vogt, F.M. Magnetic particle imaging: Kinetics of the intravascular signal in vivo. *Int. J. Nanomed.* **2014**, *9*, 4203–4209. [[CrossRef](#)] [[PubMed](#)]

3. Weizenecker, J.; Gleich, B.; Rahmer, J.; Dahnke, H.; Borgert, J. Three-dimensional real-time in vivo magnetic particle imaging. *Phys. Med. Biol.* **2009**, *54*, L1–L10. [[CrossRef](#)] [[PubMed](#)]
4. Borgert, J.; Schmidt, J.D.; Schmale, I.; Rahmer, J.; Bontus, C.; Gleich, B.; David, B.; Eckart, R.; Woywode, O.; Weizenecker, J.; et al. Fundamentals and applications of magnetic particle imaging. *J. Cardiovasc. Comput. Tomogr.* **2012**, *6*, 149–153. [[CrossRef](#)]
5. Kratz, H.; Eberbeck, D.; Wagner, S.; Taupitz, M.; Schnorr, J. Synthetic routes to magnetic nanoparticles for MPI. *Biomed. Tech.* **2013**, *58*, 509–515. [[CrossRef](#)]
6. Franke, J.; Heinen, U.; Lehr, H.; Weber, A.; Jaspard, F.; Ruhm, W.; Heidenreich, M.; Schulz, V. System characterization of a highly integrated preclinical hybrid MPI-MRI scanner. *IEEE Trans. Med. Imaging* **2016**, *35*, 1993–2004. [[CrossRef](#)]
7. Rahmer, J.; Antonelli, A.; Sfara, C.; Tiemann, B.; Gleich, B.; Magnani, M.; Weizenecker, J.; Borgert, J. Nanoparticle encapsulation in red blood cells enables blood-pool magnetic particle imaging hours after injection. *Phys. Med. Biol.* **2013**, *58*, 3965–3977. [[CrossRef](#)]
8. Kaul, M.G.; Weber, O.; Heinen, U.; Reitmeier, A.; Mummert, T.; Jung, C.; Raabe, N.; Knopp, T.; Ittrich, H.; Adam, G. Combined Preclinical Magnetic Particle Imaging and Magnetic Resonance Imaging: Initial Results in Mice. *Rofa* **2015**, *187*, 347–352. [[CrossRef](#)]
9. Nishimoto, K.; Mimura, A.; Aoki, M.; Banura, N.; Murase, K. Application of Magnetic Particle Imaging to Pulmonary Imaging Using Nebulized Magnetic Nanoparticles. *Open J. Med. Imaging* **2015**, *5*, 49–55. [[CrossRef](#)]
10. Zheng, B.; Vazin, T.; Goodwill, P.W.; Conway, A.; Verma, A.; Saritas, E.U.; Schaffer, D.; Conolly, S.M. Magnetic Particle Imaging tracks the long-term fate of in vivo neural cell implants with high image contrast. *Sci. Rep.* **2015**, *5*, 14055. [[CrossRef](#)]
11. Ohki, A.; Tanoue, M.; Kobayashi, S.; Murase, K. Magnetic Particle Imaging for Quantitative Evaluation of Tumor Response to Magnetic Hyperthermia Treatment Combined with Chemotherapy Using Cisplatin. *Therm. Med.* **2017**, *33*, 39–51. [[CrossRef](#)]
12. Kuboyabu, T.; Yabata, I.; Aoki, M.; Banura, N.; Nishimoto, K.; Mimura, A.; Murase, K. Magnetic Particle Imaging for Magnetic Hyperthermia Treatment: Visualization and Quantification of the Intratumoral Distribution and Temporal Change of Magnetic Nanoparticles in Vivo. *Open J. Med. Imaging* **2016**, *6*, 1–15. [[CrossRef](#)]
13. Vogel, P.; Ruckert, M.A.; Klauer, P.; Kullmann, W.H.; Jakob, P.M.; Behr, V.C. First in vivo traveling wave magnetic particle imaging of a beating mouse heart. *Phys. Med. Biol.* **2016**, *61*, 6620–6634. [[CrossRef](#)] [[PubMed](#)]
14. Zheng, B.; von See, M.P.; Yu, E.; Gunel, B.; Lu, K.; Vazin, T.; Schaffer, D.V.; Goodwill, P.W.; Conolly, S.M. Quantitative Magnetic Particle Imaging Monitors the Transplantation, Biodistribution, and Clearance of Stem Cells In Vivo. *Theranostics* **2016**, *6*, 291–301. [[CrossRef](#)] [[PubMed](#)]
15. Dieckhoff, J.; Kaul, M.G.; Mummert, T.; Jung, C.; Salamon, J.; Adam, G.; Knopp, T.; Ludwig, F.; Balceris, C.; Ittrich, H. In vivo liver visualizations with magnetic particle imaging based on the calibration measurement approach. *Phys. Med. Biol.* **2017**, *62*, 3470–3482. [[CrossRef](#)]
16. Kaul, M.G.; Mummert, T.; Jung, C.; Salamon, J.; Khandhar, A.P.; Ferguson, R.M.; Kemp, S.J.; Ittrich, H.; Krishnan, K.M.; Adam, G.; et al. In vitro and in vivo comparison of a tailored magnetic particle imaging blood pool tracer with Resovist. *Phys. Med. Biol.* **2017**, *62*, 3454–3469. [[CrossRef](#)]
17. Ohki, A.; Kuboyabu, T.; Aoki, M.; Yamawaki, M.; Murase, K. Quantitative Evaluation of Tumor Response to combination of Magnetic Hyperthermia Treatment and Radiation Therapy using Magnetic Particle Imaging. *Int. J. Nanomed. Nanosurgery* **2016**, *2*. [[CrossRef](#)]
18. Khandhar, A.P.; Keselman, P.; Kemp, S.J.; Ferguson, R.M.; Goodwill, P.W.; Conolly, S.M.; Krishnan, K.M. Evaluation of PEG-coated iron oxide nanoparticles as blood pool tracers for preclinical magnetic particle imaging. *Nanoscale* **2017**, *9*, 1299–1306. [[CrossRef](#)]
19. Starmans, L.W.; Burdinski, D.; Haex, N.P.; Moonen, R.P.; Strijkers, G.J.; Nicolay, K.; Grull, H. Iron oxide nanoparticle-micelles (ION-micelles) for sensitive (molecular) magnetic particle imaging and magnetic resonance imaging. *PLoS ONE* **2013**, *8*, e57335. [[CrossRef](#)]
20. Ziemian, S.; Lowa, N.; Kosch, O.; Bajj, D.; Wiekhorst, F.; Schutz, G. Optimization of Iron Oxide Tracer Synthesis for Magnetic Particle Imaging. *Nanomaterials* **2018**, *8*, 180. [[CrossRef](#)]

21. Eberbeck, D.; Dennis, C.L.; Huls, N.F.; Krycka, K.L.; Gruttner, C.; Westphal, F. Multicore Magnetic Nanoparticles for Magnetic Particle Imaging. *IEEE Trans. Magn.* **2013**, *49*, 269–274. [[CrossRef](#)]
22. Tay, Z.W.; Chandrasekharan, P.; Zhou, X.Y.; Yu, E.; Zheng, B.; Conolly, S. In vivo tracking and quantification of inhaled aerosol using magnetic particle imaging towards inhaled therapeutic monitoring. *Theranostics* **2018**, *8*, 3676–3687. [[CrossRef](#)] [[PubMed](#)]
23. Bender, P.; Fock, J.; Frandsen, C.; Hansen, M.F.; Balceris, C.; Ludwig, F.; Posth, O.; Wetterskog, E.; Bogart, L.K.; Southern, P.; et al. Relating Magnetic Properties and High Hyperthermia Performance of Iron Oxide Nanoflowers. *J. Phys. Chem. C* **2018**, *122*, 3068–3077. [[CrossRef](#)]
24. Lu, A.H.; Salabas, E.L.; Schuth, F. Magnetic nanoparticles: Synthesis, protection, functionalization, and application. *Angew. Chem. Int. Ed.* **2007**, *46*, 1222–1244. [[CrossRef](#)] [[PubMed](#)]
25. Cotin, G.; Kiefer, C.; Pertont, F.; Ihiawakrim, D.; Blanco-Andujar, C.; Moldovan, S.; Lefevre, C.; Ersen, O.; Pichon, B.; Mertz, D.; et al. Unravelling the Thermal Decomposition Parameters for The Synthesis of Anisotropic Iron Oxide Nanoparticles. *Nanomaterials* **2018**, *8*, 881. [[CrossRef](#)] [[PubMed](#)]
26. Kratz, H.; Taupitz, M.; Ariza de Schellenberger, A.; Kosch, O.; Eberbeck, D.; Wagner, S.; Trahms, L.; Hamm, B.; Schnorr, J. Novel magnetic multicore nanoparticles designed for MPI and other biomedical applications: From synthesis to first in vivo studies. *PLoS ONE* **2018**, *13*, e0190214. [[CrossRef](#)] [[PubMed](#)]
27. Laurent, S.; Forge, D.; Port, M.; Roch, A.; Robic, C.; Vander Elst, L.; Muller, R.N. Magnetic iron oxide nanoparticles: Synthesis, stabilization, vectorization, physicochemical characterizations, and biological applications. *Chem. Rev.* **2008**, *108*, 2064–2110. [[CrossRef](#)]
28. Eberbeck, D.; Wiekhorst, F.; Wagner, S.; Trahms, L. How the size distribution of magnetic nanoparticles determines their magnetic particle imaging performance. *Appl. Phys. Lett.* **2011**, *98*. [[CrossRef](#)]
29. Ferguson, R.M.; Khandhar, A.P.; Arami, H.; Hua, L.; Hovorka, O.; Krishnan, K.M. Tailoring the magnetic and pharmacokinetic properties of iron oxide magnetic particle imaging tracers. *Biomed. Tech.* **2013**, *58*, 493–507. [[CrossRef](#)]
30. Scharlach, C.; Müller, L.; Wagner, S.; Kobayashi, Y.; Kratz, H.; Ebert, M.; Jakubowski, N.; Schellenberger, E. LA-ICP-MS Allows Quantitative Microscopy of Europium-Doped Iron Oxide Nanoparticles and is a Possible Alternative to Ambiguous Prussian Blue Iron Staining. *J. Biomed. Nanotechnol.* **2016**, *12*, 1001–1010. [[CrossRef](#)] [[PubMed](#)]
31. Wells, J.; Paysen, H.; Kosch, O.; Löwa, N.; Schmitzberger, F.; Makowski, M.; Franke, J.; Trahms, L.; Wiekhorst, F. Characterizing a Preclinical Magnetic Particle Imaging System with Separate Pickup Coil. *IEEE Trans. Magn.* **2017**, *53*, 1–5. [[CrossRef](#)]
32. Paysen, H.; Wells, J.; Kosch, O.; Steinhoff, U.; Franke, J.; Trahms, L.; Schaeffter, T.; Wiekhorst, F. Improved sensitivity and limit-of-detection using a receive-only coil in magnetic particle imaging. *Phys. Med. Biol.* **2018**, *63*, 13NT02. [[CrossRef](#)] [[PubMed](#)]
33. Them, K.; Kaul, M.G.; Jung, C.; Hofmann, M.; Mummert, T.; Werner, F.; Knopp, T. Sensitivity Enhancement in Magnetic Particle Imaging by Background Subtraction. *IEEE Trans. Med. Imaging* **2016**, *35*, 893–900. [[CrossRef](#)] [[PubMed](#)]
34. Hansen, P.C. *Discrete Inverse Problems: Insight and Algorithms*; Siam: Philadelphia, PA, USA, 2010.
35. Hemalatha, R.J.; Thamizhvani, T.R.; Dhivya, A.J.A.; Joseph, J.E.; Babu, B.; Chandrasekaran, R. Active Contour Based Segmentation Techniques for Medical Image Analysis. In *Medical and Biological Image Analysis*; IntechOpen: London, UK, 2018.
36. Reimer, P.; Balzer, T. Ferucarbotran (Resovist): A new clinically approved RES-specific contrast agent for contrast-enhanced MRI of the liver: Properties, clinical development, and applications. *Eur. Radiol.* **2003**, *13*, 1266–1276. [[CrossRef](#)]
37. Wang, Y.X. Superparamagnetic iron oxide based MRI contrast agents: Current status of clinical application. *Quant. Imaging Med. Surg.* **2011**, *1*, 35–40. [[CrossRef](#)]
38. Hyeon, T.; Lee, S.S.; Park, J.; Chung, Y.; Bin Na, H. Synthesis of highly crystalline and monodisperse maghemite nanocrystallites without a size-selection process. *J. Am. Chem. Soc.* **2001**, *123*, 12798–12801. [[CrossRef](#)]
39. Roca, A.G.; Marco, J.F.; Morales, M.D.; Serna, C.J. Effect of nature and particle size on properties of uniform magnetite and maghemite nanoparticles. *J. Phys. Chem. C* **2007**, *111*, 18577–18584. [[CrossRef](#)]
40. Kaiser, R.; Miskolczy, G. Magnetic properties of stable dispersions of subdomain magnetite particles. *J. Appl. Phys.* **1970**, *41*, 1064–1072. [[CrossRef](#)]

41. Anthore, R.; Petipas, C.; Chandesris, D.; Martinet, A. X-ray and magnetization studies of the geometrical parameters of the grains of a ferrofluid. *Le J. De Phys. Colloq.* **1977**, *38*, C2–C203.
42. Chantrell, R.; Popplewell, J.; Charles, S. Measurements of particle size distribution parameters in ferrofluids. *IEEE Trans. Magn.* **1978**, *14*, 975–977. [[CrossRef](#)]
43. O’Grady, K.; Bradbury, A.; Popplewell, J.; Charles, S.; Chantrell, R. The effect of field induced texture on the properties of a fine particle system. *J. Magn. Magn. Mater.* **1985**, *49*, 106–116. [[CrossRef](#)]
44. Van Leeuwen, D.A.; van Ruitenbeek, J.M.; de Jongh, L.J.; Ceriotti, A.; Pacchioni, G.; Haberlen, O.D.; Rosch, N. Quenching of magnetic moments by ligand-metal interactions in nanosized magnetic metal clusters. *Phys. Rev. Lett.* **1994**, *73*, 1432–1435. [[CrossRef](#)] [[PubMed](#)]
45. Millan, A.; Urtizberea, A.; Silva, N.; Palacio, F.; Amaral, V.; Snoeck, E.; Serin, V. Surface effects in maghemite nanoparticles. *J. Magn. Magn. Mater.* **2007**, *312*, L5–L9. [[CrossRef](#)]
46. Ahrens, T.J. *Rock Physics & Phase Relations*; Wiley Online Library: Hoboken, NJ, USA, 1995.
47. Biederer, S.; Knopp, T.; Sattel, T.; Lüdtke-Buzug, K.; Gleich, B.; Weizenecker, J.; Borgert, J.; Buzug, T. Magnetization response spectroscopy of superparamagnetic nanoparticles for magnetic particle imaging. *J. Phys. D Appl. Phys.* **2009**, *42*, 205007. [[CrossRef](#)]
48. Arami, H.; Khandhar, A.; Liggitt, D.; Krishnan, K.M. In vivo delivery, pharmacokinetics, biodistribution and toxicity of iron oxide nanoparticles. *Chem. Soc. Rev.* **2015**, *44*, 8576–8607. [[CrossRef](#)]
49. Blyakhman, F.A.; Makarova, E.B.; Fadeyev, F.A.; Lugovets, D.V.; Safronov, A.P.; Shabadrov, P.A.; Shklyar, T.F.; Melnikov, G.Y.; Orue, I.; Kurlyanskaya, G.V. The Contribution of Magnetic Nanoparticles to Ferrogel Biophysical Properties. *Nanomaterials* **2019**, *9*, 232. [[CrossRef](#)] [[PubMed](#)]
50. Arbab, A.S.; Wilson, L.B.; Ashari, P.; Jordan, E.K.; Lewis, B.K.; Frank, J.A. A model of lysosomal metabolism of dextran coated superparamagnetic iron oxide (SPIO) nanoparticles: Implications for cellular magnetic resonance imaging. *NMR Biomed.* **2005**, *18*, 383–389. [[CrossRef](#)]
51. Wisotzki, E.I.; Eberbeck, D.; Kratz, H.; Mayr, S.G. Magnetic response of gelatin ferrogels across the sol-gel transition: The influence of high energy crosslinking on thermal stability. *Soft Matter* **2016**, *12*, 3908–3918. [[CrossRef](#)]
52. Rahmer, J.; Weizenecker, J.; Gleich, B.; Borgert, J. Analysis of a 3-D system function measured for magnetic particle imaging. *IEEE Trans. Med. Imaging* **2012**, *31*, 1289–1299. [[CrossRef](#)]
53. Vaalma, S.; Rahmer, J.; Panagiotopoulos, N.; Duschka, R.L.; Borgert, J.; Barkhausen, J.; Vogt, F.M.; Haegele, J. Magnetic Particle Imaging (MPI): Experimental Quantification of Vascular Stenosis Using Stationary Stenosis Phantoms. *PLoS ONE* **2017**, *12*, e0168902. [[CrossRef](#)]
54. Rahmer, J.; Weizenecker, J.; Gleich, B.; Borgert, J. Signal encoding in magnetic particle imaging: properties of the system function. *BMC Med. Imaging* **2009**, *9*, 4. [[CrossRef](#)] [[PubMed](#)]
55. Knopp, T.; Gdaniec, N.; Moddel, M. Magnetic particle imaging: from proof of principle to preclinical applications. *Phys. Med. Biol.* **2017**, *62*, R124–R178. [[CrossRef](#)] [[PubMed](#)]



© 2019 by the authors. Licensee MDPI, Basel, Switzerland. This article is an open access article distributed under the terms and conditions of the Creative Commons Attribution (CC BY) license (<http://creativecommons.org/licenses/by/4.0/>).

# Publication B: In vivo magnetic particle imaging: angiography of inferior vena cava and aorta in rats using newly developed multicore particles

Journal Data Filtered By: **Selected JCR Year: 2018** Selected Editions: SCIE,SSCI  
 Selected Categories: **"MULTIDISCIPLINARY SCIENCES"** Selected Category  
 Scheme: WoS

**Gesamtanzahl: 69 Journale**

Rank	Full Journal Title	Total Cites	Journal Impact Factor	Eigenfactor Score
1	NATURE	745,692	43.070	1.285010
2	SCIENCE	680,994	41.037	1.070190
3	National Science Review	1,842	13.222	0.006500
4	Science Advances	21,901	12.804	0.110010
5	Nature Communications	243,793	11.878	1.103290
6	Nature Human Behaviour	1,230	10.575	0.006550
7	PROCEEDINGS OF THE NATIONAL ACADEMY OF SCIENCES OF THE UNITED STATES OF AMERICA	661,118	9.580	1.022190
8	Science Bulletin	3,569	6.277	0.009840
9	Scientific Data	3,240	5.929	0.015610
10	Frontiers in Bioengineering and Biotechnology	1,994	5.122	0.006540
11	Journal of Advanced Research	2,691	5.045	0.004780
12	Research Synthesis Methods	1,932	5.043	0.005420
13	GigaScience	2,674	4.688	0.012510
14	Annals of the New York Academy of Sciences	46,385	4.295	0.025840
15	Scientific Reports	302,086	4.011	1.061540
16	Journal of the Royal Society Interface	12,933	3.224	0.029190
17	NPJ Microgravity	203	3.111	0.000670
18	PHILOSOPHICAL TRANSACTIONS OF THE ROYAL SOCIETY A-MATHEMATICAL PHYSICAL AND ENGINEERING SCIENCES	19,227	3.093	0.028200



OPEN

# In vivo magnetic particle imaging: angiography of inferior vena cava and aorta in rats using newly developed multicore particles

Azadeh Mohtashamdolatshahi<sup>1✉</sup>, Harald Kratz<sup>1</sup>, Olaf Kosch<sup>2</sup>, Ralf Hauptmann<sup>1</sup>, Nicola Stolzenburg<sup>1</sup>, Frank Wiekhorst<sup>2</sup>, Ingolf Sack<sup>1</sup>, Bernd Hamm<sup>1</sup>, Matthias Taupitz<sup>1</sup> & Jörg Schnorr<sup>1</sup>

Magnetic Particle Imaging (MPI) is a new imaging modality, which maps the distribution of magnetic nanoparticles (MNP) in 3D with high temporal resolution. It thus may be suited for cardiovascular imaging. Its sensitivity and spatial resolution critically depend on the magnetic properties of MNP. Therefore, we used novel multicore nanoparticles (MCP 3) for in-vivo MPI in rats and analyzed dose requirements, sensitivity and detail resolution. 8 rats were examined using a preclinical MPI scanner (Bruker Biospin GmbH, Germany) equipped with a separate receive coil. MCP 3 and Resovist were administered intravenously (i.v.) into the rats' tail veins at doses of 0.1, 0.05 and 0.025 mmol Fe/kg followed by serial MPI acquisition with a temporal resolution of 46 volumes per second. Based on a qualitative visual scoring system MCP 3–MPI images showed a significantly ( $P \leq 0.05$ ) higher image quality than Resovist–MPI images. Morphological features such as vessel lumen diameters ( $D_L$ ) of the inferior vena cava (IVC) and abdominal aorta (AA) could be assessed along a 2-cm segment in mesenteric area only after administration of MCP 3 at dosages of 0.1, 0.05 mmol Fe/kg. The mean  $D_L \pm SD$  estimated was  $2.7 \pm 0.6$  mm for IVC and  $2.4 \pm 0.7$  mm for AA. Evaluation of  $D_L$  of the IVC and AA was not possible in Resovist–MPI images. Our results show, that MCP 3 provide better image quality at a lower dosage than Resovist. MCP 3–MPI with a clinically acceptable dose of 0.05 mmol Fe/kg increased the visibility of vessel lumens compared to Resovist-based MPI towards possible detection of vascular abnormalities such as stenosis or aneurysms, in vivo.

## Abbreviations

AA	Abdominal aorta
CDX	Carboxydextran
CMD	Carboxymethyl dextran
$D_L$	Lumen diameter
DLS	Dynamic light scattering
FFP	Field-free point
FOV	Field of view
IVC	Inferior vena cava
MCP 3	Multicore nanoparticles
MNP	Magnetic nanoparticle
MPI	Magnetic particle imaging
SF	System function
TEM	Transmission electron microscopy
VGA	Visual grading analysis
VOI	Volume of interest

<sup>1</sup>Experimental Radiology, Department of Radiology, Charité-Universitätsmedizin Berlin, corporate member of Freie Universität Berlin, Humboldt-Universität zu Berlin, Berlin Institute of Health, Chariteplatz 1, 10117 Berlin, Germany. <sup>2</sup>Department of Medical Physics and Metrological Information Technology, Physikalisch-Technische Bundesanstalt (PTB), Abbestrasse 2-12, 10587 Berlin, Germany. ✉email: Azadeh.Mohtashamdolatshahi@charite.de

Magnetic particle imaging (MPI) was first introduced in 2005 by Gleich and Weizenecker<sup>1</sup>. MPI is a noninvasive, tomographic imaging modality that maps the 3D-distribution of magnetic nanoparticles (MNP) giving quantitative information on the local MNP concentrations. MPI furthermore allows for a high temporal resolution with 46 3D frames per second (f/s) at a spatial resolution in the millimeter range. MPI images display only the distribution of the MNP and do not contain morphologic background information. Thus, qualitatively, MPI images can be compared with tomographic radiotracer images, as e.g. obtained with Single Photon Emission Computed Tomography (SPECT). The detection of MNP is based on the nonlinear magnetization response of the particles when exposed to an oscillating external magnetic field<sup>2</sup>. MPI is commonly performed using iron oxide nanoparticles (Magnetite/Maghemite) with appropriate magnetic characteristics for MPI. The resolution of MPI images is determined by a combination of MPI scanner properties such as the power and slew rate of the magnetic field gradients, as well as the MNP used.

With further advances in MPI, a number of *in vitro* and *in vivo* studies have provided the proof of concept of cardiovascular imaging. The first *in vivo* MPI images were obtained in 2009 and visualized the circulatory system and the beating heart of a mouse<sup>2</sup>. The images depicted the large vessels including the vena cava and the cardiac chambers. Since then the heart and vena cava of mice have been repeatedly scanned with various MPI systems incorporating advances in MPI technology, such as X-space MPI<sup>3</sup>, traveling wave MPI (TWMPPI)<sup>4</sup>, and the use of sophisticated separate receive coils<sup>5,6</sup> or in tracer development such as LS-008 particles<sup>3,7</sup>. These studies have shown improvements in angiographic image quality by improving sensitivity and resolution. Phantom studies show that MPI allows quantitative visualization of vascular abnormalities such as stenosis<sup>8,9</sup> and aneurysm<sup>10,11</sup> or that MPI can be used to track MNP-labeled material for vascular interventions like balloon catheters<sup>12,13</sup>.

This study introduces newly developed multicore nanoparticle (MCP 3)<sup>14</sup> as tracers for cardiovascular MPI. To this end, we administered the new tracers into the tail vein of rats and then performed imaging in a commercial *in vivo* MPI system. The sensitivity of MPI for detecting MCP 3 was compared with that of conventional tracers (Resovist). Finally, we evaluated the capability of MCP 3-based MPI to assess *in vivo* anatomical features of the abdominal aorta (AA) and the inferior vena cava (IVC).

## Results

The temporal profiles of the iron concentration in the volume of interest (VOI) over IVC and AA are presented in Fig. 1. The propagation of bolus into the IVC ( $t_1$ —time point 1–1.5 s after injection) and arterial phase ( $t_2$ —approx. 2–3 s after initial MNP administration) is seen in the signal rise in iron concentration–time curves. It takes approx. 2 s for the bolus to pass from the site of *i.v.* injection until reaching the AA. The profiles of iron concentrations over time look different due to different injection speed as the injections were performed manually. The  $t_1$  and  $t_2$  time points were chosen accordingly based on visual assessment of reconstructed images, assuring uniform bolus distribution without any impact from manual injection. Images of IVC reconstructed at the time of peak of bolus or nearly after ( $t_1$ ) showed similar adequate image quality (Supplement S1) except for Resovist at dosage of 0.025 mmol Fe/Kg, where the IVC image provided adequate image quality only at time of peak of bolus. The contributing factors in the image quality in images of MCP 3 in comparison to Resovist are the higher signal amplitude and slower drop of higher harmonics (Supplement S2)<sup>14</sup>.

Examples of overlaid reconstructed images from two time points of  $t_1$  and  $t_2$  are presented in Fig. 2. The qualitative image analysis, shows a significant increase in MPI image quality with MCP 3 rather than Resovist. A detailed overview is reported in Fig. 3. Propagation of the bolus through the IVC was visualized clearly with all three doses of the two MNP however the arterial phase was discerned only with MCP 3 particles at administered dosages of 0.1 and 0.05 mmol Fe/kg with good adequate morphological information of AA. Minor artifacts were present in images acquired after MCP 3 administration, while more severe artifacts were apparent in images obtained with administration of Resovist.

Resolution of MPI is in the millimeter range, which does not allow clear differentiation of the adjacent IVC and AA. To clearly visualize the AA during arterial phase and quantitatively estimate lumen diameters ( $D_L$ ), a digital subtraction step was carried out during and after bolus passage in the IVC (Fig. 4). The term digital subtraction refers to subtraction of two temporally separated images, an early post-contrast image ( $t_1$ ) is subtracted from a late post-contrast image ( $t_2$ ). The subtracted images allowed clear separation and independent assessment of the two adjacent vessels. Quantification of the  $D_L$  of vessels was feasible at higher concentrations of MCP 3 (0.1 and 0.05 mmol Fe/kg). Mean  $D_L$  was calculated along the longitudinal axis of the AA and IVC (Fig. 4). Mean  $D_L \pm SD$  were as follows: (A) 0.1 mmol Fe/kg: IVC =  $2.7 \pm 0.7$ , AA =  $2.5 \pm 0.7$ ; (B) 0.05 mmol Fe/kg: IVC =  $2.8 \pm 0.6$ , AA =  $2.3 \pm 0.8$  in mm.

A signal modulation is seen in the raw signal (Fig. 5). From the periodicity of the signal and/or its Fourier spectrum, distinct biological frequencies can be derived. The signal modulation is largely attributable to respiratory motion of the anesthetized rats. Based on a temporal resolution of 46 3D f/s a respiratory rate of approximately 60 (breaths/minute) can be estimated. Monitoring the signal modulation in raw signal also assured the clearance of both MNP types out of blood stream prior to the subsequent injection. The gained knowledge in combination with data from literature<sup>7,15–18</sup> affirms that 1 h interval between the subsequent injections is sufficient not to influence the subsequent MPI scan.

## Discussion

MPI has potentially high sensitivity and high contrast. This combined with a high temporal resolution of 46 3D f/s makes MPI a promising technique for cardiovascular imaging. MPI physics relies on direct measurement of electronic magnetization of MNP, rather than nuclear magnetization as in MRI, hence a much higher sensitivity in detection of MNP in MPI is possible<sup>19</sup>. Former theoretical modeling studies predicted picogram sensitivity with MPI-optimal MNP<sup>20</sup>. *In vitro* data suggest that a MPI sensitivity below 100 ng can be achieved<sup>6,21</sup>. The

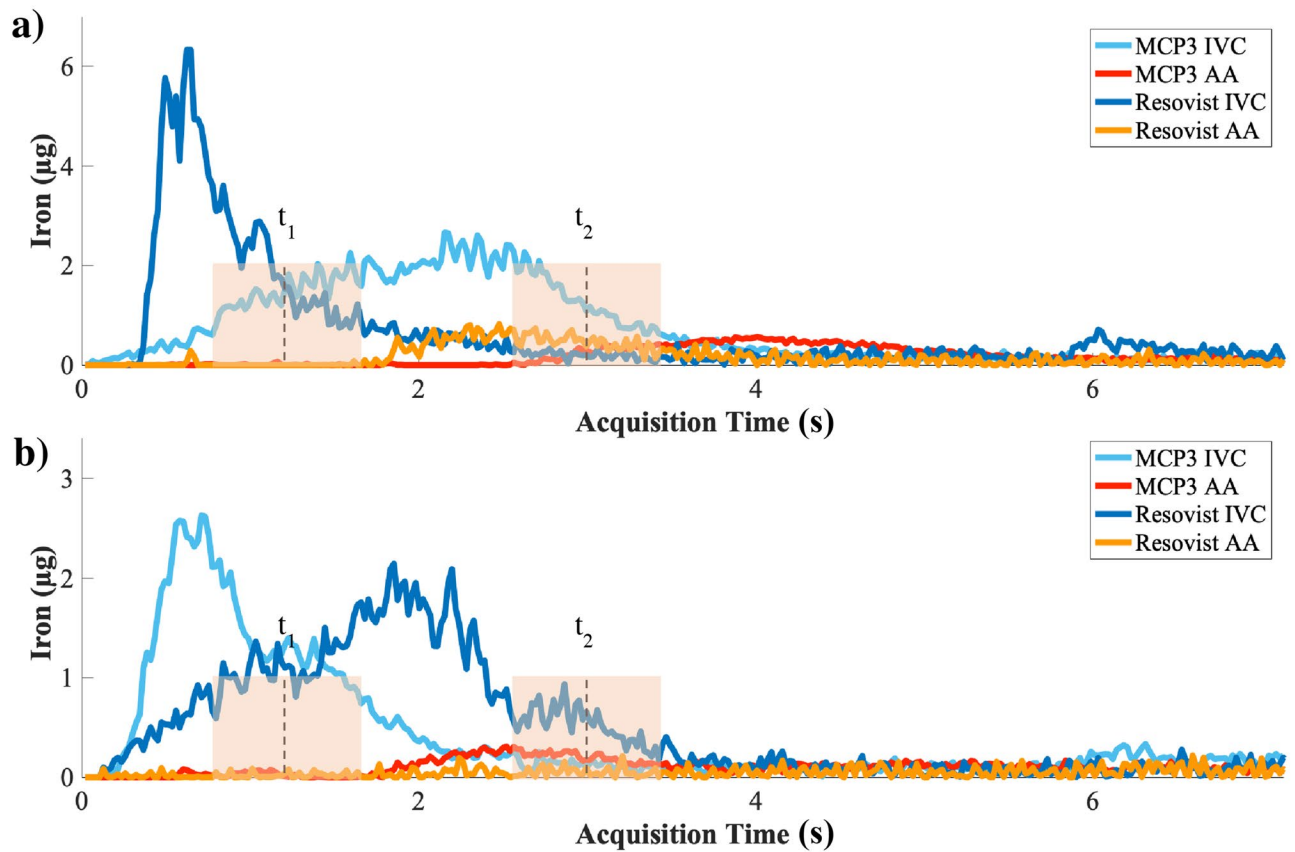


**Figure 1.** Iron concentration–time curves of the IVC and first-pass in the AA for both tracers, MCP 3 and Resovist, in the VOI defined in imaging data acquired. Shown are curves for administered doses of 0.1 mmol Fe/kg (a) and 0.05 mmol Fe/kg (b). The iron level of Resovist-based arterial phase in (b) is hardly distinguishable from noise.  $t_1$  and  $t_2$  indicate the time points when bolus in IVC and arterial phase in AA were further analysed.

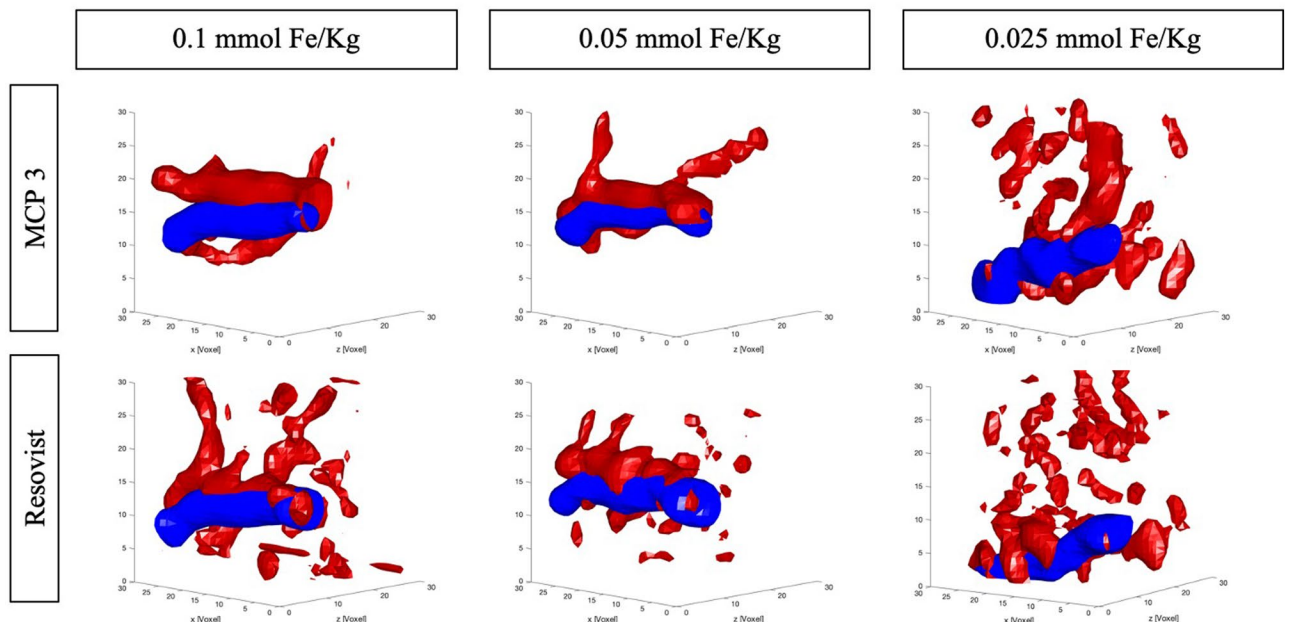


**Figure 2.** In vivo MPI images of the IVC (blue) and arterial phase (red) in rats. Arterial phase is clearly visible without degradation by artifacts with higher dosages of MCP 3. Conversely, arterial phase is hardly detectable with Resovist, and the images are characterized by an overall lower image quality and more severe background noise artifacts.

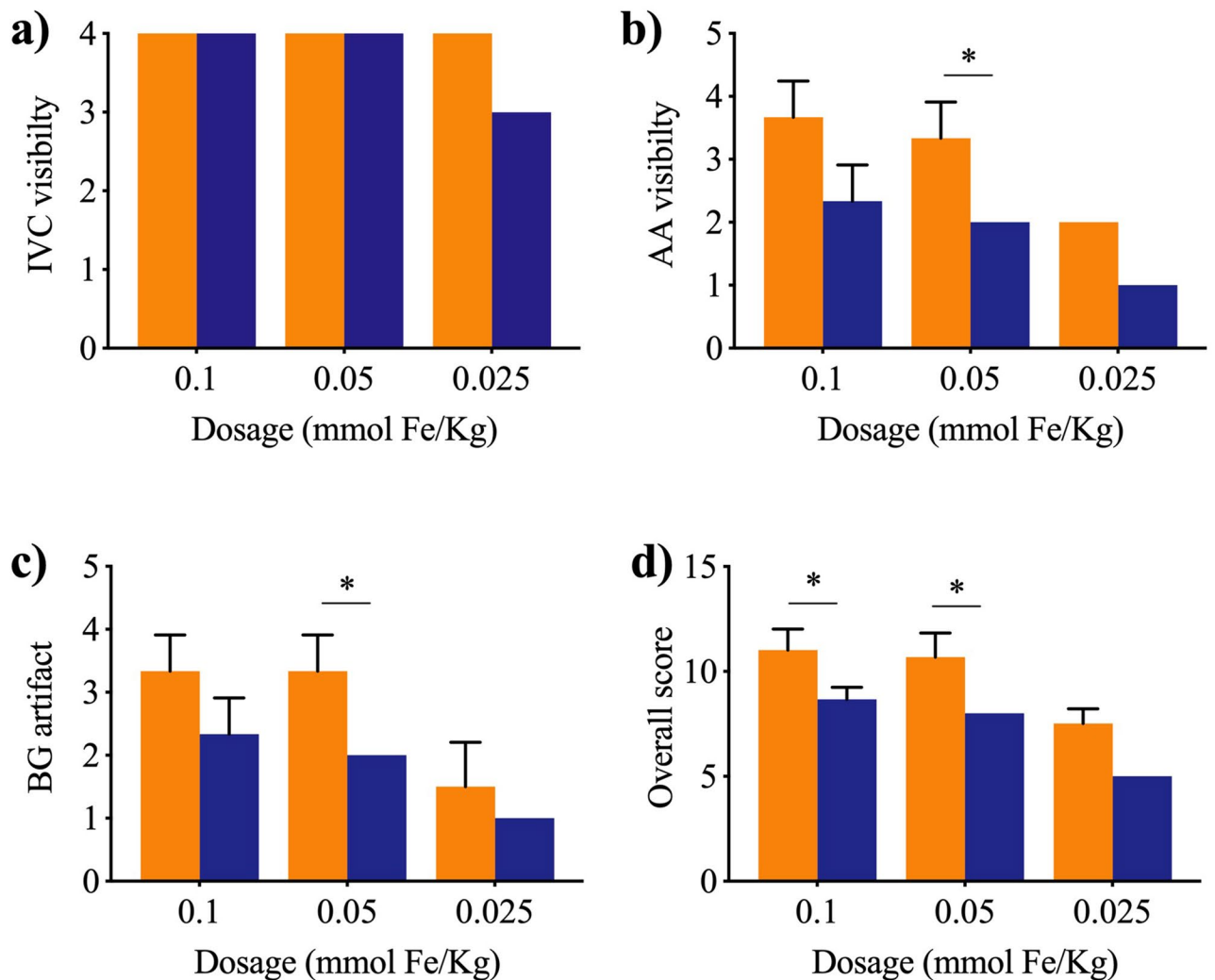


**Figure 3.** Mean VGAS as assessed on a 4-point scale at all dosages based on average score. MCP 3 (orange) and Resovist (purple). MPI images of MCP 3 show a higher VGAS in all image criteria, characterized by an overall higher image quality.  $n = 3$  for 0.1 and 0.05 mmol Fe/kg,  $n = 2$  for 0.025 mmol Fe/kg. Data were compared using one-tailed Mann–Whitney U test ( $*P \leq 0.05$ ).

former studies on in vivo vascular MPI with a spatial resolution in the millimeter range were performed with MNP dosages above the applied dosage in our study<sup>2</sup>. The newly developed MCP 3 indicates a better spatial resolution with at least 10-fold lower dosage applied, compared to conventional tracers used in angiographic system function (SF) based MPI studies (Resovist of 0.9 mmol Fe/kg<sup>22</sup>), and at least twofold lower dosage compared to the MPI-tailored MNP LS-008 (with approximately 0.15 mmol Fe/kg<sup>7</sup>) in mice. The applied dose is not far from the range of tolerable doses for MR clinical imaging with clinically approved iron oxide nanoparticles with maximum recommended Resovist doses of 0.45 mmol iron<sup>23</sup>. Moreover, in vitro studies have shown that submillimeter resolution is feasible by MPI-tailored MNP in conjunction with high-gradient amplitudes<sup>21,24</sup>. The development of MPI hardware and MPI-tailored MNP are necessary for further improvements of MPI towards clinical applications. However, hardware improvement is more challenging while optimization of MPI-tailored MNP could drastically reduce the costs of clinical MPI.

Furthermore, MCP 3-based MPI using relatively low tracer concentrations of 0.1 and 0.05 mmol Fe/kg allowed us to assess the arterial phase and to quantify aortic  $D_L$ . Hence, we conclude that quantification of vascular abnormalities such as stenosis or aneurysm with high temporal resolution combined with quantitative measurement of tracer concentration is achievable by MPI. Additionally, real-time monitoring of vital physiological signs (respiratory and cardiac) is possible from the information derived from raw MPI signal, which can be beneficial in cardiovascular imaging. For instance, the derived biosignal could be of value for respiratory motion compensation.

Our study has some limitations. To date, MPI is limited in spatial resolution leading to partial volume effects and possible under- or overestimation of  $D_L$ <sup>8</sup>. Additionally, the voxel dimension, independent of the spatial resolution of MNP, restrains the  $D_L$  measurement. Merely fractional amounts of signal in one neighboring voxel will result into significant deviation. The  $D_L$  measurement with MPI is relative. Similar to conventional

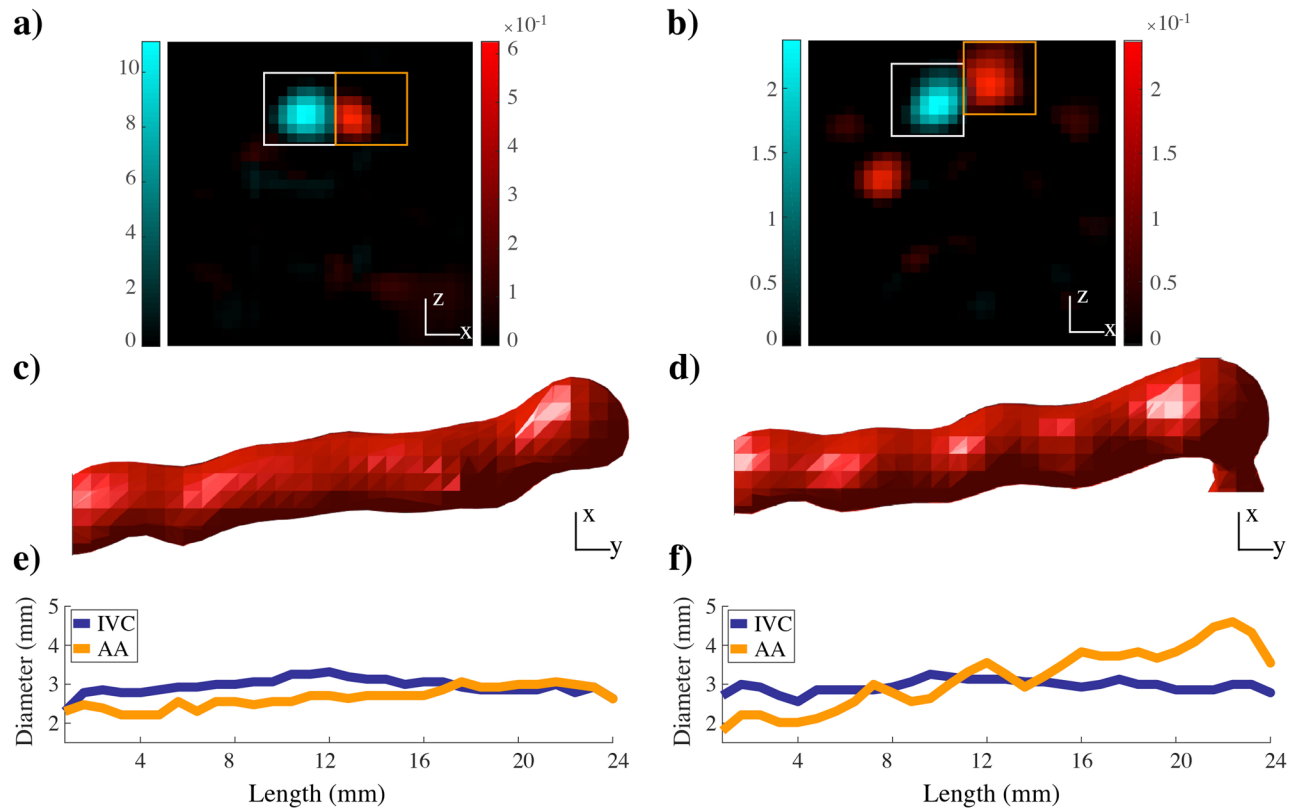


**Figure 4.** MPI digital subtraction angiography. Shown are the results for MCP 3 at 0.1 mmol Fe/kg in transverse (a) and coronal orientation (c) and the  $D_L$  (e) versus the corresponding results for 0.05 mmol Fe/kg (b, d, f). Mean  $D_L$  is in the range of 2–3 mm. The white square in A and B indicates the IVC VOI and the orange square the AA VOI. The arterial phase is isolated by subtraction of the IVC during the bolus passage through AA. The  $D_L$  of the AA and abdominal IVC along their longitudinal axes is determined. Color bar values in (a) and (b) are in  $\mu\text{g}$ .

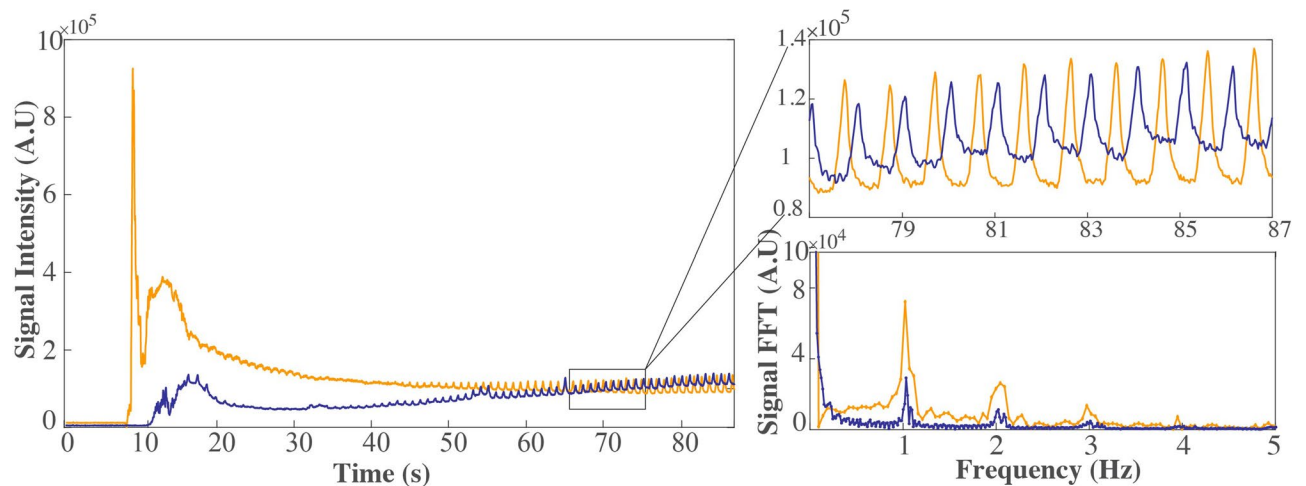


**Figure 5.** Biosignal derived from MPI signal. A signal component of the MPI measurement before background subtraction for both MNP—MCP 3 (orange) and Resovist (purple)—administered at a dose of 0.05 mmol Fe/kg. The modulation of the signal and the distinct peak in the Fourier transform of the signal correspond to a respiratory frequency of approximately 60 (breaths/minute).

CT-angiography, variations in reconstruction parameters can alter the  $D_L$  measurement. Standardized set of reconstruction parameters, based on previous phantom studies<sup>14</sup> were applied for all examinations to maintain results comparable and reliable. Nevertheless, the obtained values of AA  $D_L$  and IVC  $D_L$  are in good agreement with the literature<sup>25</sup>. In future work, we will use co-registration with MRI for a more accurate localization of the vessels and thus more precise  $D_L$  quantification. The choice of Resovist (containing the drug substance

Ferucarbotran) as a measure for comparison with MCP 3 is due to the frequent application of the tracer in MPI studies. Implementation of other commercially available tracers with promising MPI characteristics such as perimag<sup>26,27</sup> and synomag-D<sup>28</sup> (micromod Partikeltechnologie GmbH, Rostock, Germany) and comparison with the obtained results would be of interest in future studies.

Another general limitation in MPI based on SF is the possible mismatch of the SF-sample used for calibration and the magnetization dynamics of MNP under influence of their specific local environment in vivo<sup>29–32</sup>, which causes image artifacts and reduced sensitivity of MPI<sup>33</sup>. In a further step, we will investigate to which extent the adaptation of the SF e.g. adaptation of the temperature between system function measurement and in-vivo imaging can improve the image quality.

## Conclusion

Our study demonstrates the feasibility of MPI angiographic imaging with potential quantitative assessment of vascular anatomy in vivo, which has been made possible by advancements in scanner hardware and new, more refined MCP 3 tracers. Collectively, these developments improved tracking of the intravenously injected bolus in the IVC, detection and differentiation of the first pass in the AA in a quantitative manner, and visualization of the morphology of large abdominal vessels and their branches. Using MCP 3-MPI vessel lumens of  $2.7 \pm 0.6$  mm for IVC and  $2.4 \pm 0.7$  mm for AA became detectable with a clinically acceptable dose of 0.05 mmol Fe/kg. Our study opens a window into higher resolution MPI for preclinical and clinical research.

## Materials and methods

**Tracers.** Both tracers investigated and compared in this study are composed of magnetite/maghemite. They are synthesized by aqueous coprecipitation and have been proven biocompatible and biodegradable<sup>16,23</sup>.

MCP 3 was developed in-house as an MPI tracer coated with carboxymethyl dextran (CMD). The mean diameter of MCP cores is 32 nm (TEM) and the mean hydrodynamic diameter ( $D_H$ ) is 53 nm (DLS)<sup>14</sup>. The blood half-life of MCP in rats has been determined with MRI, 8.8 and 17.4 min at 0.05 and 0.1 mmol Fe/kg<sup>16</sup>.

Resovist (containing the drug substance Ferucarbotran), is an approved liver-specific MRI contrast agent (Schering AG, Berlin, Germany) that was taken off the market in Europe in 2008 but is still available in Japan (Fujifilm RI Pharma, Tokyo, Japan). It is coated with carboxydextran (CDX) and has a bimodal size distribution with mean core diameters of about 4 nm and 16 nm (TEM)<sup>34,35</sup>. The particles have a mean hydrodynamic diameter ( $D_H$ ) of 60 nm (DLS)<sup>36</sup> and has a blood half-life of 3.9–5.8 min in MRI<sup>18</sup> and less than 15 min in MPI<sup>7,15,17</sup>.

**Imaging hardware and image reconstruction.** Images were acquired in a preclinical 25/20 FF MPI scanner (Bruker Biospin/Philips, Germany) equipped with a separate receive-only gradiometer coil for increased sensitivity<sup>6</sup>. The acquisition was performed simultaneously with both the preinstalled coil and the separate receive coil. The 25/20 FF MPI scanner is a field-free-point (FFP)-based system and requires a SF calibration measurement (Supplement S3) for image reconstruction<sup>37,38</sup>. The nanoparticles were excited by drive fields of 12 mT in three orthogonal axes at three slightly different frequencies (2.5 MHz divided by 102/96/99 in x-/y-/z-direction). A selection gradient with a strength of 1.25 T/m/ $\mu_0$  in x- and y-axis and 2.5 T/m/ $\mu_0$  in z-axis is used for spatial encoding and generates the FFP. The FFP is moved along a 3D-Lissajous trajectory by the three drive fields and scans the field of view (FOV) of  $19.2 \times 19.2 \times 9.6$  mm<sup>3</sup> in 21.54 ms, resulting in 46 frames/s. The acquired data were reconstructed via the Kaczmarz algorithm with Tikhonov regularization in ParaVision 6 MPI software (Bruker Biospin, Ettlingen, Germany) to  $33 \times 33 \times 33$  voxels covering a volume of  $26.4 \times 26.4 \times 13.2$  mm<sup>3</sup> leading to an overscan of the FOV<sup>39</sup> to avoid artifacts at the borders. For further details of image reconstruction see supplement (Supplement S4).

**Image analysis.** Three-dimensional (3D) images were visualized and analyzed in MATLAB (2016a, Mathworks, Natick, MA, USA). For quantitative analysis, iron concentration–time curves were generated. A 3D VOI on the cross-section of the IVC and AA was defined, and mean signal in the VOI was determined throughout image acquisition. Digital subtraction of the IVC was performed in temporally separated images, a single frame during bolus passage in the IVC ( $t_1$ ) (Fig. 1), to separate arterial phase in the AA from the adjacent IVC in images.  $D_L$  of the IVC and AA were determined from separated vessels in images. To this end, vessel cross-sections were segmented in two-dimensional planes using basic intensity-based segmentation with a cutoff threshold of 30% maximum intensity<sup>14</sup>. The cross-sectional area was calculated as the sum of the number of all pixels in the segmented area multiplied by voxel size in transverse direction. Assuming the cross-section is circular in the transverse plane, the  $D_L$  was calculated from the area. The image quality was assessed using visual grading analysis (VGA) including visual grading analysis score (VGAS). The image criteria identified for a score scale are listed in Table 1. The overall score was defined as sum of all VGAS attributed to one examination. The statistical difference was analyzed by Mann–Whitney U-test using GraphPad Prism software version 7 (GraphPad Software, San Diego, CA, USA) and differences were considered significant for  $P \leq 0.05$ .

**Animal experiments.** All animal studies were approved by the State Office of Health and Social Affairs Berlin (LAGESO/A0409/12) and were carried out in accordance with institutional and federal animal care guidelines. Overall, 16 in vivo examinations were carried out on 8 healthy male Sprague Dawley rats (Charles River Laboratories, Sulzfeld, Germany), 7 weeks old and had an average body weight of  $259 \pm 19$  g. Prior to MPI scan, rats were anesthetized in an anaesthetic induction chamber with 5% isoflurane and maintained in 1–2% isoflurane during MPI acquisitions. Each rat was imaged twice, once with MCP 3 and once with Resovist. The order of MNP type administration was random. Identical doses of MCP 3 and Resovist were successively administered intravenously (Fig. 6) with sufficient time between the examinations for clearance of the MNP from the

Score Criterion	1	2	3	4
IVC visibility	Not visible	Poorly visible	Visible	Very well visible
AA visibility	Not visible	Poorly visible	Visible	Very well visible
Background (BG) artifact	Extensive artifact	Moderate artifact	Minimal artifact	No artifact

**Table 1.** The image quality criteria and the score scale defined to evaluate the quality of images. The image quality was graded visually. A higher score corresponds to better image quality and vice versa.

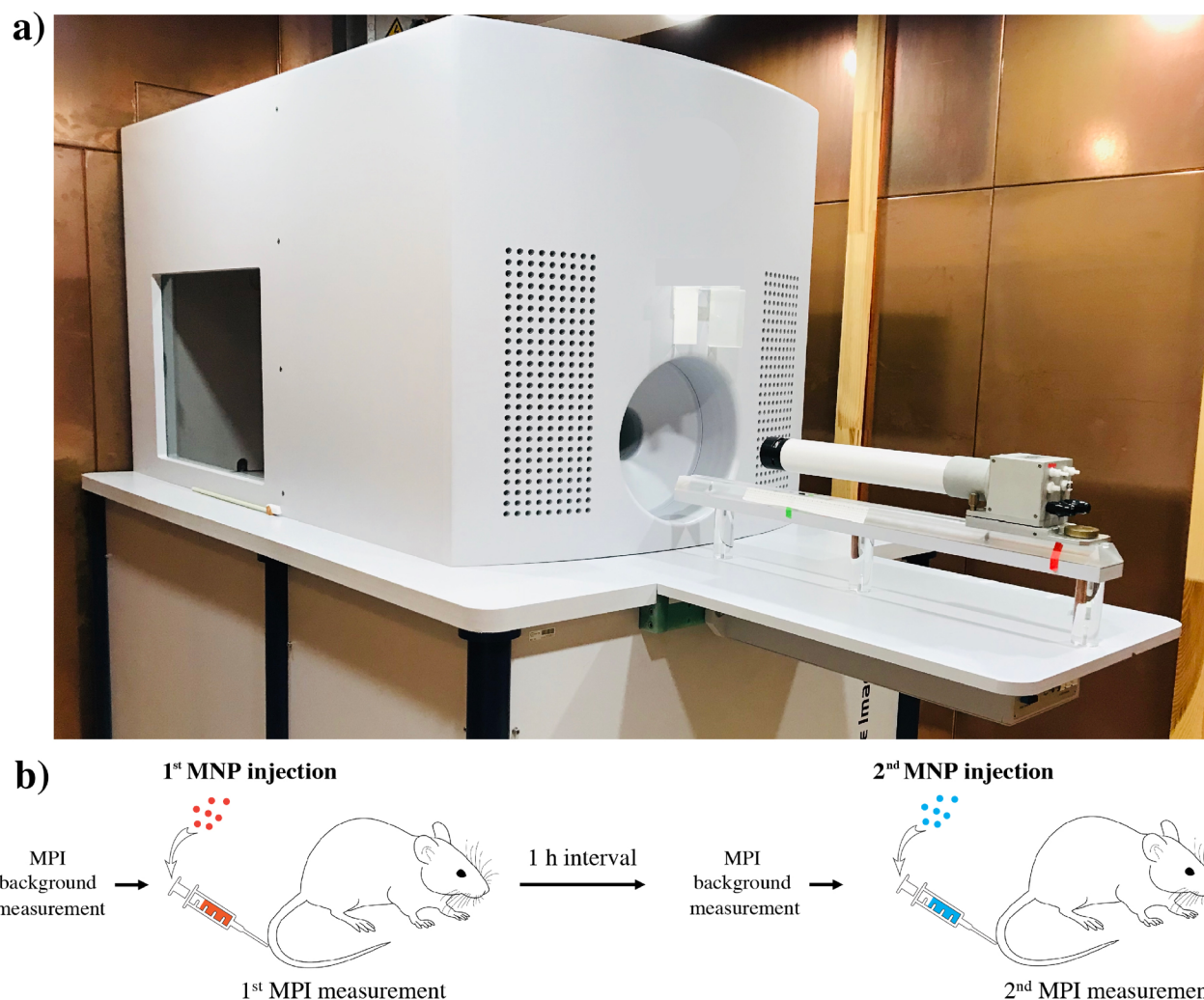


**Figure 6.** Preclinical MPI scanner (a) and diagram of experimental workflow (b). (a) Preclinical MPI scanner (MPI 25/20 FF, Bruker BioSpin) in a copper-shielded cabinet to suppress interferences from external electromagnetic fields. (b) Diagram of experimental workflow. First, background MPI signal is acquired, followed by IV injection of one of the MNP and MPI scanning for several minutes. After 1 h (no signals from MNP detectable in blood vessels), the second tracer, was injected intravenously. The order of MNP type administration was random.

blood (at least 1 h), when no signal modulation was detected prior to the MPI scans, as seen in raw data on the baseline signal (Fig. 5). The concentrations of the stock solutions were 145.5 mmol Fe/l for MCP 3 and 500 mmol Fe/l for Resovist, and the final administered doses were 0.025, 0.5, and 0.1 mmol Fe/kg of bodyweight. Final concentrations were prepared by diluting stock solutions with 7.5% mannitol. MPI acquisition, duration 2–5 min, started approximately 1 min before injection.

**Compliance with ethical standards.** All animal studies were approved by the State Office of Health and Social Affairs Berlin (LAGESO) and were carried out in accordance with institutional and federal animal care guidelines.

Received: 13 May 2020; Accepted: 28 September 2020

Published online: 14 October 2020

## References

- Gleich, B. & Weizenecker, J. Tomographic imaging using the nonlinear response of magnetic particles. *Nature* **435**, 1214–1217 (2005).
- Weizenecker, J., Gleich, B., Rahmer, J., Dahnke, H. & Borgert, J. Three-dimensional real-time in vivo magnetic particle imaging. *Phys. Med. Biol.* **54**, L1–L10 (2009).
- Khandhar, A. P. *et al.* Evaluation of PEG-coated iron oxide nanoparticles as blood pool tracers for preclinical magnetic particle imaging. *Nanoscale* **9**, 1299–1306 (2017).
- Vogel, P. *et al.* First in vivo traveling wave magnetic particle imaging of a beating mouse heart. *Phys. Med. Biol.* **61**, 6620–6634 (2016).
- Graeser, M. *et al.* Towards picogram detection of superparamagnetic iron-oxide particles using a gradiometric receive coil. *Sci. Rep.* **7**, 6872 (2017).
- Paysen, H. *et al.* Improved sensitivity and limit-of-detection using a receive-only coil in magnetic particle imaging. *Phys. Med. Biol.* **63**, 13NT02 (2018).
- Kaul, M. G. *et al.* In vitro and in vivo comparison of a tailored magnetic particle imaging blood pool tracer with Resovist. *Phys. Med. Biol.* **62**, 3454–3469 (2017).
- Vaalma, S. *et al.* Magnetic particle imaging (MPI): Experimental quantification of vascular stenosis using stationary stenosis phantoms. *PLoS ONE* **12**, e0168902 (2017).
- Herz, S. *et al.* Magnetic particle imaging for quantification of vascular stenoses: A phantom study. *IEEE Trans. Med. Imaging* **37**, 61–67 (2018).
- Sedlacik, J. *et al.* Magnetic particle imaging for high temporal resolution assessment of aneurysm hemodynamics. *PLoS ONE* **11**, e0160097 (2016).
- Franke, J. *et al.* MPI Flow analysis toolbox exploiting pulsed tracer information—An aneurysm phantom proof. *Int. J. Magnetic Particle Imaging* **3** (2017).
- Haegele, J. *et al.* Magnetic particle imaging: Visualization of instruments for cardiovascular intervention. *Radiology* **265**, 933–938 (2012).
- Salamon, J. *et al.* Magnetic particle/magnetic resonance imaging: In-vitro MPI-guided real time catheter tracking and 4D angioplasty using a road map and blood pool tracer approach. *PLoS ONE* **11**, e0156899 (2016).
- Kratz, H. *et al.* MPI phantom study with a high-performing multicore tracer made by coprecipitation. *Nanomaterials (Basel)* **9**, 1466 (2019).
- Haegele, J. *et al.* Magnetic particle imaging: Kinetics of the intravascular signal in vivo. *Int. J. Nanomed.* **9**, 4203–4209 (2014).
- Kratz, H. *et al.* Novel magnetic multicore nanoparticles designed for MPI and other biomedical applications: From synthesis to first in vivo studies. *PLoS ONE* **13**, e0190214 (2018).
- Keselman, P. *et al.* Tracking short-term biodistribution and long-term clearance of SPIO tracers in magnetic particle imaging. *Phys. Med. Biol.* **62**, 3440–3453 (2017).
- Hamm, B. *et al.* Contrast-enhanced MR imaging of liver and spleen: First experience in humans with a new superparamagnetic iron oxide. *J. Magn. Reson. Imaging* **4**, 659–668 (1994).
- Saritas, E. U. *et al.* Magnetic particle imaging (MPI) for NMR and MRI researchers. *J. Magn. Reson.* **229**, 116–126 (2013).
- Gleich, B. *Principles and Applications of Magnetic Particle Imaging*. 53 (Springer, New York, 2013).
- Arami, H. *et al.* Tomographic magnetic particle imaging of cancer targeted nanoparticles. *Nanoscale* **9**, 18723–18730 (2017).
- Kaul, M. G. *et al.* Combined preclinical magnetic particle imaging and magnetic resonance imaging: Initial results in mice. *Rofo* **187**, 347–352 (2015).
- Lawaczek, R. *et al.* Magnetic iron oxide particles coated with carboxydextran for parenteral administration and liver contrasting. Pre-clinical profile of SH U555A. *Acta Radiol.* **38**, 584–597 (1997).
- Vogel, P. *et al.* Micro-traveling wave magnetic particle imaging—Sub-millimeter resolution with optimized tracer LS-008. *IEEE Trans. Magn.* **55**, 1–7 (2019).
- Lanz, B., Poitry-Yamate, C. & Gruetter, R. Image-derived input function from the vena cava for 18F-FDG PET studies in rats and mice. *J. Nucl. Med.* **55**, 1380–1388 (2014).
- Tay, Z. W. *et al.* In vivo tracking and quantification of inhaled aerosol using magnetic particle imaging towards inhaled therapeutic monitoring. *Theranostics* **8**, 3676–3687 (2018).
- Eberbeck, D. *et al.* Multicore magnetic nanoparticles for magnetic particle imaging. *IEEE Trans. Magn.* **49**, 269–274 (2013).
- Bender, P. *et al.* Influence of clustering on the magnetic properties and hyperthermia performance of iron oxide nanoparticles. *Nanotechnology* **29**, 425705 (2018).
- Wells, J., Paysen, H., Kosch, O., Trahms, L. & Wiekhorst, F. Temperature dependence in magnetic particle imaging. *AIP Adv.* **8**, 056703 (2018).
- Loewa, N., Seidel, M., Radon, P. & Wiekhorst, F. Magnetic nanoparticles in different biological environments analyzed by magnetic particle spectroscopy. *J. Magn. Mater.* **427**, 133–138 (2017).
- Kosch, O., *et al.* Adaptation of a system function for in-vivo media. *IWMPI* (2018).
- Dieckhoff, J. *et al.* In vivo liver visualizations with magnetic particle imaging based on the calibration measurement approach. *Phys. Med. Biol.* **62**, 3470 (2017).
- Them, K. *et al.* Increasing the sensitivity for stem cell monitoring in system-function based magnetic particle imaging. *Phys. Med. Biol.* **61**, 3279–3290 (2016).
- Reimer, P. & Balzer, T. Ferucarbotran (Resovist): A new clinically approved RES-specific contrast agent for contrast-enhanced MRI of the liver: properties, clinical development, and applications. *Eur. Radiol.* **13**, 1266–1276 (2003).
- Eberbeck, D.W., F. Wagner, S. Trahms, L. How the size distribution of magnetic nanoparticles determines their magnetic particle imaging performance. *Appl. Phys. Lett.* **98**, 182502 (2011).
- Kratz, H., Eberbeck, D., Wagner, S., Taupitz, M. & Schnorr, J. Synthetic routes to magnetic nanoparticles for MPI. *Biomed. Tech. (Berl)* **58**, 509–515 (2013).
- Rahmer, J., Weizenecker, J., Gleich, B. & Borgert, J. Signal encoding in magnetic particle imaging: Properties of the system function. *BMC Med. Imaging* **9**, 4 (2009).
- Rahmer, J., Weizenecker, J., Gleich, B. & Borgert, J. Analysis of a 3-D system function measured for magnetic particle imaging. *IEEE Trans. Med. Imaging* **31**, 1289–1299 (2012).
- Weber, A., Werner, F., Weizenecker, J., Buzug, T. M. & Knopp, T. Artifact free reconstruction with the system matrix approach by overscanning the field-free-point trajectory in magnetic particle imaging. *Phys. Med. Biol.* **61**, 475–487 (2016).

## Acknowledgments

We are grateful for funding support from Deutsche Forschungsgemeinschaft (DFG, German Research Foundation): GRK 2260, BIOQIC-Biophysical Quantitative Imaging; DFG; grant number: 5943/31/41/91, and SFB 1340/1 2018, Matrix in Vision, grant number 372486779, projects A02 and C01.

## Author contributions

Conceptualization, A.M., H.K. and J.S.; methodology, A.M., H.K., J.S., R.H., N.S. and O.K.; software, A.M. and O.K.; validation, A.M., H.K., O.K., J.S. and F.W.; formal analysis, A.M., H.K. and O.K.; investigation, A.M., H.K., J.S., O.K. and N.S.; resources, R.H.; writing-original draft preparation, A.M.; writing-review and editing, H.K., O.K., F.W., I.S., M.T., and J.S.; visualization, A.M., H.K. and O.K.; supervision, J.S.; funding acquisition, M.T., I.S., B.H., and J.S.

## Funding

Open Access funding enabled and organized by Projekt DEAL.

## Competing interests

The authors declare no competing interests.

## Additional information

**Supplementary information** is available for this paper at <https://doi.org/10.1038/s41598-020-74151-4>.

**Correspondence** and requests for materials should be addressed to A.M.

**Reprints and permissions information** is available at [www.nature.com/reprints](http://www.nature.com/reprints).

**Publisher's note** Springer Nature remains neutral with regard to jurisdictional claims in published maps and institutional affiliations.



**Open Access** This article is licensed under a Creative Commons Attribution 4.0 International License, which permits use, sharing, adaptation, distribution and reproduction in any medium or format, as long as you give appropriate credit to the original author(s) and the source, provide a link to the Creative Commons licence, and indicate if changes were made. The images or other third party material in this article are included in the article's Creative Commons licence, unless indicated otherwise in a credit line to the material. If material is not included in the article's Creative Commons licence and your intended use is not permitted by statutory regulation or exceeds the permitted use, you will need to obtain permission directly from the copyright holder. To view a copy of this licence, visit <http://creativecommons.org/licenses/by/4.0/>.

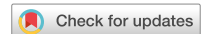
© The Author(s) 2020

# Publication C: Ex vivo magnetic particle imaging of vascular inflammation in abdominal aortic aneurysm in a murine model

Journal Data Filtered By: **Selected JCR Year: 2018** Selected Editions: SCIE,SSCI  
 Selected Categories: **"MULTIDISCIPLINARY SCIENCES"** Selected Category  
 Scheme: WoS

**Gesamtanzahl: 69 Journale**

Rank	Full Journal Title	Total Cites	Journal Impact Factor	Eigenfactor Score
1	NATURE	745,692	43.070	1.285010
2	SCIENCE	680,994	41.037	1.070190
3	National Science Review	1,842	13.222	0.006500
4	Science Advances	21,901	12.804	0.110010
5	Nature Communications	243,793	11.878	1.103290
6	Nature Human Behaviour	1,230	10.575	0.006550
7	PROCEEDINGS OF THE NATIONAL ACADEMY OF SCIENCES OF THE UNITED STATES OF AMERICA	661,118	9.580	1.022190
8	Science Bulletin	3,569	6.277	0.009840
9	Scientific Data	3,240	5.929	0.015610
10	Frontiers in Bioengineering and Biotechnology	1,994	5.122	0.006540
11	Journal of Advanced Research	2,691	5.045	0.004780
12	Research Synthesis Methods	1,932	5.043	0.005420
13	GigaScience	2,674	4.688	0.012510
14	Annals of the New York Academy of Sciences	46,385	4.295	0.025840
15	Scientific Reports	302,086	4.011	1.061540
16	Journal of the Royal Society Interface	12,933	3.224	0.029190
17	NPJ Microgravity	203	3.111	0.000670
18	PHILOSOPHICAL TRANSACTIONS OF THE ROYAL SOCIETY A-MATHEMATICAL PHYSICAL AND ENGINEERING SCIENCES	19,227	3.093	0.028200



OPEN

# Ex vivo magnetic particle imaging of vascular inflammation in abdominal aortic aneurysm in a murine model

Dilyana B. Mangarova<sup>1,2</sup>✉, Julia Brangsch<sup>1,3</sup>, Azadeh Mohtashamdolatshahi<sup>1</sup>, Olaf Kosch<sup>4</sup>, Hendrik Paysen<sup>4</sup>, Frank Wiekhorst<sup>4</sup>, Robert Klopffleisch<sup>2</sup>, Rebecca Buchholz<sup>6</sup>, Uwe Karst<sup>6</sup>, Matthias Taupitz<sup>1</sup>, Jörg Schnorr<sup>1</sup>, Bernd Hamm<sup>1</sup> & Marcus R. Makowski<sup>1,5</sup>

Abdominal aortic aneurysms (AAAs) are currently one of the leading causes of death in developed countries. Inflammation is crucial in the disease progression, having a substantial impact on various determinants in AAAs development. Magnetic particle imaging (MPI) is an innovative imaging modality, enabling the highly sensitive detection of magnetic nanoparticles (MNPs), suitable as surrogate marker for molecular targeting of vascular inflammation. For this study, Apolipoprotein E-deficient-mice underwent surgical implantation of osmotic minipumps with constant Angiotensin II infusion. After 3 and 4 weeks respectively, in-vivo-magnetic resonance imaging (MRI), ex-vivo-MPI and ex-vivo-magnetic particle spectroscopy (MPS) were performed. The results were validated by histological analysis, immunohistology and laser ablation-inductively coupled plasma-mass spectrometry. MR-angiography enabled the visualization of aneurysmal development and dilatation in the experimental group. A close correlation ( $R = 0.87$ ) with histological area assessment was measured. Ex-vivo-MPS revealed abundant iron deposits in AAA samples and ex-vivo histopathology measurements were in good agreement ( $R = 0.76$ ). Ex-vivo-MPI and MPS results correlated greatly ( $R = 0.99$ ). CD68-immunohistology stain and Perls'-Prussian-Blue-stain confirmed the colocalization of macrophages and MNPs. This study demonstrates the feasibility of ex-vivo-MPI for detecting inflammation in AAA. The quantitative ability for mapping MNPs establishes MPI as a promising tool for monitoring inflammatory progression in AAA in an experimental setting.

Cardiovascular diseases are currently one of the leading causes of death in the Western world. An abdominal aortic aneurysm (AAA) is defined as a weakening and dilatation of the abdominal aorta, prevailing in the infrarenal portion of the artery. The prevalence of AAA has been on the rise during the last decades as a result of demographic ageing, screening programs and improved clinical imaging techniques<sup>1</sup>. The main risk of undetected, asymptomatic aneurysms is progressive expansion, followed by rupture, hemorrhage and death in approximately 80% of the cases<sup>2</sup>. The development of AAA involves inflammation as a fundamental process. Chronic inflammation is characterized by the infiltration of inflammatory cell types, mainly macrophages and monocytes in the thrombus and throughout all layers of the aortic wall<sup>3</sup>. These cells release several proteolytic enzymes such as matrix metalloproteinases, cytokines and oxidation-derived free radicals, leading to vascular smooth muscle cell apoptosis and degradation of the aortic tunica media<sup>3</sup>. In AAA, elastolysis as a result of the

<sup>1</sup>Department of Radiology, Charité-Universitätsmedizin Berlin, Corporate Member of Freie Universität Berlin, Humboldt-Universität zu Berlin and Berlin Institute of Health, Charitéplatz 1, 10117 Berlin, Germany. <sup>2</sup>Department of Veterinary Medicine, Institute of Veterinary Pathology, Freie Universität Berlin, Robert-von-Ostertag-Str. 15, Building 12, 14163 Berlin, Germany. <sup>3</sup>Department of Veterinary Medicine, Institute of Animal Welfare, Animal Behavior and Laboratory Animal Science, Freie Universität Berlin, Königsweg 67, Building 21, 14163 Berlin, Germany. <sup>4</sup>Department 8.2-Biosignals, Physikalisch-Technische Bundesanstalt Berlin, Abbestrasse 2-12, 10587 Berlin, Germany. <sup>5</sup>Department of Diagnostic and Interventional Radiology, Technische Universität München, Ismaninger Str. 22, 81675 Munich, Germany. <sup>6</sup>Institute of Inorganic and Analytical Chemistry, Westfälische Wilhelms-Universität Münster, Corrensstr. 30, 48149 Münster, Germany. ✉email: dilyana.mangarova@charite.de

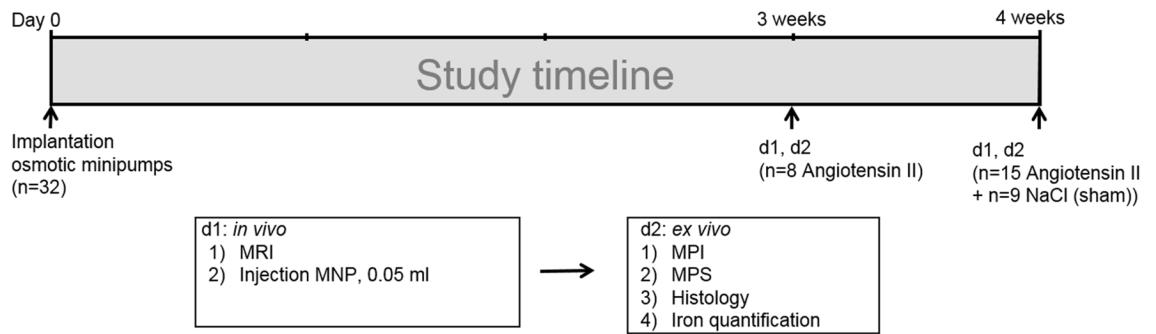


**Figure 1.** Experimental setup. Native in vivo MR imaging ( $N = 32$ ) was performed after three (group 1,  $n = 8$ ) and four weeks (group 2,  $n = 15$ ) of angiotensin II infusion. Following the scan, 50  $\mu$ l dose of macrophage-specific iron-oxide particles (ferucarbotran, 46.66  $\mu$ g iron per kg body weight) was administered via the tail vein. Ex vivo analysis (magnetic particle spectroscopy, magnetic particle imaging, histology, immunohistochemistry, laser ablation coupled to inductively coupled plasma-mass spectrometry) was performed 24 h after MNP administration. The control group consisted of apolipoprotein E-deficient mice ( $n = 9$ ) implanted with osmotic minipumps filled with sodium chloride, serving as the control group. *MPI* magnetic particle imaging, *MPS* magnetic particle spectroscopy, *MNP* magnetic nanoparticles.

chronic inflammation leads to reduced stability and consequently gradual dilatation of the aorta<sup>4</sup>. An increase in the inflammatory response and extracellular matrix (ECM) degradation results in an increased risk of rupture<sup>5</sup>.

Magnetic nanoparticles (MNPs) represent a molecular imaging probe type, mainly used for magnetic resonance imaging (MRI). MNPs are comprised of small iron oxide crystals, typically surface-modified by coating (polysaccharides, polyethylene glycol) or capping (organic acids). Their sensitivity to external magnetic fields and small size, ranging from 20 to 150 nm makes them ideal candidates for tracking tumor cells, drug delivery and detecting endothelial inflammation<sup>6,7</sup>. MNPs are internalized into macrophages/monocytes and represent a promising target for molecular imaging of inflammation and predicting aneurysm growth<sup>8–10</sup>. Ferucarbotran (RESOVIST) is a clinically approved MNP for MRI, designed for detecting liver lesions. It consists of magnetic nanoparticles (Magnetite- $\text{Fe}_3\text{O}_4$ /Maghemite- $\text{Fe}_2\text{O}_3$ ) coated with carboxydextran. Previous studies have proven ferucarbotrans efficiency for imaging AAA in clinical studies<sup>11</sup> as well as in animal models<sup>12</sup>. No adverse reactions are associated with rapid intravenous (i.v) injection of ferucarbotran<sup>13</sup>.

So far, there are several different approaches for detecting inflammation in AAA. 18F-fluorodeoxyglucose (FDG) is a radiopharmaceutical tracer for positron emission tomography (PET) and PET computed tomography (CT), targeting high-glucose-using cells including macrophages in aneurysm inflammatory sites, yet it relies on ionizing radiation<sup>14</sup>. In recent years, molecular MRI targeting macrophages and monocytes via various types of MNPs has gained momentum<sup>9</sup>. However, the detection of MNPs in MRI is highly dependent on the surrounding tissue and can be hard to distinguish from other sources (e.g. air, imaging artifacts or pathological tissue changes). Additionally, a reference scan before MNP injection is required to perform quantification.

Magnetic particle imaging (MPI) is a novel tomographic imaging modality for the highly sensitive detection and quantification of magnetic nanoparticles<sup>15</sup>. First described by Gleich and Weizenecker in 2005 MPI is currently used in preclinical studies and is not yet in clinical practice. Opposed to MRI, where MNPs cause signal void, MPI detects MNP tracers directly, causing positive contrast without any background signal from the surrounding tissue. MPI images are comparable to the images known from nuclear medicine imaging modalities such as PET and single-photon emission computed tomography (SPECT). Compared to MRI, MPI has a much higher sensitivity in detection of MNPs. MPI enables imaging and quantification of MNPs with higher specificity and without the need of additional measurements before injection of MNPs. MPI scanners have a spatial resolution in the millimeter range, which compares well with the resolution of clinical PET and SPECT. In contrast to PET or SPECT, MPI provides a much higher temporal resolution by using non-radiating tracers. Therefore, MPI makes a promising candidate for vascular imaging.

In this study, we assessed the potential of sensitive ex vivo MP imaging for the characterization of relevant parameters in AAA development and progression. A MPI-suitable MNP, ferucarbotran was used to evaluate the inflammatory processes in the aortic wall.

## Results

No side effects or adverse reactions to the imaging agents were observed in the investigated animals. In the control group, consisting of sham-operated mice ( $n = 9$ ) that received a continuous saline infusion for 28 days, AAA development was not observed. In the experimental group ( $n = 23$ ), the continuous infusion of angiotensin II (Ang II) via osmotic minipumps led to the formation of suprarenal aortic aneurysms (Figs. 1, 2). Animals developing no abdominal aneurysms were excluded from the study prior to data acquisition ( $n = 4$ ).

**MR angiography of abdominal aortic aneurysms.** Cross-sections of the abdominal aorta were assessed after 3 and 4 weeks of Ang II infusion (Fig. 1). The protocol included scans prior to administration of ferucarbotran. A significant aortic diameter increase was visible in T1 3D TOF ( $p < 0.05$ ) (Figs. 3, 4), while no

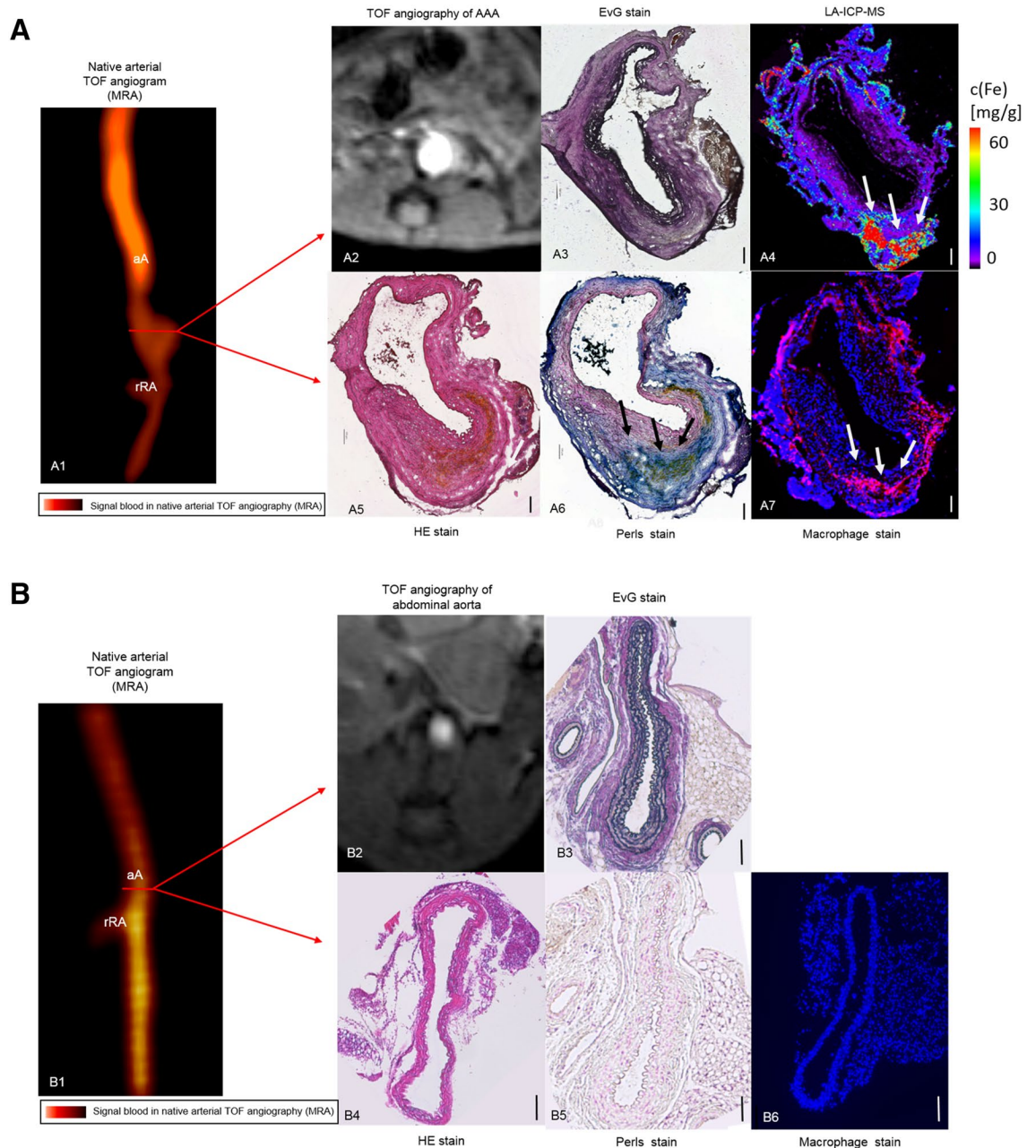


**Figure 2.** In vivo MRI of inflammatory activity during the development of aortic abdominal aneurysm compared to an animal from the control group. **(A1)** Time-of-flight angiogram showing the suprarenal abdominal aorta, including the right renal artery, of a male apolipoprotein E-deficient (Apo E  $-/-$ ) mouse after four weeks of angiotensin II (Ang II) infusion. **(A2)** A pronounced dilatation of the aortic lumen was observed on the T1 weighted sequence after 4 weeks of angiotensin infusion. **(A3–A7)** Ex vivo histological measurements using EvG **(A3)**, LA-ICP-MS **(A4)**, HE **(A5)**, Perls stain **(A6)** confirmed the in vivo findings. **(A4, A6, A7)** A strong correlation between the areas positive for iron-oxide particles in LA-ICP-MS **(A4)**, Perls' stain **(A6)** and immunofluorescence for macrophage accumulation **(A7)** in corresponding histological sections was observed. The scale bars represent 100  $\mu\text{m}$ . **(B1)** Time-of-flight angiogram showing the suprarenal abdominal aorta, including the right renal artery, of a male apolipoprotein E-deficient (Apo E  $-/-$ ) control group mouse after four weeks of sodium chloride solution infusion. **(B2)** No dilatation of the aortic lumen was observed on the T1 weighted sequence after 4 weeks of sodium chloride solution infusion. **(B3–B6)** Ex vivo histological measurements using EvG **(B3)**, HE **(B4)**, Perls' Prussian Blue **(B5)** and immunofluorescence for macrophage accumulation **(B6)** in corresponding histological sections revealed neither MNP accumulation nor AAA development. The scale bars represent 100  $\mu\text{m}$ . TOF arterial time of flight, aA suprarenal abdominal aorta, rRA right renal artery, MRA magnetic resonance angiography, HE hematoxylin–eosin-staining, EvG Miller's elastica van Gieson staining, LA-ICP-MS laser ablation coupled to inductively coupled plasma-mass spectrometry, MNP magnetic nanoparticles.

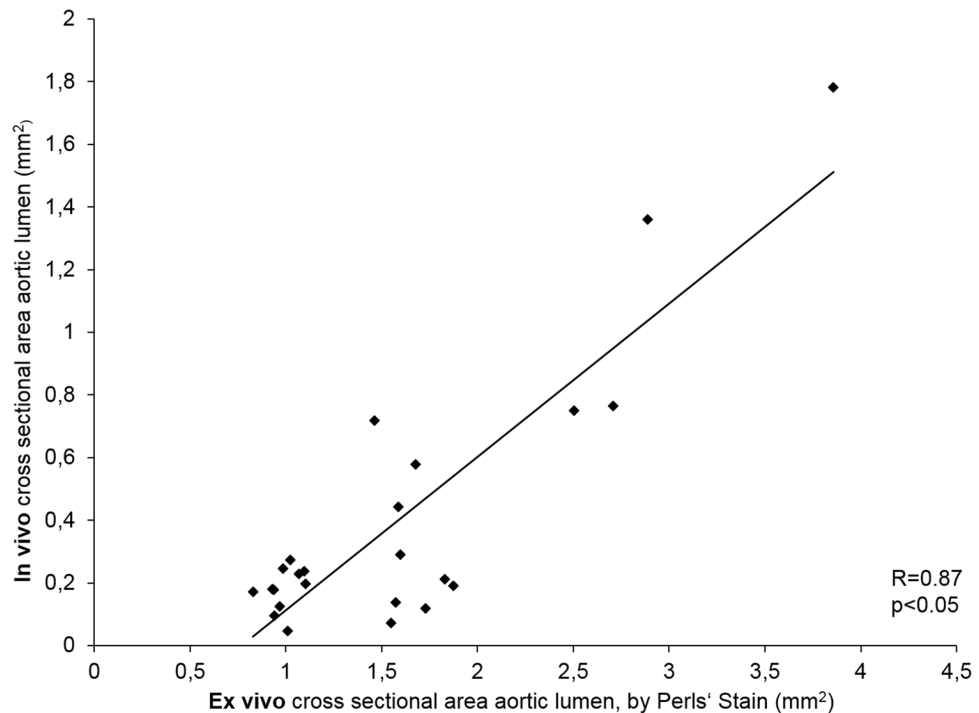


**Figure 3.** Correlation of in vivo MRI and ex vivo histological cross sectional AAA area measurements. To investigate the presence of AAA, in vivo MRI findings were compared to histological cross sections from the same region of the aorta. Time-of-flight angiogram detected the development of AAA in the experimental group. A strong correlation ( $R=0.87$ ) between the in vivo MRA and ex vivo histology images was shown. Overall, these measurements indicate an excellent agreement between in vivo and ex vivo measurements of the lumen dilatation in AAA. MRA magnetic resonance angiography.

difference was seen in the control animal group. The aortic diameter increased by 88% percent in the 3-week group and 175% in the 4-week group.

**Ex vivo magnetic particle imaging of AAA.** To evaluate the potential of MPI for measuring inflammatory response in AAA, ex vivo MPI images of the aorta were acquired 24 h after i.v. ferucarbotran administration. The AAAs with an overall iron content above  $0.3 \mu\text{g}$  were visible in MPI (Fig. 4A3). The reconstruction of images of ex vivo AAAs with low iron content was possible only with the immobilized MNP system function (SF). The decay of higher harmonics in freeze-dried ferucarbotran is rapid in comparison to the fluid sample. Hence, fewer frequency components were used in the reconstruction, which is not beneficial in sense of MPI resolution. However, the immobilized state of MNPs in the AAA after phagocytosis by macrophages<sup>16</sup> resembles more the immobilized state of MNPs in sugar matrix of mannitol SF and results in a more reliable reconstruction. The magnetic particle spectroscopy (MPS) quantification results are in good agreement and validate the MPI iron mass quantification ( $R=0.99$ ) (Fig. 5). The average deviation of total iron amount determined by MPI from MPS is 8.3% for samples above  $1 \mu\text{g}$  and 20.6% for samples below  $1 \mu\text{g}$  and 15.2% overall. The slight over- or underestimation of iron amount in comparison to MPS results might arise from partial volume effects due to the limited resolution of MPI and low signal-to-noise ratio (SNR).

**Histological analysis.** Elastica van Gieson (EvG) stained histological sections revealed strong extracellular matrix remodeling, visible in the 3 weeks- as well as in the 4 weeks Ang II infusion groups (Fig. 2A3). Degradation of elastic fibers and following dilatation of the aortic lumen was accompanied by the formation of a thrombus. On the other hand, elastogenesis characterized by a higher amount of elastic fibers in the areas adjacent to the vascular lumen was observed, indicating a repair process in late stage aneurysm. The Perls' Prussian blue stained histopathologic sections revealed abundant iron within AAA, while no or little iron was detected in the control group (Fig. 2A6). Anti-CD68 monoclonal antibody immunohistology analysis revealed abundant macrophage accumulation in the adventitial area of the aneurysm (Fig. 2A7).

**Correlation of magnetic particle spectroscopy, magnetic particle imaging, histology and immunohistochemistry.** MPS functions as a zero-dimensional MPI with higher sensitivity. The accumulation of iron in the AAAs was measured with MPS and results were used for validation of the MPI quantification.

Ex vivo MPI and MPS measurements revealed abundant iron within AAAs (Figs. 4, 5), while no or little iron was detected in the control group (Fig. 2B5).

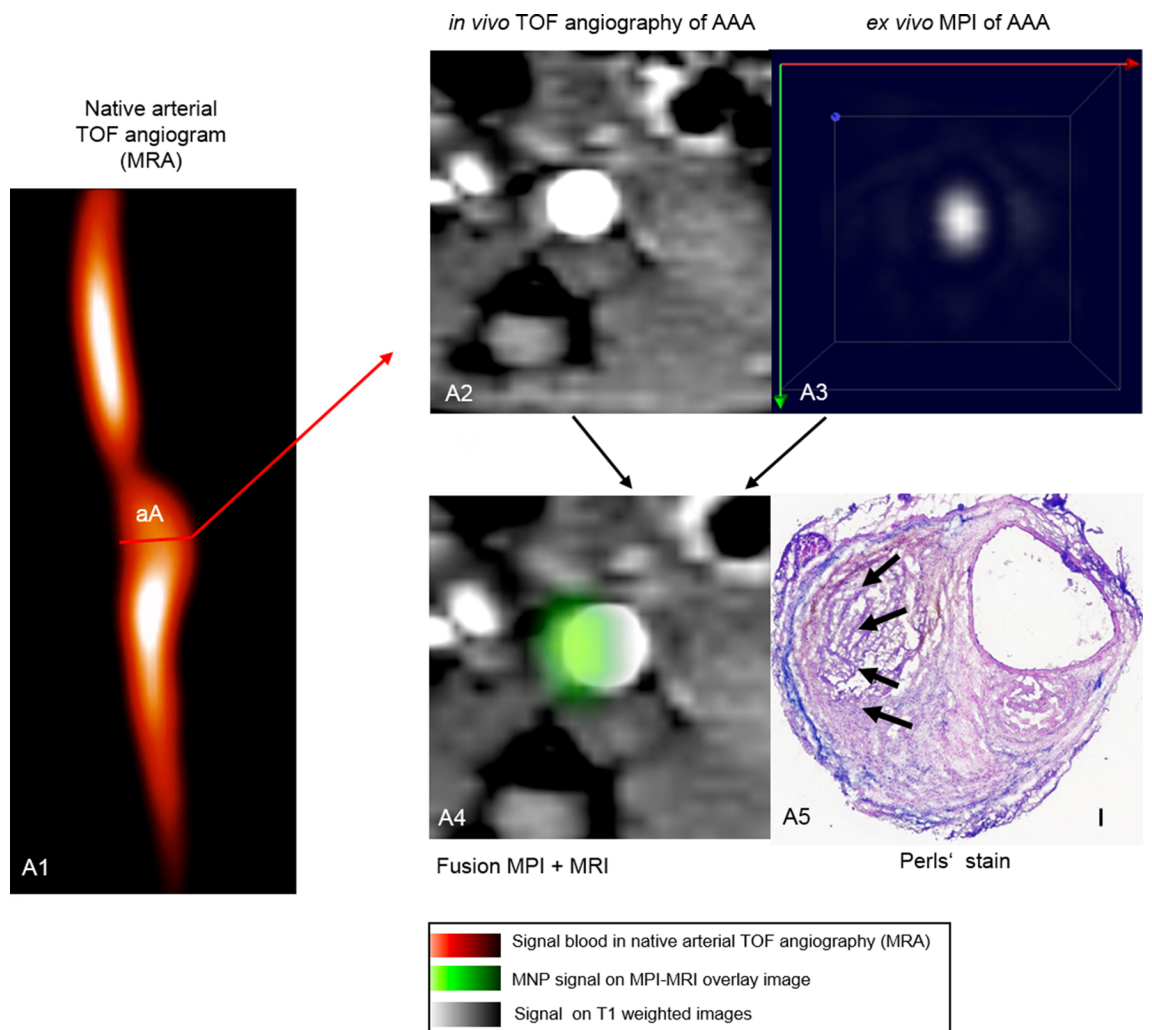


**Figure 4.** In vivo MRI and ex vivo MPI of inflammatory-activity during the development of aortic abdominal aneurysm. (A1) Time-of-flight angiogram showing the supraceliac abdominal aorta of a male apolipoprotein E-deficient (Apo E  $-/-$ ) mouse after four weeks of angiotensin II (Ang II) infusion; (A2): a pronounced dilatation of the aortic lumen was observed on the T1 weighted sequence after 4 weeks of angiotensin infusion; (A3) ex vivo MPI of the AAA region of the same mouse; (A4): ex vivo aortic MPI—in vivo whole body MRI signal manual fusion overlay based on anatomical landmarks; (A5) Perls' Prussian Blue; the scale bar represents 100  $\mu$ m. *TOF* arterial time of flight. *aA* supraceliac abdominal aorta, *MRA* magnetic resonance angiography, *MNP* magnetic nanoparticles.

A strong correlation was found between the areas positive for CD68 immunohistology stain and Perls' Prussian blue stain (Figs. 2A6, A7), confirming the co-localization of macrophages and MNPs. There is a positive correlation between the amount of iron measured in Perls' Prussian Blue and ex vivo MPS as well as ex vivo MPI (Figs. 5, 6) iron quantification. The MPS quantification of the intact harvested AAA verified that the stained iron in the sections does not originate from endogenous iron nor from cutting blades during tissue processing.

#### Elemental bioimaging by means of laser ablation-inductively coupled plasma-mass spectrometry for spatial localization of iron.

To determine the spatial distribution of MNPs within the aneurysmal wall, laser ablation inductively coupled plasma mass spectrometry (LA-ICP-MS) measurements were performed in two mice after 4 weeks of Ang II infusion. A pronounced colocalization of iron, macrophages (CD68) and Perls' Prussian blue positive areas was found (Fig. 2A4, A6, A7).

#### Discussion

This study demonstrates the feasibility of ferucarbotran-enhanced ex vivo MPI for the detection of vascular inflammation in AAA. Ex vivo iron measurements via LA-ICP-MS, immunohistology, histopathology, MPI and MPS demonstrated a strong correlation, thus confirming the inflammatory activity and resulting MNP accumulation in the aneurysmal wall.

Inflammation is a key process in the emergence and development of many pathological conditions such as vascular disease, cancer, immune and neurologic disorders. Tracking inflammatory processes usually involves

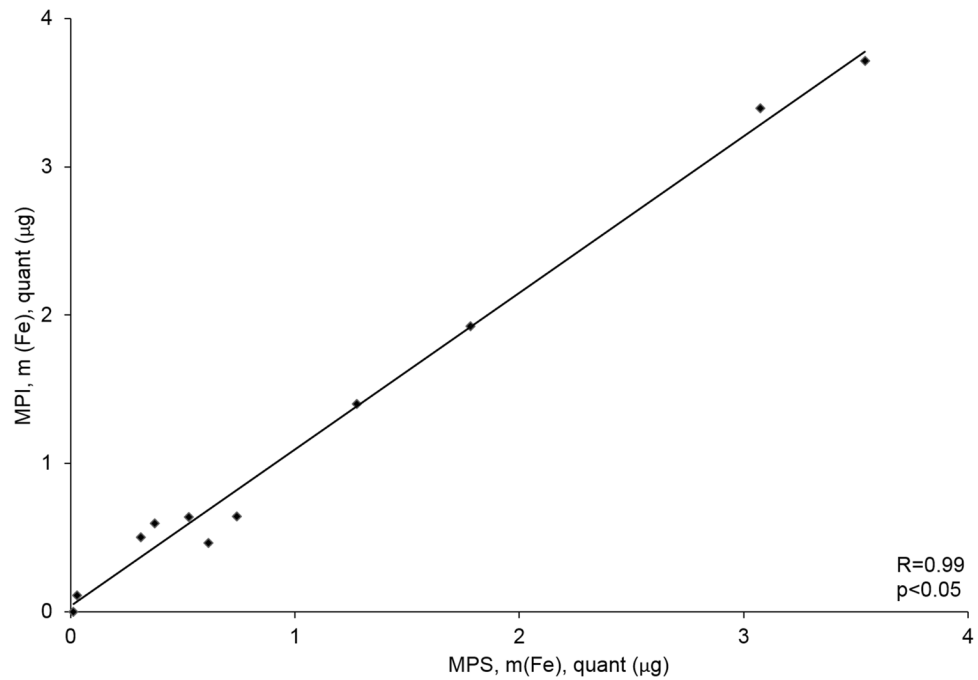


**Figure 5.** Correlation of ex vivo MPS and MPI iron oxide particle measurements. MPS is a standard method for validation of MPI results, combining static and dynamic magnetic properties of iron oxide nanoparticles. A strong correlation ( $R=0.99$ ) between the amount of iron-oxide particles measured in ex vivo MPS and ex vivo MPI was measured. *MPS* magnetic particle spectroscopy, *MPI* magnetic particle imaging.

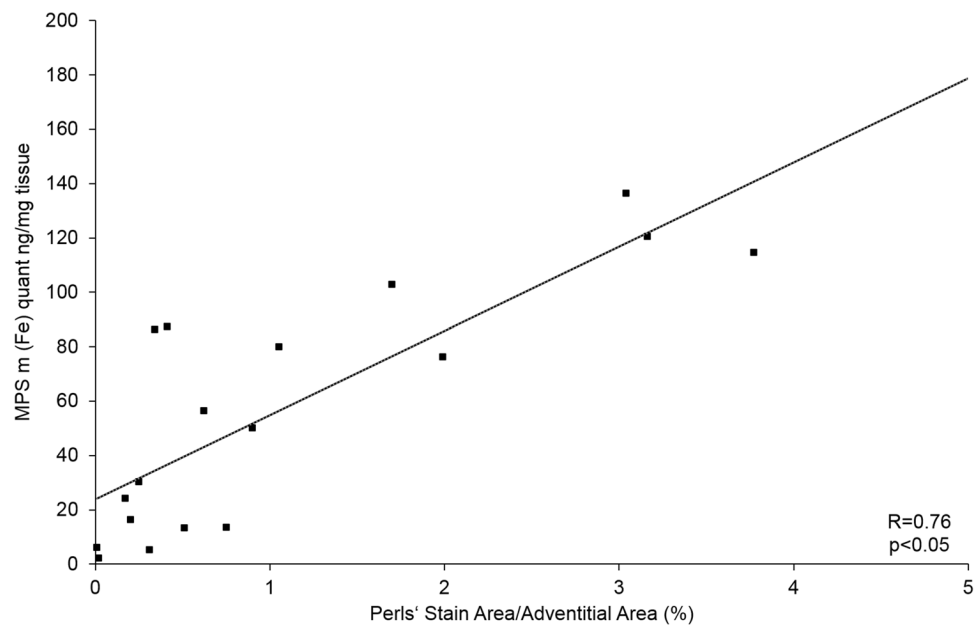


**Figure 6.** Correlation of MPS iron oxide particle measurements and Perls' Prussian Blue stained histological measurements. In order to investigate the absolute amount of iron oxide particles in AAA samples, ex vivo MPS measurements were performed prior to histological processing. A strong correlation between the amount of iron-oxide particles measured in ex vivo MPS and Perls' Prussian Blue staining was shown. The combined assessment of both analytical methods verify the feasibility of MPS for detection of inflammation sites in AAA. *MPS* magnetic particle spectroscopy.

low specificity biomedical imaging or invasive methods such as biopsies<sup>17</sup>. Previous research on inflammation detection has tended to focus on MR imaging, demonstrating the MNP uptake at inflammation sites<sup>18,19</sup>. A major disadvantage of this method is that iron oxide nanoparticles cause a signal intensity decrease in MRI, which could easily be missed or mistaken for an artifact<sup>17</sup>. MPI allows the detection of inflammation through MNPs with a higher specificity and SNR.

Ferucarbotran is currently considered the standard MPI agent due to its commercial availability and excellent signal properties<sup>20,21</sup>. Uptake of MNPs in AAAs has previously been investigated<sup>22</sup> and imaged with MRI in murine model as well as in human patients<sup>10,16,23</sup>. It has been demonstrated that MNP-enhanced MRI could identify aortic wall inflammation in patients with AAAs and predicts the rate of aneurysm growth and clinical outcome<sup>10,22</sup>. In a clinical study, the growth rate of AAA of patients correlated significantly with amount of MNP in the aneurysmal wall, despite comparable aneurysm diameters<sup>10</sup>.

Further experimental investigations should focus on enhancing the quality of angiographic and vascular MPI. MNPs are administered mostly i.v., allowing the direct visualization of the blood flow<sup>24</sup>. The first dynamic MPI-static MRI imaging sequence of a beating mouse heart was acquired in 2009<sup>25</sup>. Since most MPI scanners have no tissue depth limitation, imaging the whole cardiovascular system without signal attenuation in a similar manner is theoretically possible<sup>24</sup>. Regarding AAA, so far only hemodynamic aneurysm phantom experiments have been conducted, paving the way for in vivo MPI AAA imaging in the future. Once MNPs are administered i.v., there is a very limited imaging time frame before the particles escape the cardiovascular system and start accumulating in the spleen and liver<sup>26,27</sup>. However, for many diseases models, including AAA a prolonged blood circulation time would be beneficial. Ferumoxytol for example, an ultrasmall superparamagnetic iron oxide (USPIO) circulates longer<sup>28</sup>, avoiding uptake by Kupffer cells in the liver and also reducing the chances for shadowing effect in MPI<sup>29</sup>. The prolonged circulation is favorable for access to the AAA site and uptake by macrophages. Future studies should target identifying further, suitable, high resolution MPI tracer. Furthermore, we should also consider the application of MPI for AAA rupture prediction. In a MRI study by Brangsch et al. in a murine AAA model, the prediction of aneurysm rupture with an iron oxide based contrast agent was associated with a sensitivity of 80% and specificity of 89%. It is a question of future research to investigate whether these results are also applicable to MPI.

Although the pathophysiology of AAA is not completely deciphered, it is a well-known fact that both inflammatory activity, characterized by a pronounced proinflammatory cell infiltration, as well as ECM degradation, defined by breakdown of cross-linked elastin and collagen are key<sup>16</sup>. While those two mechanisms appear to be autonomous, the formation of AAA is most likely when they co-occur.

Inflammatory activity is an excellent in vivo indicator for the characterization of AAAs. Previous studies from the past years have showcased the potential of MNPs for imaging macrophage activity in AAAs<sup>10,23,30,31</sup>. There are two different types of macrophages, namely M1 and M2<sup>32</sup>. While M1 macrophages are associated with proinflammatory cytokines, classically activated by interferon  $\gamma$  (IFN- $\gamma$ ) or lipopolysaccharides (LPS) from viral and bacterial pathogens, M2 macrophages are responsible for tissue repair and wound healing, inducing collagen production<sup>33</sup>. AAAs are marked by a high M1:M2 cell ratio<sup>34</sup>, suggesting that various inflammatory cytokines secreted by M1 macrophages such as migration inhibitory factor (MIF-1) and tumor necrosis factor (TNF) in addition to matrix metalloproteinases (MMP-9) are responsible for the degradation of ECM proteins in the vessel wall, causing continuous dilatation of the aortic lumen<sup>35,36</sup>. In this study, we could detect and quantify the macrophage activity in AAA through several different ex vivo methods. Future work should concentrate on targeting the long-term quantification of inflammatory activity at multiple stages of the AAA development through MPI.

This study has two primary limitations. First, the strong shadowing effect<sup>29</sup> observed in ferucarbotran-enhanced MPI is responsible for the absence of in vivo MPI in our experiment. When two objects with a large difference in iron concentration simultaneously present in the field of view, the object with lower iron content is suppressed and thus not visible<sup>37</sup>. This is the case with the abdominal portion of the aorta in vicinity of the liver, where ferucarbotran is mainly sequestered by the reticuloendothelial system of the body.

Second, since no topological anatomical information is obtained from the MPI scans, a reference image is required from another imaging modality such as CT or MRI for accurate localization of the imaging area. Co-registration via fiducial markers<sup>38</sup> is an option, however the transferring of animals from the MPI scanner to the other modality might cause spatial confidence issues and requires image post-processing. An integrated hybrid system combining MPI and MRI will assure spatial co-registration accuracy. A MPI/MRI Hybrid imaging system has been realized successfully, yet only used for static images and 2D phantom measurements<sup>39,40</sup>.

## Conclusion

To our knowledge, this is the first study that demonstrates the potential of a combined in vivo MR—ex vivo MP imaging for the assessment of inflammatory response in the aneurysmal wall of an Ang II-infused ApoE<sup>-/-</sup> mouse model using the MNP ferucarbotran. Future research could examine the feasibility of a combined MR-MP imaging in order to improve the in vivo characterization of AAAs.

## Methods

**Animal experiments.** The animal experiments were approved and performed according to the local Guidelines and Provisions for Implementation of the Animal Welfare Act by Charite Universitaetsmedizin Berlin, the regulations of the Federation of Laboratory Animal Science Associations (FELASA) and the local animal protection committee of the LaGeSo, Berlin, Germany.

All procedures in this study were conducted by a veterinarian, and all possible steps were taken to avoid suffering at each stage of the experiment. The animals were fed with a standard lab diet and housed in a clean barrier. For surgery and for the imaging sessions, mice were anesthetized with an intraperitoneal (i.p.) combined

injection of 500 µg/kg medetomidin, 50 µg/kg fentanyl, and 5 mg/kg midazolam. In order to accelerate recovery time, anesthesia was antagonized using an i.p. combination of Atipamezole (2.5 mg/kg), Naloxone (1,200 µg/kg), Flumazenil (500 µg/kg) following MRI imaging. AAAs were induced in 23 male, Apolipoprotein E deficient mice (B6.129P2-ApoE<sup>tm1Unc/J</sup>) mice (8 weeks old). Osmotic minipumps (Alzet model 2004, Durect Corp) were implanted subcutaneously in the dorsal neck area. Angiotensin II was continuously infused with a rate of 1,000 ng/kg/min for 3 weeks (group 1, n = 8) or 4 weeks (group 2, n = 15), respectively. Sham-operated ApoE<sup>-/-</sup> mice (n = 9) delivered saline over 4 weeks serving as the control group.

In order to verify the development of AAA, native MR imaging was performed after 3 weeks (group 1) or 4 weeks (group 2 and control group), followed by i.v. injection of ferucarbotran to the tail vein (50 µl ferucarbotran, 46.66 µg iron per kg body weight). 24 h later, animals were sacrificed and the abdominal part of the aorta was harvested in order to correlate the in vivo MRI findings with ex vivo data (MPI, MPS, histology, immunohistochemistry and LA-ICP-MS).

**Magnetic nanoparticles.** Ferucarbotran (RESOVIST, From Pharmaceutical Co Ltd, Tokyo, Japan) is the second clinically approved MNP developed for contrast-enhanced MRI of the liver. It is a hydrophilic colloidal solution of  $\gamma$ -Fe<sub>2</sub>O<sub>3</sub> coated with carboxydextran, composed of clusters of single-domain nanoparticles. Ferucarbotran has a bimodal size distribution with mean core diameters of about 4 nm and 16 nm (electron microscopy)<sup>13,20</sup> and shows a mean hydrodynamic diameter ( $D_H$ ) of 60 nm (photon correlation spectroscopy)<sup>41</sup>. The carboxydextran coating (27–35 mg/ml with an iron to carboxydextran ratio of 1:1 (w/w)) ensures aqueous solubility of the microparticles and prevents aggregation. Ferucarbotran contains 0.5 mol Fe/l, including 40 mg/ml mannitol and 2 mg/ml of lactic acid, adjusted to a pH of 6.5. At 37 °C, the solution has an osmolality of 0.319 osmol/kg H<sub>2</sub>O and a viscosity of 1,031 MPas. Upon i.v. application, ferucarbotran is taken up by the reticuloendothelial system (RES), mostly in the liver (80%) and spleen (8–9%). Following uptake in RES cells, the carboxydextran coating decomposes and the iron is conveyed to the iron pool via transferrin<sup>42</sup>.

### In vivo magnetic resonance imaging

Mice were imaged in supine position after induction of anesthesia. Using a clinically approved single loop coil (47 mm Siemens Healthcare Solutions, Erlangen, Germany), the imaging sessions were performed on a clinical 3 T Siemens system (Biograph-mMR, Siemens Healthcare Solutions, Erlangen, Germany). Body temperature (37 °C) was monitored using a MR-compatible heating system (Model 1025, SA Instruments Inc, Stony Brook, NY). In conclusion to the acquisition of native scans, ferucarbotran was administered via a 30G cannula attached to a small diameter tube inserted into the tail vein of the animals.

A non-contrast-enhanced two-dimensional time-of-flight angiography (2D TOF) following a three-dimensional (3D) gradient echo scout scan was performed in transverse orientation for visualization of the abdominal aorta. Following parameters were used: field of view (FOV) of 200 × 200 mm, matrix of 960 × 960, resolution of 0.2 × 0.2 × 0.5 mm, 40 slices, repetition time (TR)/echo time (TE) of 35 ms/4.44 ms, flip angle of 90°, and bandwidth of 124 Hz/Px. To obtain an arterial angiogram of the abdominal aorta for planning the subsequent MR angiography, a maximum intensity projection (MIP) was automatically produced.

**Ex vivo magnetic particle imaging.** Ex vivo MP imaging of the aorta was performed 24 h post-i.v. administration of 50 µl ferucarbotran after 3 (group 1, n = 8) respectively 4 (group 2, n = 15) weeks of Ang II perfusion. MPI images were acquired on a commercial preclinical MPI system (Bruker MPI 25/20 FF), equipped with a separate gradiometric receive coil<sup>43,44</sup> for improved sensitivity and image quality.

This field-free-point (FFP) based MPI system requires a pre-recorded (SF) for image reconstruction<sup>45,46</sup>. The SPIONs inside the FOV are excited with three drive fields at amplitudes of 12 mT, orthogonal to one another, operating at slightly different excitation frequencies (2.5 MHz divided by 102/96/99 in x-/y-/z-direction) to generate the Lissajous trajectory of the FFP movement in a selection field gradient at strength of 2.5 T/m in z-direction, and 1.25 T/m in x and y direction. The FFP scans the FOV along this Lissajous trajectory. In this matter the FOV is scanned into a 3D image of the MNP distribution at a temporal resolution of 21.5 ms.

**Magnetic particle imaging system function.** The SF was measured for ferucarbotran in two forms: one in an aqueous suspension and one in a freeze-dried mannitol sugar matrix. Both SF samples, the aqueous suspension SF sample and the immobilized SF sample (in mannitol sugar matrix)<sup>47</sup> had an iron concentration (c(Fe)) of 100 mM and volume of 13.5 µl. The immobilized SF sample was prepared with a mannitol solution (10% w/v). The SF sample was measured in a container with dimension of 3 × 3 × 1.5 mm<sup>3</sup> in a cuboid shape. The measurement grid had a size of 25 × 25 × 13 in FOV of size 25 × 25 × 13 mm<sup>3</sup> leading to an overscan of the physical FOV of 19.2 × 19.2 × 9.6 mm<sup>3</sup><sup>48</sup>. The SF measurements were acquired with the same aforementioned drive and gradient fields for image acquisition.

**Image reconstruction and analysis by magnetic particle imaging.** The images were reconstructed to 25 × 25 × 13 voxels via Kaczmarz's algorithm with Tikhonov regularization in ParaVision 6 MPI software (Bruker Biospin, Ettlingen, Germany). The hardware background noise limits the used frequency components to a bandwidth to 0.09–125 MHz so the 3rd harmonic is as well filtered out. A number of 487 frequency components were chosen automatically according to the applied SF and the SNR (SNR = 7) threshold determined from the SF. Frequency components with a mixing order above 25 were removed from the further analysis. For reconstruction, a block average of 20 repetitions was applied to the measurement to reduce visible noise in the images. A regularization of  $\lambda = 10^{-149}$  and five iterations were performed for the final reconstructions. These

parameters were kept constant in all reconstructions to exclude the influence of variations in these parameters on the intensity values.

For quantification of iron mass in ex vivo MPI images, they were analysed in MATLAB (Mathworks, Natick, MA, USA). First a 50% cut-off threshold of maximum voxel intensity value was applied to the 3D dataset; to eliminate background noise and artefacts, and to minimize the effect of image blurring due to the regularization in image reconstruction<sup>44</sup>. Thereafter the calculation of iron mass in AAA was performed by integration of overall iron in volume of interest (VOI) over the AAA.

**Quantification by magnetic particle spectroscopy.** Ex vivo MPS measurements of harvested abdominal aortas (n = 32) were performed using a commercial magnetic particle spectrometer (Bruker, Germany) with a sinusoidal magnetic signal excitation using an amplitude of 25 mT, a frequency of 25 kHz and a sample temperature of 37 °C. The nonlinear magnetization response of MNPs in AAA was measured for 10 s by a pickup coil (sensitivity:  $10^{-12}$  A m<sup>2</sup>). For accurate MPS iron mass quantification, the reference was chosen according to the harmonic ratio A5/A3 of measured sample, immobilized (freeze-dried in 10% mannitol) or in water dispersion and the background signal of the empty sample holder was subtracted from the MPS spectra. For quantitation, the amplitude of the 3rd harmonic of the MPS spectra of measured samples was normalized to the amplitude of the known reference sample.

**Histological analysis of aortic aneurysms and aortic aneurysm morphometry.** Histological analysis was performed in the same region of the aorta that was imaged in MRI and MPI. Aortic aneurysm samples were divided in half for paraffin- and cryosectioning, tissues were either processed overnight in MorFF-Fix (MORPHISTO, Frankfurt am Main, Germany) or frozen at -20° C. 9 µm thick sections of the vessels were stained with Perls' Prussian Blue staining, Miller's Elastica van Gieson staining, Hematoxylin and Eosin staining. Resulting histological slices were scanned and photographed using a light microscope (Keyence BZ-X800, Keyence Corporation of America, USA). The morphometrical analysis of the aortic region was performed using Keyence BZ-X800 Analyzer software (Keyence BZ-X800, Keyence Corporation of America, USA). To measure the iron oxide percentage in the tissue in a single digitized image, the color profile of iron oxide as seen using Perls' Prussian Blue was set as reference. All structures within this specific color profile were automatically recorded and divided by the overall tissue area in order to acquire the iron oxide ratio.

**Immunofluorescence analysis.** Immunofluorescence staining was performed to assess the localization of macrophages. Frozen AAA samples fixed in optimal cutting temperature compound (OCT) at -25° were cut into 9 µm thick cryosections and subsequently mounted on SuperFrost microscope slides (Thermo Scientific). The slides were first incubated overnight at 4° using a monoclonal CD68 antibody (Rat anti-Mouse CD68, clone FA-11, Bio-Rad, 1:100) diluted in Dako REAL Antibody Diluent (Dako, Denmark) and subsequently washed with phosphate-buffered saline (PBS, pH 7.4) three times. Slides were incubated with polyclonal secondary antibody AlexaFluor 568 (Goat anti Rat IgG, Thermo Fisher Scientific, Germany, 1:200) for one hour at room temperature, followed by counterstaining and mounting with (DAPI Solution, Roti—Mount FlourCare (CARL ROTH, Germany). Co-localization of macrophages and Perl's Prussian Blue positive areas were assessed in serials section of AAAs.

**Elemental bioimaging by means of laser ablation-inductively coupled plasma-mass spectrometry for spatial localization of iron.** AAA samples were cut at -25 °C into 9 µm cryosections and immediately mounted on SuperFrost adhesion slides (Thermo Scientific). The LA-ICP-MS analysis was performed with a LSX 213 G2 + laser system (CETAC Technologies, Omaha, USA) equipped with a two volume HelEx II cell connected via Tygon tubing to an ICPMS-2030 (Shimadzu, Kyoto, Japan). Samples were ablated via line-by-line scan with a spot size of 7 µm, a scan speed of 21 µm/s and 800 mL/min He as transport gas. The analysis was performed in collision gas mode with He as collision gas and 50 ms integration time for the <sup>57</sup>Fe isotope. For the quantification of Fe, matrix-matched standards based on gelatin were used. Nine gelatin standards (10% w/w) including a blank, were spiked with different Fe concentrations ranging from 1 to 5.000 µg/g. Averaged intensities of the scanned lines of the standards showed a good linear correlation with a regression coefficient R<sup>2</sup> = 0.9999 within this concentration range. Limit of detection (LOD) and limit of quantification (LOQ), calculated with the 3σ- and 10σ-criteria, were 26 µg/g and 86 µg/g Fe. The quantification and visualization were performed with an in-house developed software (WWU Münster, Münster, Germany).

**Statistical analysis.** For the comparison of continuous variables, a Student's t test (unpaired, two-tailed) was applied. p < 0.05 was regarded to be statistically significant.

### Data availability

The datasets generated during and/or analysed during the current study are available from the corresponding author on reasonable request.

Received: 5 May 2020; Accepted: 26 June 2020

Published online: 24 July 2020

### References

1. Sakalihasan, N., Limet, R. & Defawe, O. D. Abdominal aortic aneurysm. *Lancet* **365**, 1577–1589. [https://doi.org/10.1016/s0140-6736\(05\)66459-8](https://doi.org/10.1016/s0140-6736(05)66459-8) (2005).

2. Thompson, M. M. Controlling the expansion of abdominal aortic aneurysms. *Br. J. Surg.* **90**, 897–898. <https://doi.org/10.1002/bjs.4280> (2003).
3. Shimizu, K., Mitchell, R. N. & Libby, P. Inflammation and cellular immune responses in abdominal aortic aneurysms. *Arterioscler. Thromb. Vasc. Biol.* **26**, 987–994. <https://doi.org/10.1161/01.ATV.0000214999.12921.4f> (2006).
4. Alan Daugherty, L. A. C. *Mechanisms of Abdominal Aortic Aneurysm Formation*. (2002).
5. Saraff, K., Babamusta, F., Cassis, L. A. & Daugherty, A. Aortic dissection precedes formation of aneurysms and atherosclerosis in angiotensin II-infused, apolipoprotein E-deficient mice. *Arterioscler. Thromb. Vasc. Biol.* **23**, 1621–1626. <https://doi.org/10.1161/01.ATV.0000085631.76095.64> (2003).
6. Zapotoczny, S., Szczubialka, K. & Nowakowska, M. Nanoparticles in endothelial theranostics. *Pharmacol. Rep.* **67**, 751–755. <https://doi.org/10.1016/j.pharep.2015.05.018> (2015).
7. Dulinska-Litewka, J. *et al.* Superparamagnetic iron oxide nanoparticles—current and prospective medical applications. *Materials (Basel)* **12**, <https://doi.org/10.3390/ma12040617> (2019).
8. Yang, C. Y. *et al.* Mechanism of cellular uptake and impact of ferucarbotran on macrophage physiology. *PLoS ONE* **6**, e25524. <https://doi.org/10.1371/journal.pone.0025524> (2011).
9. Neuwelt, A. *et al.* Iron-based superparamagnetic nanoparticle contrast agents for MRI of infection and inflammation. *AJR Am. J. Roentgenol.* **204**, W302–313. <https://doi.org/10.2214/AJR.14.12733> (2015).
10. Richards, J. M. *et al.* Abdominal aortic aneurysm growth predicted by uptake of ultrasmall superparamagnetic particles of iron oxide: A pilot study. *Circ. Cardiovasc. Imaging* **4**, 274–281. <https://doi.org/10.1161/CIRCIMAGING.110.959866> (2011).
11. Nchimi, A. MR imaging of iron phagocytosis in intraluminal thrombi of abdominal aortic aneurysms in humans. *Radiology* <https://doi.org/10.1148/radiol.09090657/-/DC1> (2010).
12. Carr, S., Farb, A., Pearce, W. H., Virmani, R. & Yao, J. S. Atherosclerotic plaque rupture in symptomatic carotid artery stenosis. *J Vasc Surg* **23**, 755–765 (1996) (**discussion 765–756**).
13. Reimer, P. & Balzer, T. Ferucarbotran (Resovist): A new clinically approved RES-specific contrast agent for contrast-enhanced MRI of the liver: properties, clinical development, and applications. *Eur. Radiol.* **13**, 1266–1276. <https://doi.org/10.1007/s00330-002-1721-7> (2003).
14. Buijs, R. V. *et al.* Current state of experimental imaging modalities for risk assessment of abdominal aortic aneurysm. *J. Vasc. Surg.* **57**, 851–859. <https://doi.org/10.1016/j.jvs.2012.10.097> (2013).
15. Gleich, B. & Weizenecker, J. Tomographic imaging using the nonlinear response of magnetic particles. *Nature* **435**, 1214–1217. <https://doi.org/10.1038/nature03808> (2005).
16. Brangsch, J. *et al.* Concurrent molecular magnetic resonance imaging of inflammatory activity and extracellular matrix degradation for the prediction of aneurysm rupture. *Circ. Cardiovasc. Imaging* **12**, e008707. <https://doi.org/10.1161/CIRCIMAGING.118.008707> (2019).
17. Wu, L. C. *et al.* A review of magnetic particle imaging and perspectives on neuroimaging. *AJNR Am. J. Neuroradiol.* **40**, 206–212. <https://doi.org/10.3174/ajnr.A5896> (2019).
18. Lefevre, S. *et al.* Septic arthritis: Monitoring with USPIO-enhanced macrophage MR imaging. *Radiology* **258**, 722–728. <https://doi.org/10.1148/radiol.10101272> (2011).
19. Lutz AM, W. D., Persohn E, *et al.* Imaging of macrophages in soft-tissue infection in rats: Relationship between ultrasmall superparamagnetic iron oxide dose and MR signal characteristics. (2005).
20. Eberbeck, F. W., S. Wagner, & L. Trahms. How the size distribution of magnetic nanoparticles determines their magnetic particle imaging performance. *J. Appl. Phys.* **111**, 7B318–317B3185. <https://doi.org/10.1063/1.3676053> (2011).
21. Salamon, J. *et al.* Visualization of spatial and temporal temperature distributions with magnetic particle imaging for liver tumor ablation therapy. *Sci. Rep.* **10**, <https://doi.org/10.1038/s41598-020-64280-1> (2020).
22. Daugherty, A., Manning, M. W. & Cassis, L. A. Angiotensin II promotes atherosclerotic lesions and aneurysms in apolipoprotein E-deficient mice. *J. Clin. Invest.* **105**, 1605–1612. <https://doi.org/10.1172/JCI7818> (2000).
23. Turner, G. H. *et al.* Assessment of macrophage infiltration in a murine model of abdominal aortic aneurysm. *J. Magn. Reson. Imaging* **30**, 455–460. <https://doi.org/10.1002/jmri.21843> (2009).
24. Bakenecker, A. C. *et al.* Magnetic particle imaging in vascular medicine. *Innov. Surg. Sci.* **3**, 179–192. <https://doi.org/10.1515/iss-2018-2026> (2018).
25. Weizenecker, J., Gleich, B., Rahmer, J., Dahnke, H. & Borgert, J. Three-dimensional real-time in vivo magnetic particle imaging. *Phys. Med. Biol.* **54**, L1–L10. <https://doi.org/10.1088/0031-9155/54/5/L01> (2009).
26. Haegele, J. *et al.* Magnetic particle imaging: Kinetics of the intravascular signal in vivo. *Int. J. Nanomed.* **9**, 4203–4209. <https://doi.org/10.2147/IJN.S49976> (2014).
27. Khandhar, A. P., Ferguson, R. M., Arami, H. & Krishnan, K. M. Monodisperse magnetite nanoparticle tracers for in vivo magnetic particle imaging. *Biomaterials* **34**, 3837–3845. <https://doi.org/10.1016/j.biomaterials.2013.01.087> (2013).
28. Corot, C., Robert, P., Idee, J. M. & Port, M. Recent advances in iron oxide nanocrystal technology for medical imaging. *Adv. Drug Deliv. Rev.* **58**, 1471–1504. <https://doi.org/10.1016/j.addr.2006.09.013> (2006).
29. Kratz, H. M. *et al.* MPI phantom study with a high-performing multicore tracer made by coprecipitation. *Nanomaterials (Basel)*. <https://doi.org/10.3390/nano9101466> (2019).
30. Sadat, U. *et al.* Ultrasmall superparamagnetic iron oxide-enhanced magnetic resonance imaging of abdominal aortic aneurysms—A feasibility study. *Eur. J. Vasc. Endovasc. Surg.* **41**, 167–174. <https://doi.org/10.1016/j.ejvs.2010.08.022> (2011).
31. Yao, Y. *et al.* In vivo imaging of macrophages during the early-stages of abdominal aortic aneurysm using high resolution MRI in ApoE mice. *PLoS ONE* **7**, e33523. <https://doi.org/10.1371/journal.pone.0033523> (2012).
32. Mills, C. D., Kincaid, K., Alt, J. M., Heilman, M. J. & Hill, A. M. M-1/M-2 macrophages and the Th1/Th2 paradigm. *J. Immunol.* **164**, 6166–6173. <https://doi.org/10.4049/jimmunol.164.12.6166> (2000).
33. Krzyszczyk, P., Schloss, R., Palmer, A. & Berthiaume, F. The role of macrophages in acute and chronic wound healing and interventions to promote pro-wound healing phenotypes. *Front. Physiol.* **9**, 419. <https://doi.org/10.3389/fphys.2018.00419> (2018).
34. Dale, M. A. *et al.* Elastin-derived peptides promote abdominal aortic aneurysm formation by modulating M1/M2 macrophage polarization. *J. Immunol.* **196**, 4536–4543. <https://doi.org/10.4049/jimmunol.1502454> (2016).
35. Hellenthal, F. A., Buurman, W. A., Wodzig, W. K. & Schurink, G. W. Biomarkers of abdominal aortic aneurysm progression. Part 2: Inflammation. *Nat. Rev. Cardiol.* **6**, 543–552. <https://doi.org/10.1038/nrcardio.2009.102> (2009).
36. Thompson, R. W. *et al.* Production and localization of 92-kilodalton gelatinase in abdominal aortic aneurysms. An elastolytic metalloproteinase expressed by aneurysm-infiltrating macrophages. *J. Clin. Invest.* **96**, 318–326. <https://doi.org/10.1172/JCI118037> (1995).
37. Knopp, T., Gdaniec, N. & Moddel, M. Magnetic particle imaging: From proof of principle to preclinical applications. *Phys. Med. Biol.* **62**, R124–R178. <https://doi.org/10.1088/1361-6560/aa6c99> (2017).
38. Werner F. J. C., Hofmann, M., Werner, R., Salamon, J., Säring, D., *et al.* Geometry planning and image registration in magnetic particle imaging using bimodal fiducial markers. *Med. Phys.* (2016).
39. Vogel, P. *et al.* Superspeed bolus visualization for vascular magnetic particle imaging. *IEEE Trans. Med. Imaging* <https://doi.org/10.1109/TMI.2020.2965724> (2020).
40. Franke, J. *et al.* System characterization of a highly integrated preclinical hybrid MPI-MRI scanner. *IEEE Trans. Med. Imaging* **35**, 1993–2004. <https://doi.org/10.1109/TMI.2016.2542041> (2016).

41. Kratz, H. *et al.* Novel magnetic multicore nanoparticles designed for MPI and other biomedical applications: From synthesis to first in vivo studies. *PLoS ONE* **13**, e0190214. <https://doi.org/10.1371/journal.pone.0190214> (2018).
42. 42Vogl, H., Schwarz, K., Müller, B., Lauten, B., Mack, S., Schrem, B., Neuhaus, F. Magnetic resonance imaging of focal liver lesions. Comparison of the superparamagnetic iron oxide resovist versus gadolinium-DTPA in the same patient. *Invest. Radiol.* (1996).
43. Wells, J. *et al.* Characterizing a preclinical magnetic particle imaging system with separate pickup coil. *IEEE Trans. Magn.* **53**, 1–5. <https://doi.org/10.1109/tmag.2017.2708419> (2017).
44. 44Paysen, H. *et al.* Improved sensitivity and limit-of-detection using a receive-only coil in magnetic particle imaging. *Phys. Med. Biol.* **63**, 13NT02. <https://doi.org/10.1088/1361-6560/aac87> (2018).
45. Rahmer, J., Weizenecker, J., Gleich, B. & Borgert, J. Signal encoding in magnetic particle imaging: Properties of the system function. *BMC Med. Imaging* **9**, 4. <https://doi.org/10.1186/1471-2342-9-4> (2009).
46. 46Jürgen Rahmer, J. W., Gleich, B., Borgert, J. *Analysis of a 3-D System Function Measured for Magnetic Particle Imaging.* (2012).
47. Norbert Löwa, P. R., Kosch, O., Wiekhorst, F. *Concentration Dependent MPI Tracer Performance.* (2016).
48. Weber, A., Werner, F., Weizenecker, J., Buzug, T. M. & Knopp, T. Artifact free reconstruction with the system matrix approach by overscanning the field-free-point trajectory in magnetic particle imaging. *Phys. Med. Biol.* **61**, 475–487. <https://doi.org/10.1088/0031-9155/61/2/475> (2016).
49. 49Kratz, H. *et al.* MPI phantom study with a high-performing multicore tracer made by coprecipitation. *Nanomaterials (Basel)* **9**, <https://doi.org/10.3390/nano9101466> (2019).

## Acknowledgements

This study was funded by the Deutsche Forschungsgemeinschaft (DFG, German Research Foundation)—Projektnummer 372486779—SFB 1340; MA 5943/3-1/4-1/9-1, Magnetic Particle Imaging and Research Training Group 2260 (BIOQIC),

## Author contributions

D.B.M. performed and analyzed the animal and ex vivo experiments and wrote the manuscript. M.R.M. designed and supervised the study. R.B. and U.K. designed and carried out the LA-ICP-MS experiments. A.M., J.B., H.P. and O.K. participated in ex vivo experiments and reviewed the manuscript. J.B., A.M., O.K., H.P., F.W., R.K., R.B., U.K., M.T., J.S. and B.H. reviewed and commented on the manuscript.

## Competing interests

The authors declare no competing interests.

## Additional information

**Correspondence** and requests for materials should be addressed to D.B.M.

**Reprints and permissions information** is available at [www.nature.com/reprints](http://www.nature.com/reprints).

**Publisher's note** Springer Nature remains neutral with regard to jurisdictional claims in published maps and institutional affiliations.



**Open Access** This article is licensed under a Creative Commons Attribution 4.0 International License, which permits use, sharing, adaptation, distribution and reproduction in any medium or format, as long as you give appropriate credit to the original author(s) and the source, provide a link to the Creative Commons license, and indicate if changes were made. The images or other third party material in this article are included in the article's Creative Commons license, unless indicated otherwise in a credit line to the material. If material is not included in the article's Creative Commons license and your intended use is not permitted by statutory regulation or exceeds the permitted use, you will need to obtain permission directly from the copyright holder. To view a copy of this license, visit <http://creativecommons.org/licenses/by/4.0/>.

© The Author(s) 2020

My curriculum vitae does not appear in the electronic version of my thesis due to data protection reasons.

# Complete list of publications

## Published peer-reviewed articles

Langhorst H, Juttner R, Groneberg D, **Mohtashamdolatshahi A**, Pelz L, Purfurst B, Schmidt-Ott KM, Friebe A, Rathjen FG. The IgCAM CLMP regulates expression of Connexin43 and Connexin45 in intestinal and ureteral smooth muscle contraction in mice. *Dis Model Mech.* 2018;11(2)

Kratz H, **Mohtashamdolatshahi A**, Eberbeck D, Kosch O, Hauptmann R, Wiekhorst F, Taupitz M, Hamm B, Schnorr J. MPI Phantom Study with A High-Performing Multicore Tracer Made by Coprecipitation. *Nanomaterials (Basel).* 2019;9(10):1466

**Mohtashamdolatshahi A**, Kratz H, Kosch O, Hauptmann R, Stolzenburg N, Wiekhorst F, Sack I, Hamm B, Taupitz M, Schnorr J. In vivo magnetic particle imaging: angiography of inferior vena cava and aorta in rats using newly developed multicore particles. *Sci Rep.* 2020;10(1):17247

Mangarova DB, Brangsch J, **Mohtashamdolatshahi A**, Kosch O, Paysen H, Wiekhorst F, Klopffleisch R, Buchholz R, Karst U, Taupitz M, Schnorr J, Hamm B, Makowski MR. Ex vivo magnetic particle imaging of vascular inflammation in abdominal aortic aneurysm in a murine model. *Sci Rep.* 2020;10(1):12410

Kratz H, **Mohtashamdolatshahi A**, Eberbeck D, Kosch O, Wiekhorst F, Taupitz M, Hamm B, Stolzenburg N, Schnorr J. Tailored Magnetic Multicore Nanoparticles for Use as Blood Pool MPI Tracers. *Nanomaterials (Basel).* 2021 Jun 10;11(6):1532

# Acknowledgments

Hereby, I would like to express my gratitude to everyone who supported me to accomplish this thesis.

First, I want to thank Prof. Matthias Taupitz and Dr. Jörg Schnorr for giving me the chance to be a member of the Experimental Radiology group and work on this project. I would like to acknowledge the BIOQIC graduate college and its coordinators, Prof. Ingolf Sack and Prof. Tobias Schäffter, for their support and also for creating diverse learning opportunities besides the research opportunity within the interdisciplinary BIOQIC program.

My sincere and deepest gratitude goes to Dr. Harald Kratz, not only for technical support but also moral support, and Dr. Olaf Kosch, that without their assistance and support, accomplishment of this work would have been impossible. I would like to thank Dr. Nicola Stolzenburg besides Dr. Jörg Schnorr for her assistance in in vivo studies and Susanne Metzkow for kindly assisting me with cell culture studies. I thank Dr. Frank Wiekhorst for reviewing the scientific content of the work and for allowing me access to their group facilities. I want to thank Prof. Marcus Makowski and his team, Julia Brangsch and Dilyana Mangarova for the pleasant collaboration. I am thankful to all dear lab members of Experimental Radiology and Molecular Imaging group. Special thank-you goes to Franziska Rausch, Julia Kamischke and Ledia Lilaj for sharing laughs to alleviate the load of exhausting days.

Most importantly, I would like to thank my family for the support they provided me through my entire life and especially my great friends for their moral support. No doubt without your support my success would have been impossible.

Finally, I would like to express my gratitude to everybody who taught me the tiniest bit, as knowledge is power.